A Test and Characterisation Facility for Cryogenic Low Noise Amplifiers

Presented by:

Wesley Alan Newton

Prepared for:

Dr. Willem Petrus Francois Schonken
Dept. of Electrical Engineering
University of Cape Town
and
Mr Jocias Malan
South African Radio Astronomy Observatory

A dissertation submitted to the Department of Electrical Engineering,
University of Cape Town,
in partial fulfilment of the requirements for the
degree of Master of Science in Engineering specialising in
Radar and Electronic Defence.

June, 2022

Declaration

I declare that this dissertation is my own , unaided work. I have used IEEE style of referencing. This dissertation is being submitted for the degrees of Master of Science in Engineering at the University of Cape Town . It has not been submitted before for any degree or examination in any other university.

Signature of Author …… Signed by candidate ……..

Cape Town

June 2022

Abstract

One way to describe the performance of a radio telescope is to quote its ability to receive very weak signals from astronomical sources. This receiving sensitivity is determined largely by the system noise temperature (T_{sys}). The equivalent noise temperature (T_e) of the low noise amplifier (LNA) contained within the receiver plays a major role in the T_{sys}. The LNAs are cryogenically cooled to 20 K in order to reach the required T_e performance.

Measuring the performance of this type of LNA presents a few issues that need to be addressed:

- No direct measurement of the coaxial feed cables and the amplifier under test (AUT) is possible as they are located inside a vacuum Dewar.
- The T_e of the AUT is <3.5 K over the operating band. The uncertainty of this measurement must be in the order of <1 K.

This dissertation discusses how the receiver and the LNA contained within the receiver are the major contributors to the sensitivity. Furthermore, a method for testing and determining the equivalent noise temperature of a cryogenic LNA operating at a physical temperature of 20 K is selected and presented.

This method was tested at the Klerefontein support base and the measurements allowed conclusions to be drawn that show that the uncertainty was unacceptable due to a few factors. One of the factors is the thermal gradient across the attenuator. This was investigated via a limited thermal study and a solution was proposed and implemented. Another set of measurements was performed at the Klerefontein support base and the resultant equivalent noise temperature (T_e) of the LNA was determined to within 2 K of the manufacturer supplied data.

This work presented in this dissertation forms part of the design of a test facility intended to be built at the South African Radio Astronomy Observatory (SARAO) offices.

Acknowledgements

To my supervisor Dr Francois Schonken for his encouragement and advice.

I would also like to thank my co-supervisor Sias Malan. We had many discussions where you helped me reach a conclusion or see a different solution. For reviewing my drafts and giving me valuable feedback.

I would like to thank the National Research Foundation (NRF) and the South African Radio Astronomy Observatory (SARAO) for affording me the opportunity to pursue the MSc programme:

- by fostering a company culture that encourages further study and research,
- for allocating funds for the purchasing of materials,
- for allowing the use of equipment, cryostat and other needed resources

Ben Jordaan for his much needed advice and for making time in his extremely busy schedule to assist me with testing at the Klerefontein receiver support facility.

Juan Daniel Gallego at the Yebes observatory for the valuable feedback that was used in the conclusions.

To my loving wife, Candice, for the encouragement, understanding and patience.

Edroy & Tapuwa for our weekly discussions that helped keep me focused and providing useful advice to the many issues encountered.

Glenn Taylor for helping me with the milling of the copper plates

God for gifting me with a mind that can reason and for guiding me.

Contents

List of Figures

List of Tables

Nomenclature

λ – Wavelength

A_e – Effective aperture

AUT – Amplifier under test

BW – Bandwidth in Hz

COSI - Compton Spectrometer and Imager

cm – Centimetre

DST – Department of Science and Technology

DUT – Device under test

EM - Electromagnetic

IF – Intermediate frequency

J/K – Joules per kelvin

K – Kelvin

KAT-7 – 7 dish Karoo Array Telescope

LNA – Low noise amplifier

m – Metre(s)

MeerKAT – 64 element Karoo Array Telescope

MHz – Megahertz

mK – Metres kelvin

m/s – Metres per second

NRF – National Research Foundation

OMT – Orthomode transducer

RF – Radio frequency

RFI – Radio frequency interference

SKA – Square Kilometre Array

STEM – Science, technology, engineering and mathematics

T_e – Equivalent noise temperature

T_{sys} – System noise temperature

UHF-band – Ultra high frequency band. 580 MHz to 1015 MHz in the context of MeerKAT.

XDM - Experimental development model

Conventions

In this work, the real part of a complex number $x + iy$ is denoted by the vertical bars: $|x + iy|$. Uncertainty is denoted by the capital delta symbol Δ.

Storage of scripts and measured data

The captured data and scripts can be found at https://bit.ly/3FmzRoJ.
Alternatively, the data may be requested from the author via email: wesnewton@gmail.com

"People who believe they are ignorant of nothing have neither looked for, nor stumbled upon, the boundary between what is known and unknown in the universe."

— Neil deGrasse Tyson, Astrophysics for People in a Hurry

Chapter 1

Introduction

1.1 Background

1.1.1 Radio astronomy

One of the basic human motivations is the thirst for understanding about the world that surrounds us. Since ancient times, visionary individuals have looked at the sky at night and pondered the seemingly infinite points of light.

Radio astronomy is a relatively young branch of astronomy, first pioneered in the 1930s by Jansky and in the 1940's by Reber [1][2][3][4].

In 1944 Van de Hulst proposed that the signals that Jansky and Reber had recorded were the hydrogen spectral line (21 cm line). Laboratory experiments confirmed that this phenomenon is caused by the change in the energy state of neutral hydrogen atoms and thus radio astronomy was legitimised as a new way of studying the universe [5][6].

Since then radio astronomy has blossomed into a vitally important branch of astrophysics.

1.1.2 Ground-based radio astronomy

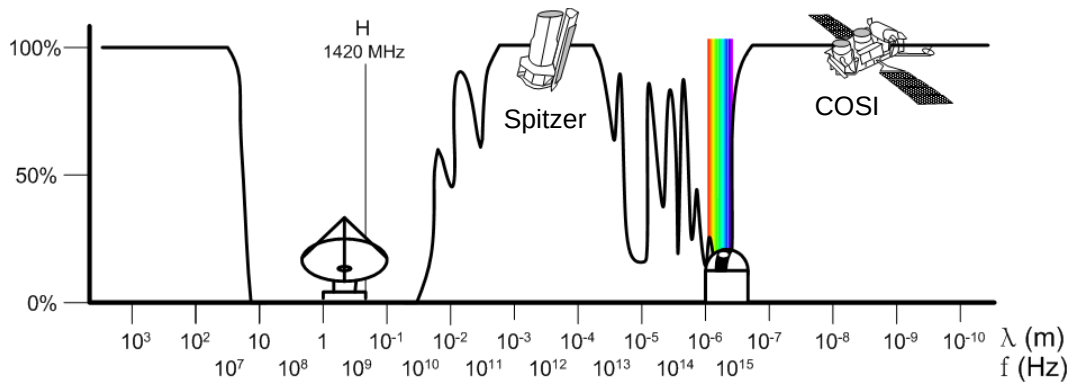

Figure 1.1. The electromagnetic (EM) spectrum showing atmospheric absorption [7].

Figure 1.1 shows the EM spectrum with a simplified representation of the Earths' atmospheric absorption line overlayed on the figure. This absorption line varies between 0% to no propagation at 100 %.

Shown in Figure 1.1 are icons that represent the space-based telescopes:

- Spitzer Space Telescope
- Compton Spectrometer and Imager (COSI)

Both operate in part of the EM spectrum that is mostly blocked by the Earths' atmosphere.

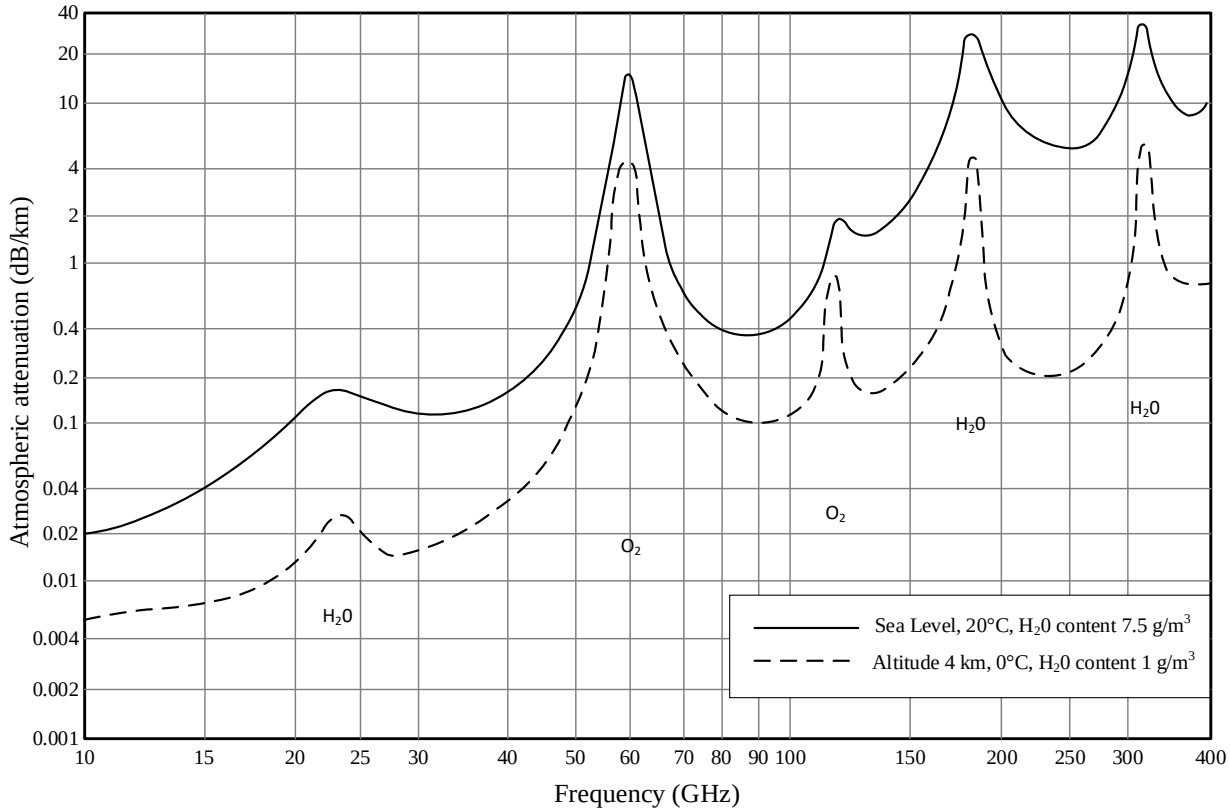

Figure 1.2. Measured average atmospheric absorption of EM waves from 10 GHz to 400 GHz [8].

The prediction of atmospheric absorption of EM waves is a complex issue. As illustrated in Figure 1.2, there is a variation of atmospheric attenuation with frequency due to electromagnetic (EM) wave absorption properties of atmospheric water vapour and oxygen. Radio telescopes are located at high altitudes to encounter as little atmospheric interference as possible.

Ground-based *optical* astronomy occurs within the visible light section of the spectrum and is subject to partial atmospheric distortion, whereas ground-based *radio* astronomy is subject to very little atmospheric distortion. In ground-based radio astronomy the atmospheric distortion tends to increase with increasing signal frequency. Additionally, a wider EM spectrum is available to radio astronomy and the EM waves received in radio astronomy are able to provide information about the electric and magnetic fields that they propagated through. Lastly, radio astronomy observations can occur day or night.

Table 1.1. Examples of existing ground-based radio telescopes.

Name	Altitude above sea level (m)	Frequency Range (GHz)
Atacama Large Millimeter Array (ALMA) [9]	5058	35 to 950
Green Bank Telescope (GBT) [10]	807	0.1 to 116
MeerKAT [11] [12]	1309	0.58 to 3.5
Very Large Array (VLA) [13]	2124	0.74 to 50

Challenges with radio astronomy:

- Spatial resolution decreases with decreasing wavelength in the case of a single-dish antenna. The spatial resolution is improved by using large dishes or antenna arrays.
- Radio frequency interference (RFI) is a major challenge.
- Reception and amplification of extremely low-power signals. See chapter 2.2.1 for an expanded explanation.

1.1.3 The MeerKAT project

The MeerKAT radio telescope is a 64-element radio telescope array built in the Northern Cape province of South Africa. Funded by the South African National Research Foundation (NRF) and Department of Science and Technology (DST), it is the precursor instrument to the SKA mid-frequency band. At the time of its launch in 2018 it was the most sensitive centimetre (cm) wavelength telescope in the southern hemisphere.

It was preceded by the single eXperimental Development Model (XDM) dish and then later by a seven dish Karoo Array Telescope (KAT-7) interferometer [14][15][16].

The MeerKAT radio telescope is a 64 element antenna array consisting of Gregorian offset dishes. Each dish in the array is 13.965 m in diameter. The frequency range of each element is 580 MHz to 3.5 GHz. This is divided into UHF, L-band and S-band receivers[1] [16].

Figure 1.3. Photograph of the MeerKAT radio telescope [17].

1.2 Problem statement

The sensitivity of a radio telescope antenna is discussed in detail in section 2.2. The main goal of this discussion is to illustrate the critical role that the low noise amplifier (LNA) performs in the sensitivity of the MeerKAT radio-telescope array element.

There is a need to accurately measure the equivalent noise temperature (T_e) of the LNA used in the MeerKAT receiver for the purposes of optimisation and fault-finding. The equivalent noise temperature is a figure of merit that describes the noise contribution of the LNA during signal amplification[2]. In order to achieve the ultra-low T_e performance goal, the LNA operates at a physical temperature of approximately 20 K inside a vacuum cryostat. It is therefore important that the LNA be tested under the same vacuum and temperature conditions to ensure

[1] The compromise was made to split up the frequency range into narrower band receivers to achieve optimal sensitivity and EM performance [16].

[2] The equivalent noise temperature is discussed in detail in section 2.1.

proper functionality prior to final receiver installation. Additionally a range of LNAs may be evaluated in this operational environment.

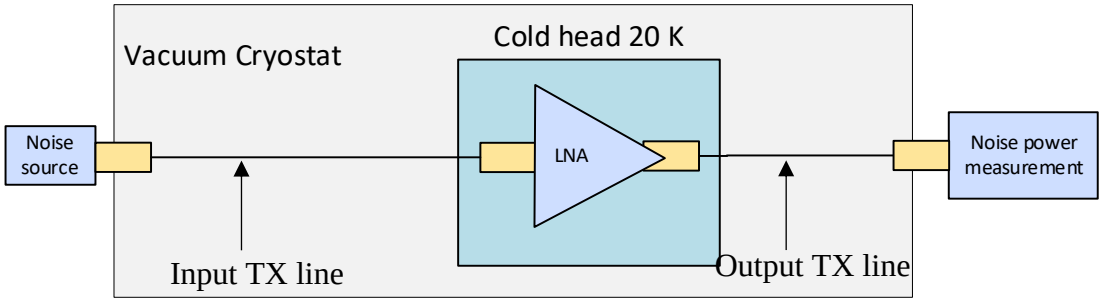

Figure 1.4. The measurement of a cryogenic LNA using the classic Y-factor method.

The challenges presented by this type of measurement include:

- No physical access to the LNA or internal cables during operation.
- Characterisation of the input transmission line (TX line) is complex due to the large temperature gradient across it. The noise contribution and loss through the input TX line adds unacceptable uncertainty to the measurement signal present at the LNA.
- The expected LNA T_e is in the order of 1 to 2 K. This measurement method requires very low uncertainty to be meaningful.

1.3 Objectives and scope

The main objectives of this thesis are to review the available T_e measurement methods; select the most suitable method based on the review; design and build a T_e measurement system based on the selected method; perform measurements on a cryogenic LNA; and then interpret and present the results.

1.4 Limitations

The mechanical design of the vacuum cryostat is outside the scope of this thesis. The constraint was set to use an existing receiver to carry out the test to avoid over-investment of resources.

1.5 Thesis structure

This thesis is structured as follows:

- **Chapter 2** explains relevant concepts in more detail and the role of the LNA in the context of the MeerKAT radio telescope.
- **Chapter 3** provides a literature review of cryogenic LNA measurement methods.
- **Chapter 4** describes the proposed measurement solution and physical implementation including the major components selected and hardware used.
- **Chapter 5** gives an overview of the measurements carried out and the comments and issues encountered during the test campaigns, including a limited thermal study. The measurement results are presented.
- **Chapter 6** presents a summary of the work, compares the results with the supplier data. Conclusions are discussed based on the results and suggestions are put forward for future work.

Chapter 2

Background information

2.1 Thermal noise in electrical circuits

Since the adoption of the telephone in 1878, interference began to be recognised as a limitation to the reception of very weak signals. This “hiss” that was present on the receiving speaker was attributed to manufacturing defects within the tube or insufficient shielding of the conductors [18].

However the paper describing the fundamental limit presented by thermal noise was published in 1928 by Johnson and Nyquist. The design and manufacturing of tube amplifiers had improved to a level that Johnson had a “good” amplifier with enough gain to study the phenomena of thermal noise [19][20].

Thermal noise exists as a measurable random variation of potential difference between the terminals of any conductor.

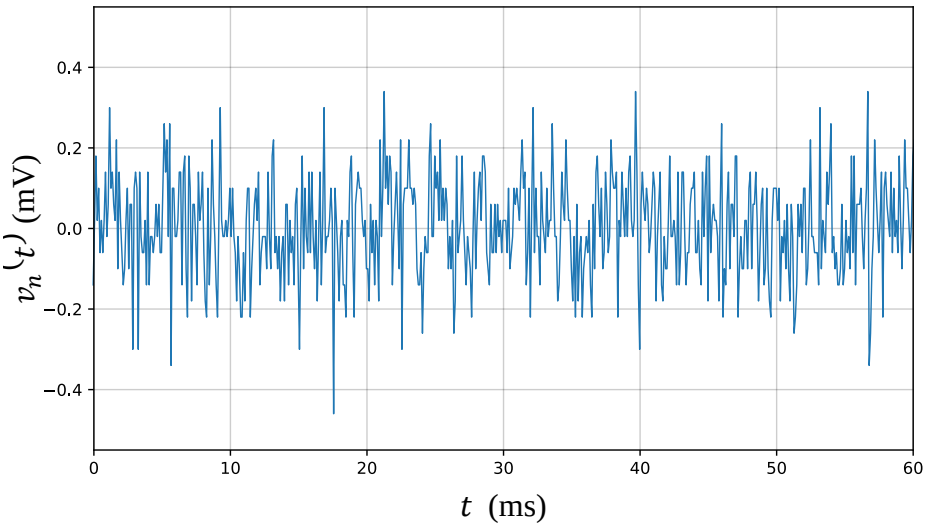

Figure 2.1. Measured randomly varying voltage across a conductor (generated by author).

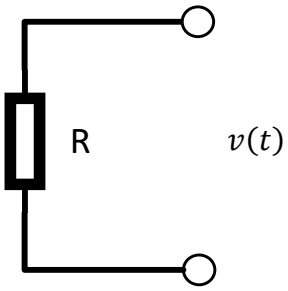

Figure 2.2. Measuring the random voltage $v_n(t)$ across a resistor.

Figure 2.1 presents the measured instantaneous noise voltage as a function of time denoted as $v_n(t)$ measured across a resistor shown in Figure 2.2 . The root mean square (RMS) value of the noise voltage is denoted as V_n and it can be described using a form of Planck's black-body radiation law equation [21]:

$$V_n = \sqrt{\frac{4hf\ BWR}{e^{hf/kT} - 1}} \tag{2.1}$$

Where:

- V_n is the RMS value of noise voltage in V.
- $h = 6.62607015\ \times\ 10^{-34}$ is Planck's constant in J/Hz.
- f is the center frequency of the bandwidth in Hz.
- BW is the instantaneous bandwidth of the system in Hz.
- R is the resistance across the terminals in Ω.
- $k\ =\ 1.380\ x\ 10^{-23}$ is Boltzmann's constant in J/K.
- T is the physical temperature of the resistor in K.

The Rayleigh-Jeans approximation reduces the complexity of equation (2.1) by making the following assumption [21]:

$$e^{hf/kT} - 1 \approx \frac{hf}{kT} \tag{2.2}$$

This approximation may not be valid for frequencies above 100 GHz or physical temperatures below 100 K, but it does allow simplification of (2.1) to yield the equation [21]:

$$V_n = \sqrt{4kTBWR} \tag{2.3}$$

Where:

- V_n is the RMS value of noise voltage in V.
- BW is the instantaneous bandwidth of the system in Hz.
- R is the resistance across the terminals in Ω.
- $k = 1.380\ x\ 10^{-23}$ is Boltzmann's constant in J/K.
- T is the physical temperature of the resistor in K.

Shown in Figure 2.3 the noisy resistor is represented by an equivalent circuit consisting of a noiseless resistor and an RMS noise voltage generator in series. The circuit is terminated in the resistor or value R to give maximum power transfer.

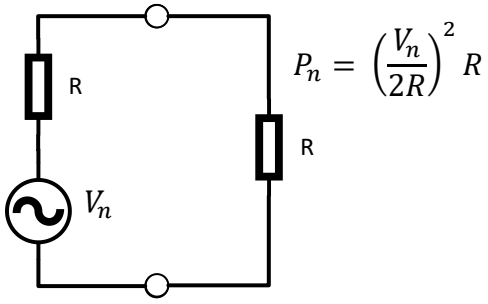

Figure 2.3. Equivalent circuit with the voltage generator and noiseless resistors R [21].

The available noise power (P_n) delivered to the load resistor is calculated by assuming that equation (2.2) is valid and substituting equation (2.3) to result in the equation [21][22]:

$$P_n = \left(\frac{V_n}{2R}\right)^2 \times R = \frac{{V_n}^2}{4R} = kTBW \tag{2.4}$$

Where:

- P_n is the maximum available noise power in W.
- BW is the instantaneous bandwidth of the system in Hz.
- $k = 1.380\ x\ 10^{-23}$ is Boltzmann's constant in J/K.
- T is the physical temperature of the resistor in K.

2.1.1 Equivalent noise temperature

Noise power that remains relatively constant over the system bandwidth is called white noise. When a noise source emits white noise, equivalent noise temperature (T_e) can be used to describe the source. In essence the noise source is replaced with an equivalent thermal source at a temperature of T_e that results in the same P_n and equation (2.4) is still satisfied. Equation (2.4) is rearranged to make T_e the subject [21]:

$$T_e = \frac{P_n}{kBW} \tag{2.5}$$

Where:

- T_e is the noise temperature in K.
- P_n is the noise power in W.
- BW is the instantaneous bandwidth of the system in Hz.
- $k = 1.380\ x\ 10^{-23}$ is Boltzmann's constant in J/K.

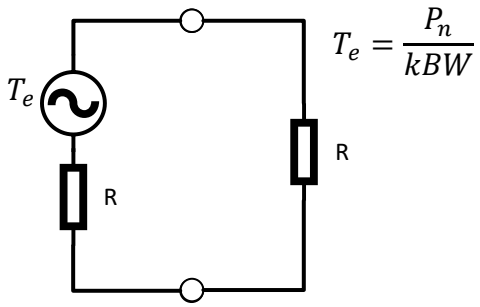

Figure 2.4. Equivalent circuit with the thermal noise generator and noiseless resistors R [21].

The T_e can be referenced at the input port or output port of a device. For amplifiers, T_e is normally referenced at the input port and for passive devices T_e is normally referenced at the output port.

2.1.2 Equivalent noise temperature of an LNA

Figure 2.5 shows a 2-port network with available gain (G_a). The input of the LNA is terminated with a resistor R and a generator to represent its noise. The noise available at the output of the LNA is equal to [21]:

$$G_a \cdot (T_{e\,LNA} + T_{e1})$$

$T_{e\,LNA}$ is modelled as an additional generator at the input of the amplifier that is summed with the wanted signal.

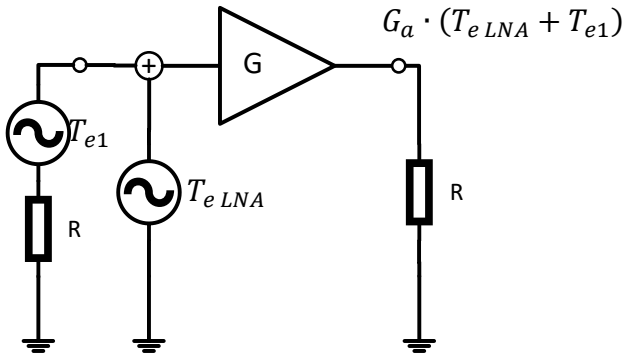

Figure 2.5. Equivalent circuit with $T_{e\,LNA}$ modelled as a generator [21].

The $T_{e\,LNA}$ denotes the noise contributed by the amplifier itself as the signal is amplified. The resultant signal at the output of the amplifier contains both the wanted T_{e1} and the unwanted $T_{e\,LNA}$. Although amplification has taken place, the signal-to-noise ratio at the output of the LNA is worse than at the input [21].

2.1.3 Equivalent noise temperature of a passive component

Passive lossy components, such as transmission lines and attenuators, will have a T_e that is directly proportional to the physical temperature and the available gain (G_a) where $G_a < 1$ of the component and is determined by the equation [21]:

$$T_e = \left(\frac{1}{G_a} - 1\right) T = \frac{(L_i - 1)(L_i + |\Gamma_s|^2)}{L_i(1 - |\Gamma_s|^2)} T \qquad (2.6)$$

Where:

- T_e is the equivalent noise temperature of the passive mismatched component in K.
- G_a is the available power gain of the passive mismatched component in W/W.
- T is the physical temperature of the passive component in K.
- L_i is the insertion loss of the passive matched component in W/W.
- Γ_s is the reflection coefficient looking towards the source.

There is a special case of equation (2.6) when there is no mismatch, $\Gamma_s = 0$, and the equation becomes [21]:

$$T_e = (L_i - 1)T = \left(\frac{1}{G_i} - 1\right)T \tag{2.7}$$

Where:

- T_e is the equivalent noise temperature of the passive matched component in K.
- T is the physical temperature of the passive matched component in K.
- L_i is the insertion loss of the passive matched component in W/W.
- G_i is the insertion power gain of the passive mismatched component in W/W.

Randa *et al*. (2005) presented the use of the full Planck form for the T_e of a passive termination. This prevents errors associated with the Rayleigh-Jeans approximation equation (2.2) that can occur at very low temperatures and very high frequencies [23]:

$$T_e = \frac{1}{k}\left(\frac{hf}{e^{hf/kT} - 1}\right) \tag{2.8}$$

Where:

- T_e is the noise temperature available at the output port of a passive termination in K.
- $k = 1.380\ x\ 10^{-23}$ is Boltzmann's constant in J/K.
- $h = 6.62607015 \times 10^{-34}$ is Planck's constant in J/Hz.
- f is the center frequency of the bandwidth in Hz.
- T is the physical temperature of the passive termination in K.

2.1.4 Cascaded power gain

Insertion power gain[3] (G_i) can be used to refer to the power gain of an LNA. G_i may be measured using a scalar network analyser or power meter and signal generator. G_i is defined as the

[3] Also known as scalar linear gain.

difference in power measured between the LNA and bypassing the LNA with a short low-loss coaxial line. G_i is described using the equation [21][24]:

$$G_i = |S_{21}|^2 \tag{2.9}$$

The problem with G_i is that it assumes the source reflection coefficient (Γ_S) and the load reflection coefficient (Γ_L). The power gain may vary substantially with different values of Γ_S presented to the input port and different values of Γ_L presented at the output port.

A definition of power gain that makes provision for the Γ_S is available power gain (G_a). This definition of gain incorporates the scattering matrix measurement and port mismatches for source and output port. Multi stage networks defined using G_a can be directly cascaded as the Γ_{out} of the proceeding stage forms the Γ_s for the following stage.

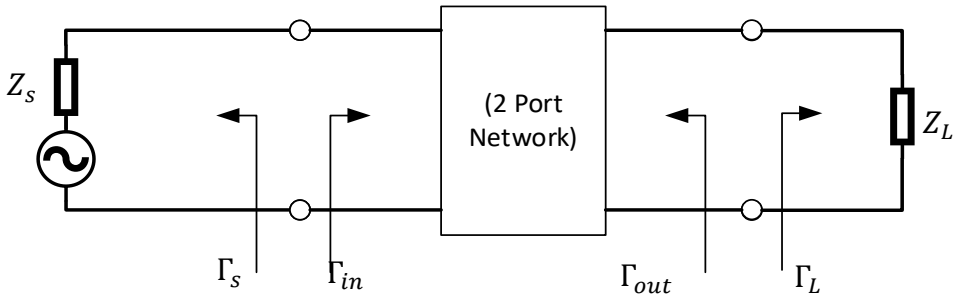

Figure 2.6. A two-port network diagram [21].

G_a is defined in terms of the ratio of the power available from the network (P_{avn}) to the power available from the source (P_{avs}) and can be determined using the equation [21][24] [25][26][27]:

$$G_a = \frac{P_{avn}}{P_{avs}} = \frac{|S_{21}|^2(1 - |\Gamma_s|^2)}{|1 - S_{11}\Gamma_s|^2(1 - |\Gamma_{out}|^2)} \tag{2.10}$$

Where:

- G_a is the available power gain of a two-port network in W/W.
- P_{avn} is the power available from the two-port network in W.
- P_{avs} is the power available from the source in W.
- Γ_s is the reflection coefficient looking towards the source.
- Γ_{out} is the reflection coefficient looking back into the output of the two-port network.

- S_{21} is the scattering parameter complex ratio between the voltage wave measured at port 2 when an incident voltage wave is applied to port 1.
- S_{11} is the scattering parameter complex ratio between the voltage wave measured at port 1 when an incident voltage wave is applied to port 1.

The output reflection coefficient is required to calculate the G_a and this can be determine using the equation [21][24]:

$$\Gamma_{out} = S_{22} + \frac{S_{12}S_{21}\Gamma_s}{1 - S_{11}\Gamma_s} \tag{2.11}$$

Where:

- Γ_{out} is the reflection coefficient looking back towards the output of the two-port network.
- Γ_s is the reflection coefficient looking towards the source.
- S_{11} is the scattering parameter complex ratio between the voltage wave measured at port 1 when an incident voltage wave is applied to port 1.
- S_{22} is the scattering parameter complex ratio between the voltage wave measured at port 2 when an incident voltage wave is applied to port 2.
- S_{12} is the scattering parameter complex ratio between the voltage wave measured at port 1 when an incident voltage wave is applied to port 2.
- S_{21} is the scattering parameter complex ratio between the voltage wave measured at port 2 when an incident voltage wave is applied to port 1.

2.1.5 Cascaded noise temperature

When there is a signal chain or cascade of components as presented in Figure 2.7, each component will have an associated T_e and G_a. It may seem counterintuitive when first encountered, but the T_e of each stage does not simply multiply as in the case of G_a. Instead, equation (2.12) describes how to calculate the equivalent cascaded noise temperature (T_{cas}) shown in Figure 2.7 [21][28].

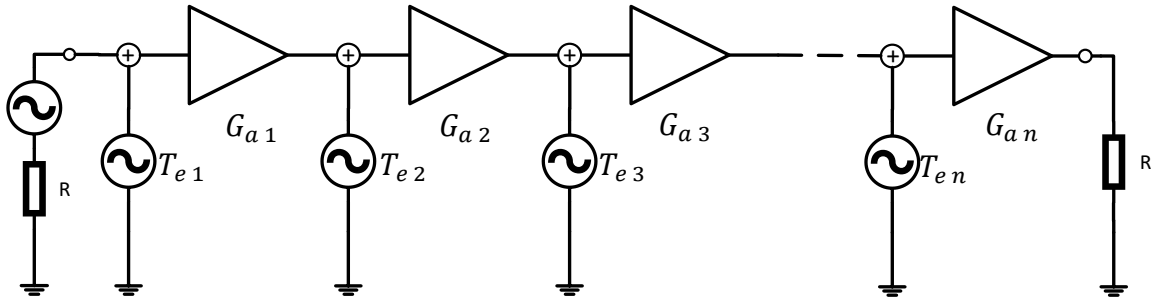

Figure 2.7. Cascaded amplifiers with gain and equivalent noise temperature. Each signal chain element has its T_e represented by a signal source [21].

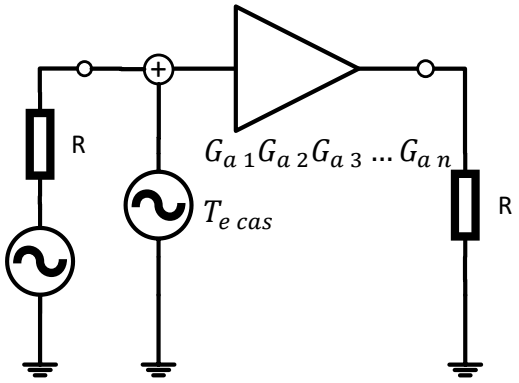

Figure 2.8. The equivalent network for the cascade [21].

The T_e of the first stage has the highest contribution to the $T_{e\,cas}$. The T_e of each successive stage is divided by the cumulative gain of the preceding stages. This is shown below in Friis's cascaded noise equation and it is important that the first stage of amplification has a high G_a and extremely low T_e [21][28]:

$$T_{e\,cas} = T_{e\,1} + \frac{T_{e\,2}}{G_{a\,1}} + \frac{T_{e\,3}}{G_{a\,1}G_{a\,2}} + \cdots + \frac{T_{e\,n}}{G_{a\,1}G_{a\,2}\ldots G_{a\,n-1}} \quad (2.12)$$

Where:

- $T_{e\,cas}$ is the T_e of the cascaded signal chain in K.
- $T_{e\,1}$ is the T_e of the first element in the signal chain in K.
- $T_{e\,2}$ is the T_e of the second element in the signal chain in K.
- $T_{e\,3}$ is the T_e of the third element in K.
- $T_{e\,n}$ is the T_e of the nth element in K.
- $G_{a\,1}$ is the G_a of the first element in W/W.
- $G_{a\,2}$ is the G_a of the second element in W/W.
- $G_{a\,n-1}$ is the G_a of the n-1 element W/W.

2.2 The sensitivity of a radio telescope

2.2.1 Received signal power

There are various types of sources of radio signals, classified as thermal or non-thermal. In this chapter only the thermal black-body radiation is considered. To illustrate the relevance of sensitivity it is important to examine some fundamental black-body radiation laws [6].

Wien's displacement law states that the spectral energy density of the black-body radiator peaks at a wavelength λ_{peak}. The peak wavelength is inversely proportional to physical temperature of the black-body radiator as described by the equation [6][29]:

$$\lambda_{peak} = \frac{b}{T} \quad (2.13)$$

Where:

- λ_{peak} is the wavelength of peak spectral energy density in m.
- $b = 2.897771955 \times 10^{-3}$ is the Wien's displacement constant in m·K.
- T is the physical temperature in K.

The Rayleigh-Jeans law states that the spectral energy density increases as the square of the signal frequency. This is only valid at frequencies below 100 GHz [6].

$$B_f(T) = \frac{2f^2kT}{c^2} \tag{2.14}$$

Where:

- $B_f(T)$is the spectral energy density in $Wm^{-2}Hz^{-1}rad^{-2}$.
- $c = 2.99792458 \times 10^8$ is the speed of light in m/s.
- $k = 1.380\ x\ 10^{-23}$ is Boltzmann's constant in J/K.
- T is the physical temperature in K.
- f is the signal frequency in Hz.

While Wien's displacement law and the Rayleigh-Jeans law are intuitive, they are incomplete. A more complete description of the spectral energy density of a black-body radiator is given by Planck's law. Planck asserted that every physical body at a temperature above zero K emits electromagnetic radiation. The spectral energy density at frequency f of a body at temperature T can be determined by the equation [6]:

$$B(f,T) = \frac{2hf^3}{c^2} \cdot \frac{1}{e^{hf/kT} - 1} \tag{2.15}$$

Where:

- $B(f,T)$ is the spectral energy density in $Wm^{-2}Hz^{-1}rad^{-2}s$.
- $h = 6.62607015 \times 10^{-34}$ is Planck's constant in J/Hz.
- $c = 2.99792458 \times 10^8$ is the speed of light in a vacuum in m/s.
- $k = 1.380 \times 10^{-23}$ is Boltzmann's constant in J/K.
- T is the physical temperature in K.
- f is the frequency in Hz.

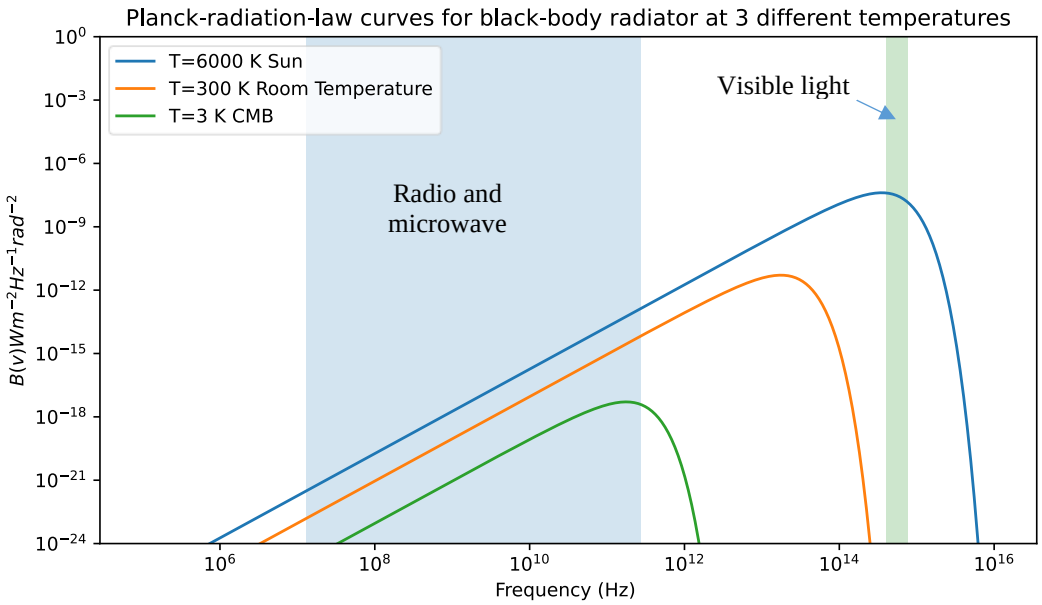

Figure 2.9. The Planck radiation law curves for a black-body radiator[4] [6].

Shown in Figure 2.9 is the Planck radiation law curves for a black-body radiator. The international telecommunications union (ITU) allocated radio astronomy frequency allocations all fall within the blue shaded area of 13 MHz to 275 GHz. The frequency range of visible light is shaded in green[5]. This shows one of the trade-offs of radio astronomy versus optical astronomy: the spectral energy density $B(v)$ of a black-body radiator is directly dependant on the physical temperature of the radiator. $B(v)$ decreases dramatically with decreasing signal frequency [30].

The consequence of this is that radio astronomy instruments receive extremely low power signals compared to optical astronomy. Therefore, the ability to receive these extremely low power signals is one of the critical design considerations of a radio telescope.

2.2.2 The radio telescope antenna array element

Although the MeerKAT radio telescope is an antenna array, only one array element is considered in this analysis.

[4] The source code for this script can be found at Appendix A - Python script for generating Planck blackbody radiation curves

[5] Visible light frequency range is 400 THz to 769 THz

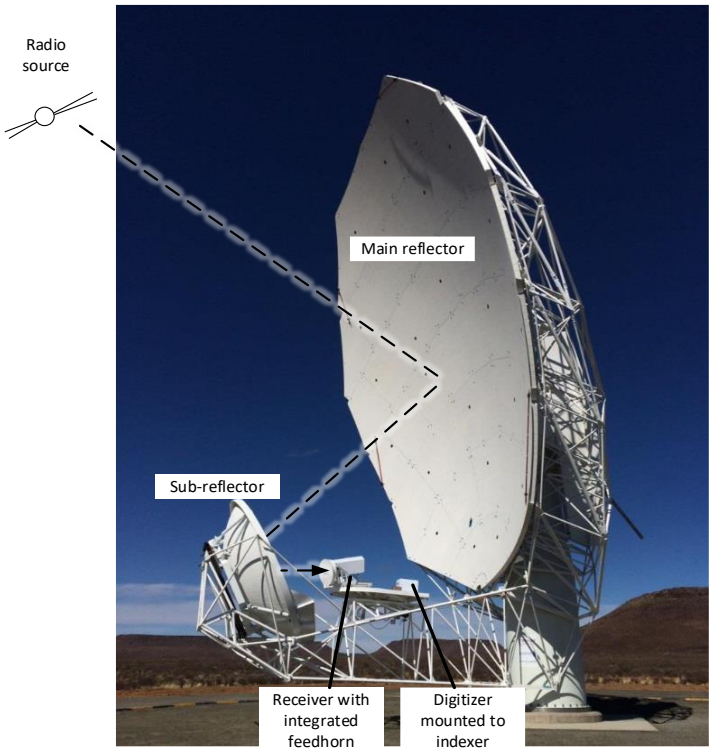

Figure 2.10. Picture of a single MeerKAT radio telescope antenna array element with the path of the EM waves depicted using the dashed line [31].

In Figure 2.10 an image of a single MeerKAT antenna element is shown in order to illustrate where each of the items in the block diagram is physically located. Figure 2.11 below shows a functional block diagram of the array element. In both diagrams the signal flow shows electromagnetic (EM) waves from the distant radio source collected by the dish optics and converted to two electrically conducted signals by the receiver. The electrically conducted signals are converted from an analog radio frequency signal to data packets by the digitizer and then sent to the correlator.

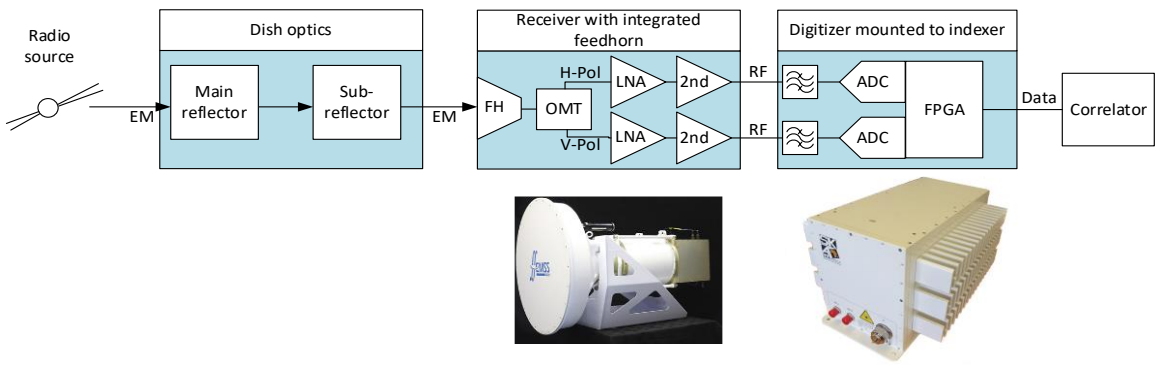

Figure 2.11. The block diagram of a radio telescope antenna array element. The signal flow and conversion of the EM waves to conducted RF signals to data packets is shown [32].

2.2.3 The radiometer equation

Radiometry is a technique that develops information about a source solely from the radio and microwave frequency radiation that originates from the source. A radiometer is a sensitive receiver that is designed to measure the noise power of the radio and microwave radiation. A radio telescope is a radiometer used for radio astronomy. The measure of the ability of a radiometer to receive extremely low power signals is defined as the sensitivity given by the equation [6][11][21][33]:

$$\Delta T_{min} = \frac{T_{sys}}{\sqrt{BW \cdot \tau}} \tag{2.16}$$

Where:

- ΔT_{min} is the minimum detectable signal of the radiometer in K.
- T_{sys} is the system noise temperature in K. Refer to section 2.2.6 for a more detailed discussion.
- τ is the integration time in s.
- BW is the instantaneous bandwidth of the radiometer detector in Hz.

The ideal radiometer equation shows that ΔT_{min} can be decreased by:

- Increasing BW.
- Increasing τ.
- Lowering T_{sys}.

Furthermore, it can be seen that lowering T_{sys} is the most effective way of improving ΔT_{min}, since the other two parameters must be increased by the same factor squared to have the same effect.

The T_{sys} specifications for the MeerKAT UHF-band telescope configuration is 20 K to 27 K [16].

2.2.4 Minimum detectable flux density

The ultimate sensitivity of a radio telescope element is given by the minimum detectible flux density (S_{min}). The equation for S_{min} contains the elements from ΔT_{min} with the addition of effective aperture (A_e), the receiver constant K_s and Boltzmann's constant. Essentially, the S_{min} equation takes into account the characteristics of the dish optics and effective aperture of the antenna [6]:

$$S_{min} = \frac{2kK_sT_{sys}}{A_e\sqrt{BW \cdot \tau}} \tag{2.17}$$

Where:

- S_{min} is the minimum detectable flux density for a radio telescope in W/m^2.
- $k = 1.380\ x\ 10^{-23}$ is Boltzmann's constant in J/K.
- K_s is the receiver constant. This is 1 for a total power radiometer.
- T_{sys} is the system noise temperature in K.
- A_e is the effective aperture in m^2. Refer to section 2.2.5.
- BW is the bandwidth in Hz.
- τ is the integration time in s.

2.2.5 Effective aperture

The area that collects the EM energy incident on the antenna is called the antenna effective aperture (A_e). An electrically large aperture will increase the antenna gain. The gain of an antenna (G_{ant}) is defined as the ratio of the maximum radiation intensity in the main beam to the average radiation intensity in all space multiplied by the antenna radiation efficiency. The effective aperture of an antenna can be expressed by the equation [21]:

$$A_e = \frac{G_{ant}\lambda^2}{4\,\pi} \tag{2.18}$$

Where:

- A_e is the effective aperture area of the antenna in m^2.
- G_{ant} is the antenna gain in W/W.
- λ is the wavelength in m.

And the equation:

$$A_e = \eta_{ap} A_g \tag{2.19}$$

Where:

- A_e is the effective aperture in m^2.
- η_{ap} is the aperture efficiency.
- A_g is the geometric aperture area based on the radiation pattern and wavelength in m^2.

The minimum detectable flux density can be increased by increasing A_e, which is related to the physical size of the dish optics and feedhorn. Factors that reduce the A_e are surface errors due to limited machining tolerance of the reflector surface, blockage due to support structure in the path of the received EM waves, losses due to finite resistance in the reflector materials, spill-over of the feed pattern and the losses due to the aperture illumination taper [16][21][34][35].

2.2.6 System temperature

The system temperature (T_{sys}) is the equivalent noise temperature of the single array antenna element in K. It consists of the sky background temperature (T_{sky}), spill-over to ground (T_{spill}), the temperature contribution from the atmosphere (T_{atm}), the scattering from feed support structure ($T_{scattering}$) and the equivalent noise temperature of the receiver (T_{RX}). The elements that contribute to T_{sys} are shown in the system diagram Figure 2.12 and can be represented by the equation [6][21][35]:

$$T_{sys} = T_{sky} + T_{spill} + T_{atm} + T_{scattering} + T_{RX} \tag{2.20}$$

Where:

- T_{sky} is the sky noise temperature. Assumed to be "cold sky" for most cases = $2.725 + 1.6(frequency\ in\ GHz)^{-2.75}$ K.
- T_{spill} is the antenna spill-over noise temperature contribution in K. This can be minimised through reflector and antenna design.
- T_{atm} is the noise temperature contribution of the atmosphere in K.
- T_{RX} is the equivalent noise temperature of the receiver in K.

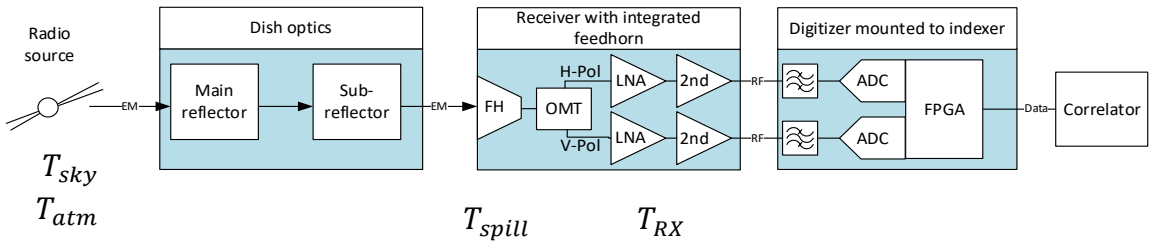

Figure 2.12. The block diagram of a radio telescope antenna element. The T_{sys} components are shown [32].

The offset Gregorian type reflector design for the MeerKAT antenna avoids any scattering from the structure, thus $T_{scattering}$ is not a factor. The feedhorn and orthomode transducer (OMT) are integrated into the receiver assembly, thus resistive losses in the feedhorn and OMT (T_{loss}) are included in T_{RX}. A single MeerKAT antenna array element in UHF-band configuration has a T_{sys} of 20 to 27 K [16] [34][35].

2.2.7 The receiver and low noise amplifier

The UHF-band receiver and L-band receiver were designed and built by EMSS Antennas. The receivers are mounted to the feed indexer. The UHF-band receiver is selected by rotating the indexer so that the focal point of the sub-reflector aligns with the UHF-band receiver feedhorn [16].

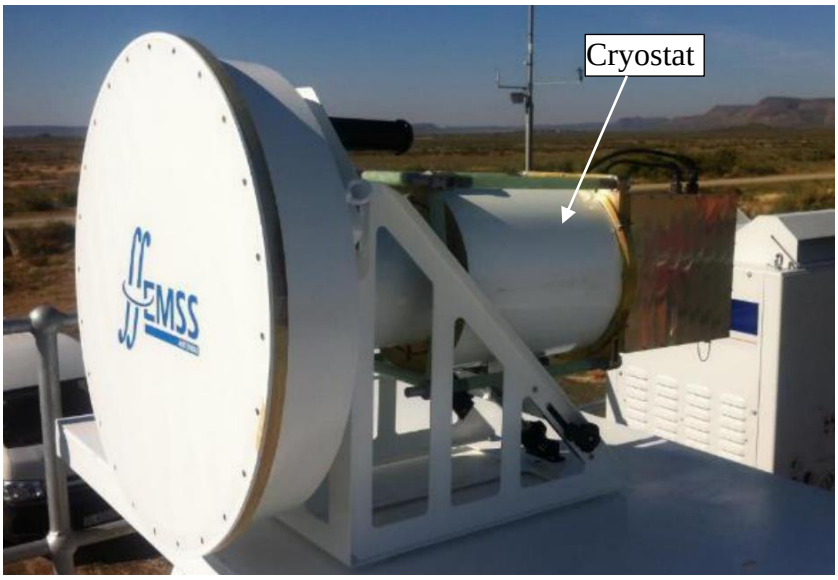

Figure 2.13. The receiver built by EMSS Antennas with feedhorn attached [31].

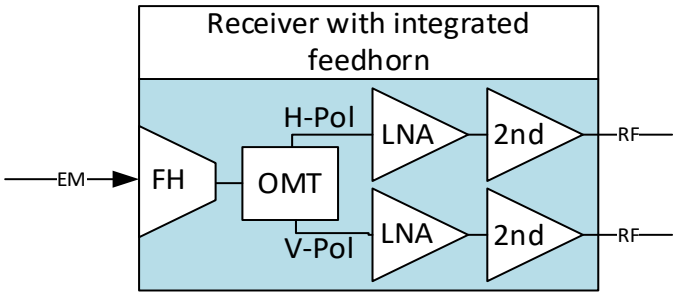

Figure 2.14. A block diagram of the receiver.

The receiver with the feedhorn attached is shown in Figure 2.13. Figure 2.14 shows a block diagram of the receiver. The EM waves collected by the main dish optics enter the feedhorn (FH) and two orthogonally polarised EM waves are converted into electrically conducted signals by the orthomode transducer (OMT). The output signals from the OMT, denoted as horizontally polarised (H-pol) and vertically polarised (V-pol) are each conducted via a coaxial cable to the low noise amplifiers (LNA). The cryo-cooler keeps the OMT at a physical temperature of approximately 100 K to reduce the noise temperature contribution before the LNA. The LNAs are cooled by the cryocooler to approximately 20 K [16].

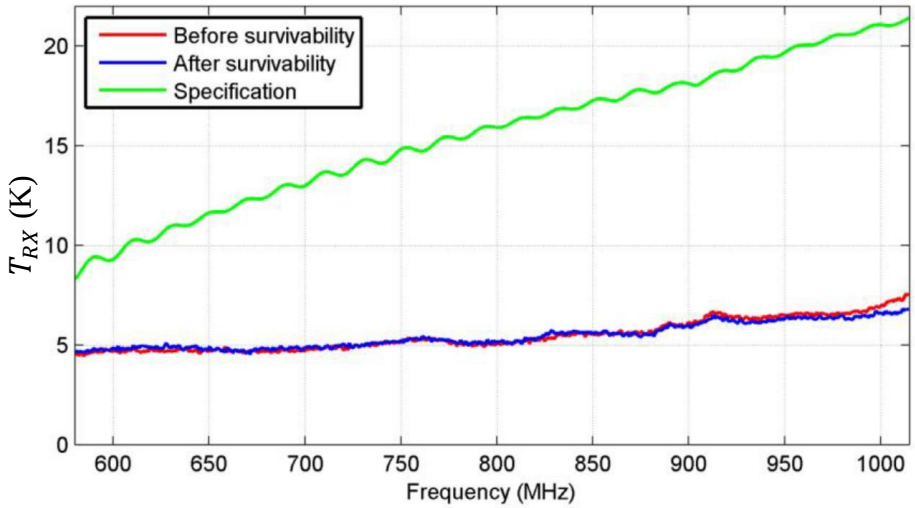

Figure 2.15. UHF-band receiver noise temperature T_{RX}. Survivability refers to the survivability test that injects the highest input power allowed. There should be no degradation in performance after the survivability test. [36].

The LNA is the first stage of amplification of the received signal within the receiver. As explained in section 2.1.5, the first stage of amplification has the greatest effect on the equivalent noise temperature of the entire receiver.

For a single MeerKAT antenna element in the UHF-band configuration, the T_{RX} is 5 K to 7 K as shown in Figure 2.15. The frequency range for the UHF-band receiver is 580 MHz to 1015 MHz [16][34][35].

2.2.8 The UHF-band LNA

The UHF-band cryogenic LNA was developed for the UHF-band receiver by Herzberg Astronomy and Astrophysics (HAA), a part of the National Research Council Canada (NRC). The first stage uses an Indium Phosphate (InP) high electron mobility transistor (HEMT) as it gives the best low noise performance. The second and third stage use Gallium Arsenide (GaAs) HEMTs as these give high gain and good amplitude stability. The LNA has the following specifications across the frequency band of operation [37]:

- A T_e of 0.6 K average.
- A gain of greater than 45 dB.
- Input and output return losses of less than 12 dB.
- Operation over the frequency band of 580 to 1070 MHz.

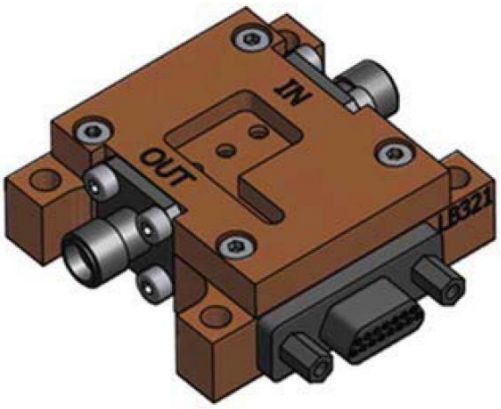

Figure 2.16. The UHF-band LNA [38].

The effect of cryogenic cooling on an LNA is illustrated by McCulloch *et al.*, 2017 and represented in Figure 2.17. Even though their measurements were not performed on the UHF-band LNA used in MeerKAT, the results presented are still of importance as they show that in general the T_e of cryogenic LNAs have a direct linear relationship with the physical temperature of the electron channel within the LNA transistors. The self-heating effect of the electron channel has an increasingly prominent effect on the reduction of the T_e of the LNA below about 25 K physical case temperature. These characteristics vary depending on the transistors used [39].

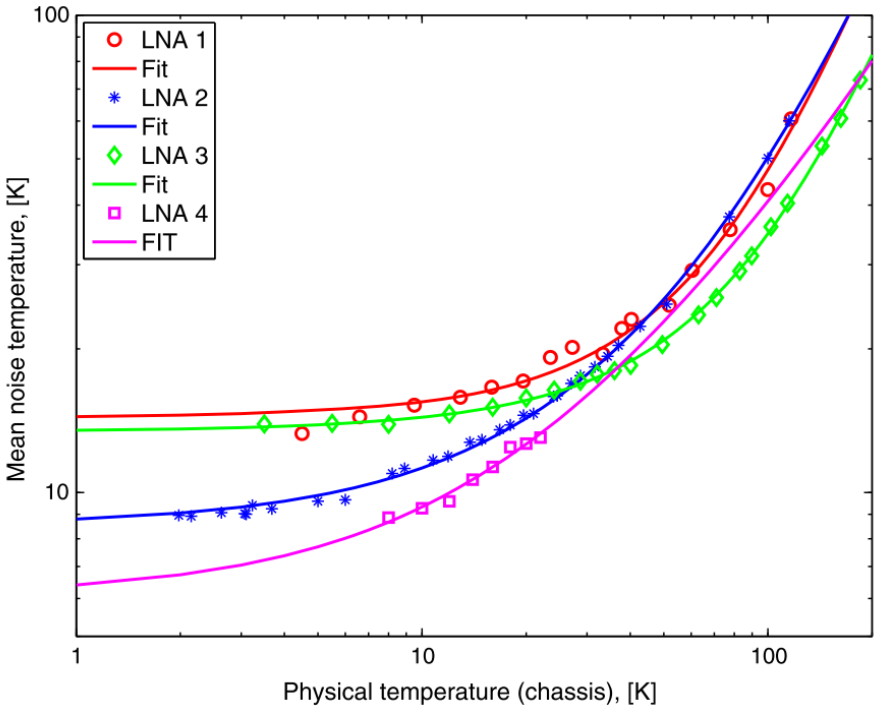

Figure 2.17. The relationship between physical case temperature and mean T_e for a cryogenic LNA [39].

2.3 Chapter conclusion

The first half of this chapter dealt with concepts around the phenomenon of noise in electrical circuits, including a description of the terms: equivalent noise temperature (T_e), cascaded power gain and equivalent noise temperature of a cascade (T_{cas}).

The second half of this chapter discussed topics relating to the sensitivity of a radio telescope element. The description of a radio telescope array element was followed by a discussion of the radiometer equation and the minimum detectable flux density as well as the effective aperture (A_e) and the system temperature (T_{sys}). The final two sections gave a brief description of the MeerKAT receiver and the UHF-band LNA in the context of the receiver, and ultimately, in the context of the radio telescope. Figure 2.18 shows the radio telescope antenna element

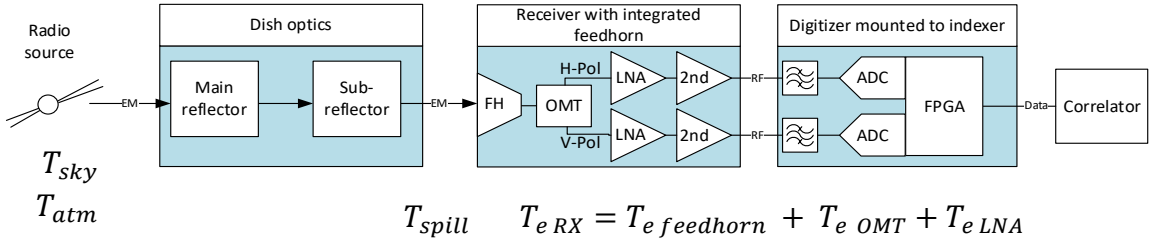

Figure 2.18. The block diagram of a radio telescope antenna element. The T_{sys} components are shown [32].

The relevant background information has been presented and the reader should be familiar with the concepts as they are used in the remainder of this thesis. The importance of the T_e performance of the LNAs to the radio telescope array element should now be evident. An appropriate measurement method should be selected that will allow accurate measurement of T_e of the LNA. To be able to perform T_e measurements on the UHF-band LNA, the following will be presented in the next chapter:

- An extensive literature survey and a suitable LNA equivalent noise temperature measurement method will be selected.
- The measurement method will have a suitable uncertainty to be able to measure T_e of 0.6 K across the band.
- The measurement method will make use of the existing receiver hardware and test system as far as possible.

Chapter 3

LNA T_e measurement methods

3.1 Introduction

The goal of this chapter is to present the different low noise amplifier equivalent noise temperature measurement methods that were investigated and discuss the suitability of each method. The theoretical ideal measurement case is presented, and the challenges that prevent this from being realised are discussed. The Y-factor measurement method is presented followed by improvements that address issues with the Y-factor method. The cold source measurement method is discussed along with a variation of the cold source method that makes use of a variable temperature source. The measurement of noise using a VNA is also possible, and this is briefly discussed. Finally, the cold attenuator measurement method is presented, followed by a summary and comparison of methods.

Commonly used terms:

- Delta (Δ) is used to denote the uncertainty of a term.
- Second stage is used to denote the stages after the AUT. This normally includes the output transmission line, test cable and noise figure analyser.

3.2 LNA equivalent noise temperature measurement – The ideal case

Theoretically, if the input of the AUT could be terminated with a passive termination that had a physical temperature (T_{phys}) of 0 K, then the noise temperature measured at the output of the AUT would be $T_{meas} = T_{e\ AUT} G_{a\ AUT}$ [21][40].

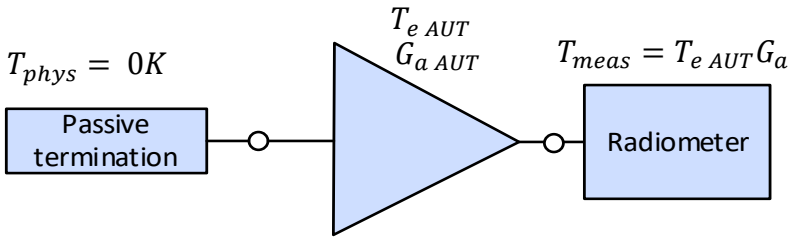

Figure 3.1. Measurement of $T_{e\ AUT}$ using a 0 K load and lossless radiometer [21].

This theory is not able to be realized. Firstly, it is not possible to cool the passive termination to 0 K [21]. Secondly, the input and output transmission lines (TX lines) will have their own T_e and G_a contributions. Finally, the radiometer has its own T_e and G_a contribution. Adding in all these factors results in Figure 3.2 and equation (3.1).

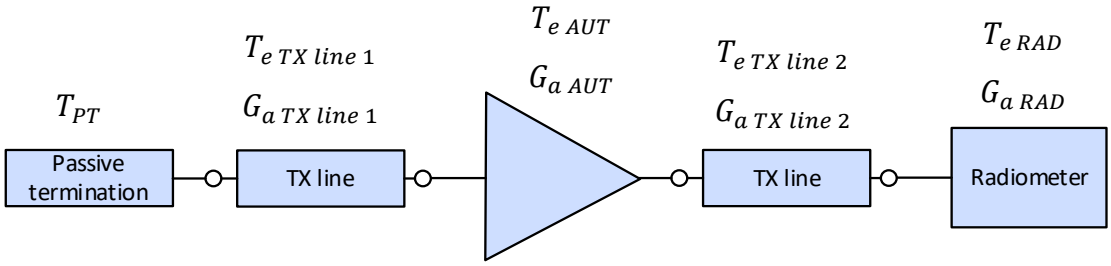

Figure 3.2. Measurement of T_e using a ambient load, transmission lines and a lossy radiometer [21].

The value measured by the radiometer can be expressed by this equation:

$$T_{meas} = ((((((T_{PT} + T_{e\ TX\ line\ 1})G_{a\ TX\ line\ 1}) + T_{e\ AUT})G_{a\ AUT} + T_{e\ TX\ line\ 2})G_{a\ TX\ line\ 2}) + T_{e\ RAD})G_{a\ RAD} \quad (3.1)$$

Where:

- T_{meas} is the noise temperature measured by the radiometer in K.
- T_{PT} is the noise temperature of the passive termination in K.
- $T_{e\ TX\ line\ 1}$ is the T_e of the input TX line in K.
- $G_{a\ TX\ line\ 1}$ is the available gain of the input TX line in W/W.
- $T_{e\ AUT}$ is the T_e of the AUT in K.
- $G_{a\ AUT}$ is the available gain of the AUT in W/W.

- $T_{e\ TX\ line\ 2}$ is the T_e of the output TX line in K.
- $G_{a\ TX\ line\ 2}$ is the available gain of the output TX line in W/W.
- $T_{e\ RAD}$ is the T_e of the radiometer in K.
- $G_{a\ RAD}$ is the available gain of the radiometer in W/W.

It is no trivial feat to de-embed the $T_{e\ AUT}$ from equation (3.1) based on a single measurement, therefore, several methods for measuring the $T_{e\ AUT}$ are described and listed in this chapter. These methods include:

- The classic Y-factor method.
- The corrected Y-factor method.
- The cold source method.
- A variable temperature cold source method.
- Vector network analyser method
- The cold attenuator method.

3.3 The classic Y-factor method

The classic Y-factor method uses two noise sources at significantly different equivalent noise temperature values, called the hot noise temperature (T_h) and the cold noise temperature (T_c). The noise sources can be active or passive, but the values for T_h and the T_c should be accurately known.

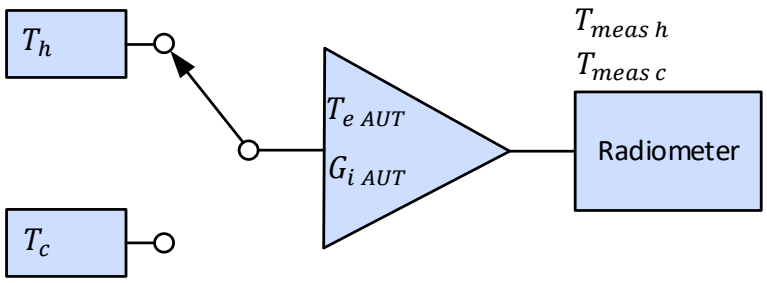

Figure 3.3. A simplified diagram of the classic Y-factor measurement method [21].

The first step is to measure the noise power (P_n) on the radiometer with the T_h coupled to the input of the AUT. The next step is to measure the P_n on the radiometer with the T_c coupled to the input of the AUT. These measured power values are called $P_{meas\,h}$ and $P_{meas\,c}$ respectively. The equivalent noise temperature of the AUT ($T_{e\,AUT}$) may be calculated using the following equations [21][40][41][42][43][44]:

$$Y = \frac{(T_{e\,AUT} + T_h)G_{i\,AUT}}{(T_{e\,AUT} + T_c)G_{i\,AUT}} = \frac{T_{meas\,h}}{T_{meas\,c}} = \frac{T_{e\,AUT} + T_h}{T_{e\,AUT} + T_c} \tag{3.2}$$

The Y-factor ratio can also be calculated using the measured power in watts:

$$Y = \frac{P_{meas\,h}}{P_{meas\,c}} \tag{3.3}$$

Rearranging equation (3.2) and performing algebraic manipulation:

$$Y(T_{e\,AUT} + T_c) = T_{e\,AUT} + T_h$$

$$YT_{e\,AUT} + YT_c = T_{e\,AUT} + T_h$$

$$YT_{e\,AUT} - T_{e\,AUT} = T_h - YT_c$$

$$T_{e\,AUT}(Y - 1) = T_h - YT_c$$

The resultant equation can be used to find the equivalent noise temperature of the AUT:

$$T_{e\,AUT} = \frac{T_h - YT_c}{Y - 1} \tag{3.4}$$

The insertion gain of the amplifier under test can determined using the equation [21][40][41][42][43][44]:

$$G_{i\,AUT} = \frac{T_{meas\,h} - T_{meas\,c}}{T_h - T_c} \tag{3.5}$$

Where:

- Y is the ratio of the output noise temperature measurements.

- $T_{e\ AUT}$ is the equivalent noise temperature of the AUT in K.
- T_h is the known noise temperature of the hot load in K.
- T_c is the known noise temperature of the cold load in K.
- $T_{meas\ c}$ is the measured noise temperature when T_c is attached to the input port in K.
- $T_{meas\ h}$ is the measured noise temperature when $\mathrm{T_h}$ is attached to the input port in K.
- $P_{meas\ c}$ is the measured noise power when the T_c is attached to the input port in W.
- $P_{meas\ h}$ is the measured noise power when the T_h is attached to the input port in W.
- $G_{i\ AUT}$ is the insertion gain of the AUT in W/W.

Figure 3.4 shows a graphical representation of the Y-factor calculation. The blue dot represents the hot measurement and is plotted with the measured $P_{meas\ h}$ value on the y-axis with the known T_h value on the x-axis. The orange dot represents the cold measurement and is plotted with the measured $P_{meas\ c}$ value on the y-axis with the known T_c value on the x-axis. The y-intercept point is the point where the source noise temperature equals 0 K. If a line is drawn through the two measured points, then the y-intercept can be extrapolated [42].

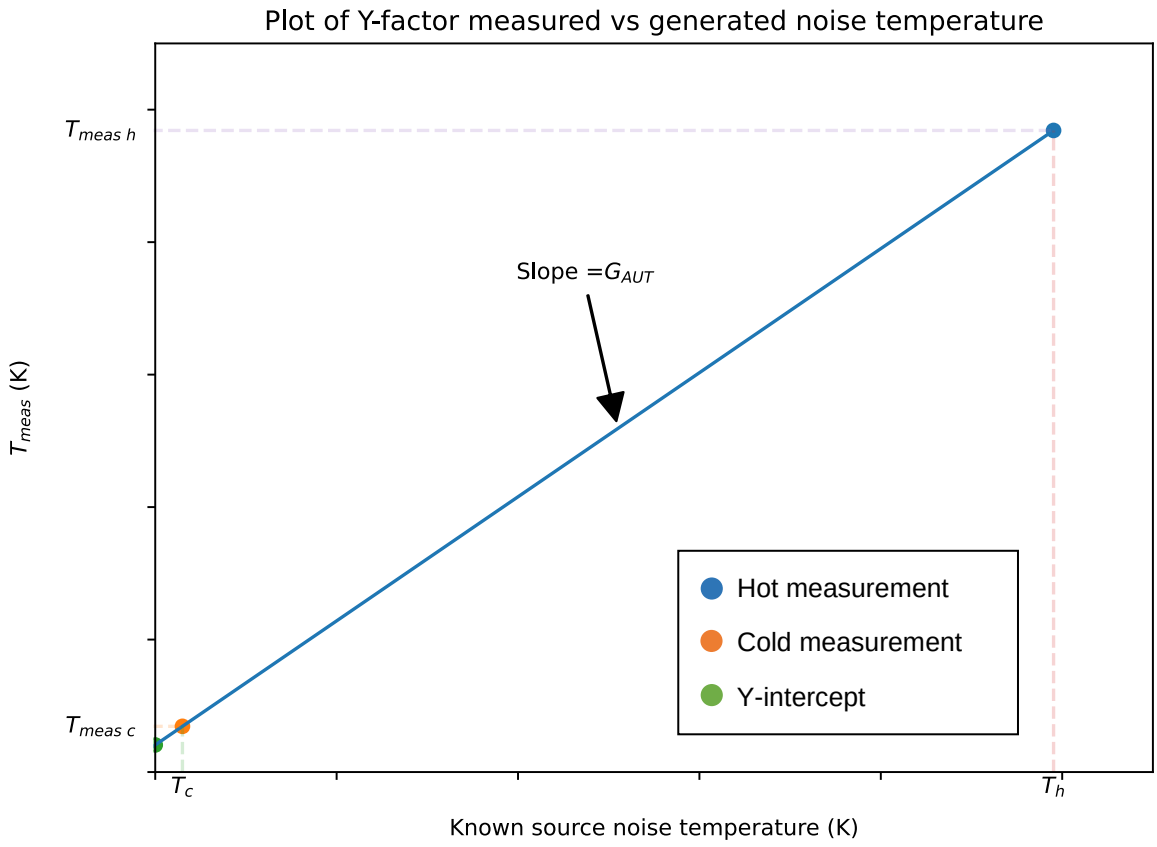

Figure 3.4. Graph showing the measured equivalent noise temperature versus the noise source equivalent noise temperature values.

The equivalent noise temperature can be found by extrapolation of the graph to the y-intercept. This is the green point on the Figure 3.4, where the equivalent noise temperature of the source is zero and the measured power is generated by the AUT.

$$y - intercept\ = (T_{e\ AUT})G_{i\ AUT} \tag{3.6}$$

The gradient of the graph can be used to determine the insertion gain (G_i) using the equation [40][42]:

$$\frac{dy}{dx} = \frac{T_{meas\ h} - T_{meas\ c}}{T_h - T_c} \tag{3.7}$$

But the measured noise temperature consists of the following:

$$\begin{aligned} T_{meas\ h} &= (T_{e\ AUT} + T_h)G_{i\ AUT} \\ T_{meas\ c} &= (T_{e\ AUT} + T_c)G_{i\ AUT} \end{aligned} \tag{3.8}$$

When equation
(3.8) is substituted into equation (3.7) and algebraic manipulation is performed:

$$\frac{dy}{dx} = \frac{T_{meas\,h} - T_{meas\,c}}{T_h - T_c} = \frac{(T_{e\,AUT} + T_h)G_{i\,AUT} - (T_{e\,AUT} + T_c)G_{i\,AUT}}{T_h - T_c}$$

$$\frac{dy}{dx} = \frac{G_{i\,AUT}T_{e\,AUT} + G_{i\,AUT}T_h - G_{i\,AUT}T_{e\,AUT} - G_{i\,AUT}T_c}{T_h - T_c}$$

$$\frac{dy}{dx} = \frac{G_{i\,AUT}(T_{e\,AUT} + T_h - T_{e\,AUT} - T_c)}{T_h - T_c}$$

$$\frac{dy}{dx} = G_{i\,AUT} \tag{3.9}$$

Where:

- $G_{i\,AUT}$ is the insertion gain of the AUT in W/W.

Equation (3.9) shows that the slope of the Figure 3.4 is equal to the gain of the amplifier under test. The classic Y-factor method requires all components to be well matched and a large difference between the T_{hot} and the T_{cold} [45].

3.3.1 Removing the second stage effect from the cascade

In most classic Y-factor measurements, the result is not only the T_e of the AUT ($T_{e\,AUT}$), but the T_e of the cascade ($T_{e\,cas}$) consisting of the AUT, test cables, pre-amplifier and radiometer. To calculate the $T_{e\,AUT}$, second stage correction is employed. Figure 3.5 shows a classic Y-factor measurement using a calibrated noise diode as the noise source. The noise diode may be coupled directly to the input port of the AUT and provides two noise temperature values.

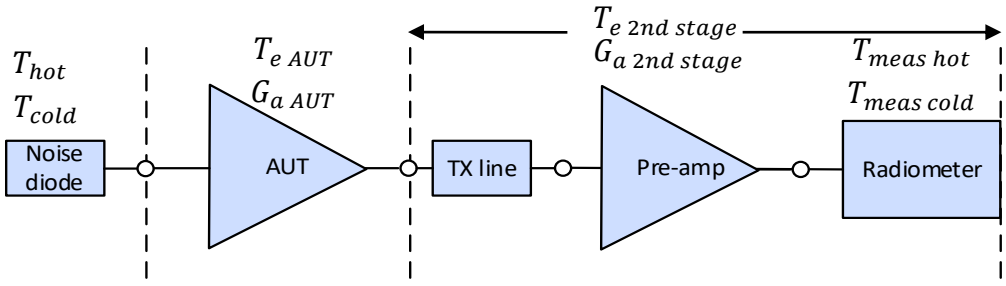

Figure 3.5. Measurement of T_e using a noise diode, transmission lines and a lossy radiometer [21].

The equivalent noise temperature of the second stage is measured on its own. A classic Y-factor measurement is performed on the second stage as per Figure 3.6.

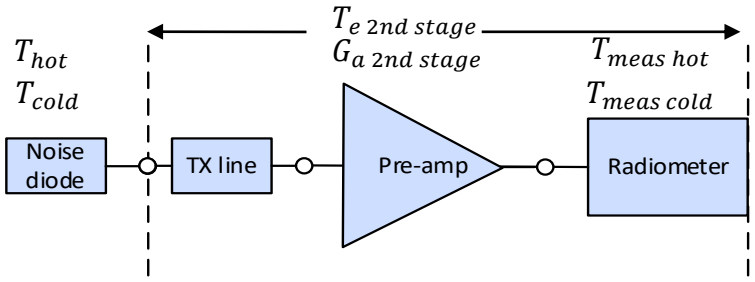

Figure 3.6. Measurement of the $T_{e\ 2nd\ stage}$ using a noise diode [42].

Friis formula given in equation (2.12) is used to determine $T_{e\ AUT}$ from the $T_{e\ cas}$ [40][42]:

$$T_{e\ AUT} = T_{e\ cas} - \frac{T_{e\ 2nd\ stage}}{G_{a\ AUT}} \tag{3.10}$$

Where:

- $T_{e\ AUT}$ is the T_e of the AUT in K.
- $T_{e\ cas}$ is the T_e of the AUT and second stage in K.
- $T_{e\ 2nd\ stage}$ is the T_e of the second stage in K.
- $G_{a\ AUT}$ is the available gain of the AUT in W/W.

The gain of the amplifier under test ($G_{a\ AUT}$) is determined by a VNA measurement.

Referring to equation (3.10), if the gain of the amplifier under test ($G_{a\ AUT}$) is sufficiently large, then the 2nd stage contribution will be very small. If $G_{a\ AUT}$ is small then a low noise pre-amplifier is added after the AUT to decrease the 2nd stage contribution [42].

3.4 The corrected Y-factor method

3.4.1 Improvements to the 2nd stage correction

Vondran (1999) describes two issues pertinent to the classic Y-factor measurement, namely using the incorrect gain definition (Available gain G_a versus insertion gain G_i) for removing

the 2nd stage effect from the cascade and matching between networks. Making the incorrect assumptions about the above two points may lead to significant errors in the final $T_{e\ AUT}$ value [24].

Molina (2019) already suggested that using the simple Y-factor method on an AUT results in errors. They derived expressions to estimate the error limits with and without an isolator after and before the AUT. They showed that errors may be as high as ± 0.74 dB when measuring a 1 dB NF amplifier with no input isolator. They declared that the measurement errors are dominated by mismatches. Mismatches are caused when there is a difference between the source and load impedances in a component cascaded. The mismatches are measured using a vector network analyser (VNA), which measures both the magnitude and phase. These are used to calculate the G_a for the second stage correction [27].

Additionally, the equivalent noise temperature of the radiometer is strongly dependent on the source impedance presented to its input port.

3.4.2 Problem with the 2nd stage correction:

Adapting equation (2.10) to illustrate the issue with the output matching of the AUT:

$$G_{a\ AUT} = \frac{P_{avn}}{P_{avs}} = \frac{|S_{21}|^2(1-|\Gamma_s|^2)}{|1-S_{11}\Gamma_s|^2(1-|\Gamma_{out}|^2)} \tag{3.11}$$

Referring to equation (3.11), the term related to the AUT output matching $(1-|\Gamma_{out\ AUT}|^2)$ becomes the dominant term as the AUT output match degrades. This means that the available gain of the AUT approaches infinity as the output reflection coefficient approaches 1 and this error also strongly depends on the phase of the output reflection coefficient [27].

Analysing equation (3.10) and denoting which terms are a function of the output reflection coefficient of the AUT ($\Gamma_{out\ AUT}$) and the source reflection coefficient presented by the noise source (Γ_s) using brackets [27]:

$$T_{e\ AUT}(\Gamma_{out\ AUT}) = T_{cas}(\Gamma_{out\ AUT}) - \frac{T_{e\ 2nd\ stage}(\Gamma_s)}{G_{a\ AUT}(\Gamma_{out\ AUT})}$$

The first thing to note is that the second stage equivalent noise temperature ($T_{e\ 2nd\ stage}$) is measured without the AUT in place as shown in Figure 3.7. This means that it is a function of the source reflection coefficient of the noise source (Γ_s) and not the output reflection coefficient of the AUT ($\Gamma_{\text{out AUT}}$). The second stage equivalent noise temperature is not identical when the different reflection coefficients Γ_s and $\Gamma_{\text{out AUT}}$ are presented to its input port. As the value of $T_{e\ 2nd\ stage}(\Gamma_s)$ diverges from $T_{e\ 2nd\ stage}(\Gamma_{out\ AUT})$ the error contributed by this term increases.

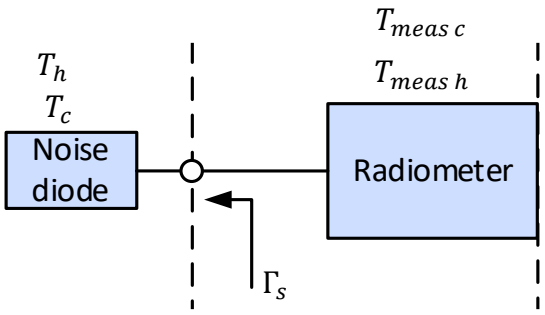

Figure 3.7. Y-factor measurement of $T_{e\ 2nd\ stage}$ using a noise diode is a function of Γ_s [27].

$G_{a\ AUT}$ and T_{cas} are determined with the AUT in the cascade as shown in Figure 3.8 where the output reflection coefficient of the AUT ($\Gamma_{out\ AUT}$) is presented to the second stage input port.

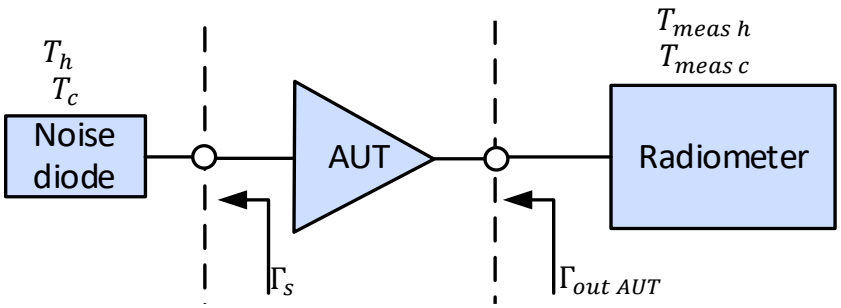

Figure 3.8. Y-factor measurement of $T_{e\ cas}$ is a function of $\Gamma_{out\ AUT}$ [27].

Thus to minimise the error caused by the change in equivalent noise temperature of the second stage with different impedances presented to its input port, the gain of the AUT can be increased or the matching between the AUT and the second stage can be improved using an attenuator or isolator between the AUT and the second stage.

The corrected Y-factor method does not correct for all mismatch as illustrated in Figure 3.9. An AUT with a high mismatch presented at its output port and low values of $G_{i\,AUT}$ will result in significant errors regardless of the method used. Higher $G_{i\,AUT}$ with lower AUT $|S_{22}|$ values result in reduced error [27].

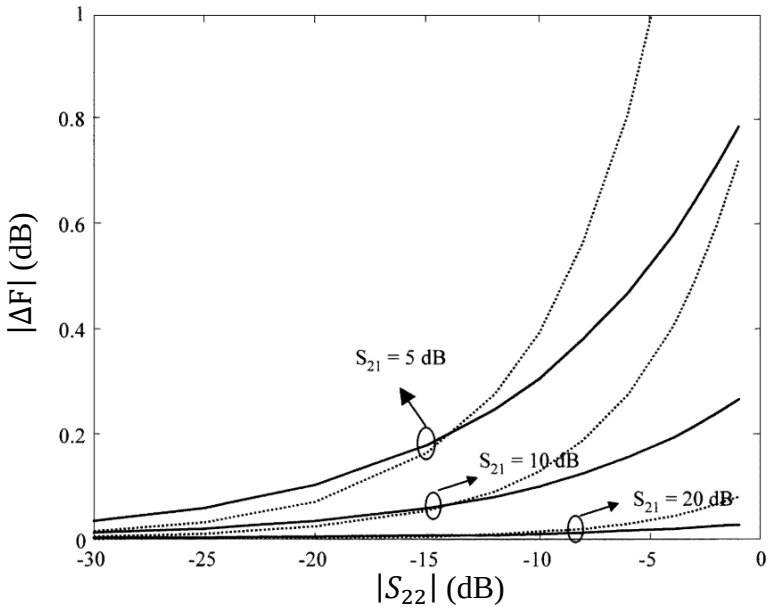

Figure 3.9. Noise factor error (ΔF) versus AUT output return loss. Three values of S_{21} are shown. Note that $G_{i\,AUT} = |S_{21}|$ (dB) in the diagram. The solid line is the classic Y-Factor method, dashed line is the corrected Y-factor method [27].

Isolators or attenuators used between the AUT and the radiometer or the 2nd stage can minimise the error that the mismatch causes. In particular, the input of the radiometer should be isolated to reduce the difference in the T_e of the radiometer itself when different impedances are presented to the radiometer.

3.4.3 Noise source impedance changes between on and off state

The noise diode and the excess noise ratio (ENR) is dealt with in more detail in section 4.3.1. The heart of an active noise source is an avalanche diode that is biased when the noise source is switched on (T_h) and unbiased when the noise source is switched off (T_c). An attenuator is built into the noise source to diminish the effect of the change in the impedance between the two states [24].

The measured reflection coefficient for both states of the 346B noise source is presented in Figure 3.10. The reader should note that the importance is the difference between the states. The effect of this is that the available gain of the amplifier under test ($G_{a\ AUT}$) will be different between the on and off states of the noise source[6].

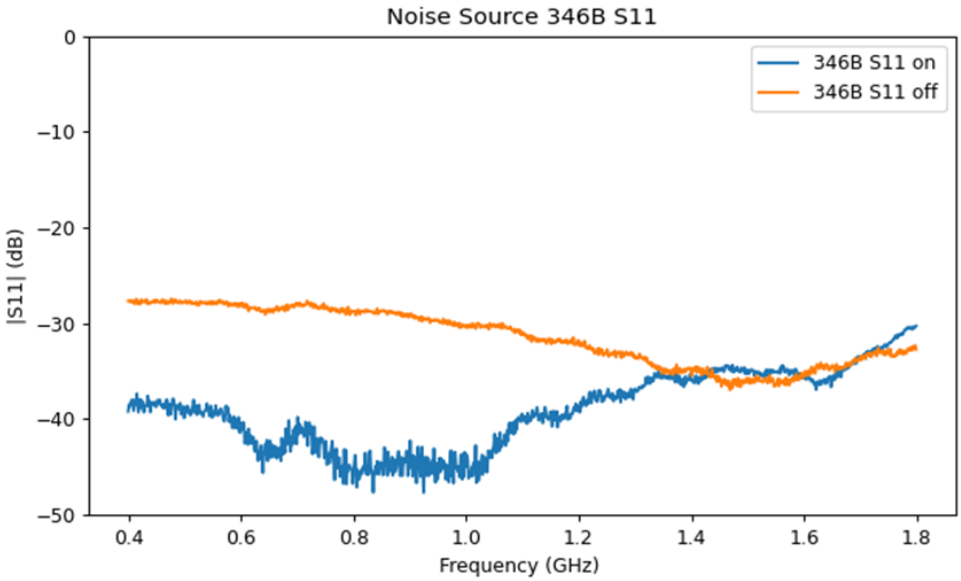

Figure 3.10. The difference in return loss between hot and cold states of the noise source.

Molina (2019) states that for the Y-factor low-noise amplifier measurements, one of the main causes of error is the variation in the output impedance between the noise diode switched on and switched off. The Y-factor equation (3.4) assumes that the mismatch between the noise source and the AUT is identical between the on and off states. The effect of the variation can be lessened by including a well characterised isolator or attenuator between the noise source output and the AUT input. This results in a reduced impedance mismatch between the AUT and noise diode output [27][46].

3.5 The cold source measurement method

After 1990, the classic Y-factor method that requires the use of isolators was no longer seen as a viable measurement method and the cold source method was adopted [47].

[6] This difference is shown in the plot of the measured available gain of the AUT in Figure 5.26. Note that in this plot, the attenuator between the noise source and the AUT reduces the difference to insignificance.

Randa *et al.* (2006) and Gu *et al.* (2013) describe a measurement method developed at the National Institute of Standards and Technology (NIST). Figure 3.11 illustrates the cold source measurement method. This method uses a cryogenically-cooled passive termination with a physical temperature that is as low as possible. This cold source is coupled directly to the input of the AUT. A radiometer is used to measure the noise temperature at the output of the AUT [23][48].

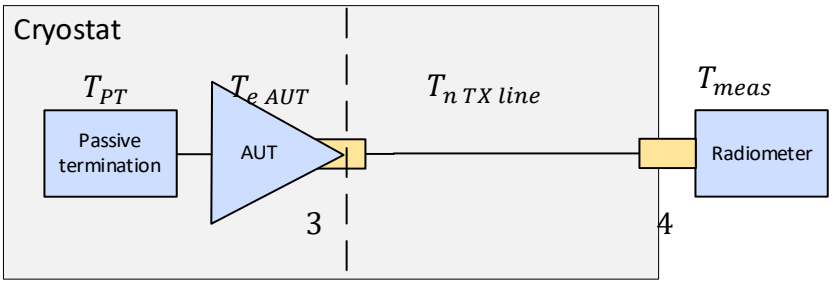

Figure 3.11. Measuring the T_e of the AUT using the cold source method [23][48][49].

This method has shown to have extremely low measurement uncertainty provided that the radiometer and transmission line G_a and T_e characteristics are accurately known. The cold source measurement method has two advantages over the classic Y-factor method, namely [23][48][49]:

- The passive termination has a high return loss. This reduces the uncertainty due to the mismatch between the output port of the noise source and the input port of the AUT.
- A noise diode is not used for the AUT measurement, thus the noise diode ENR uncertainty is not part of the measurement uncertainty.

Figure 3.12 shows the cold source measurement setup used by Gu *et al.* (2013).

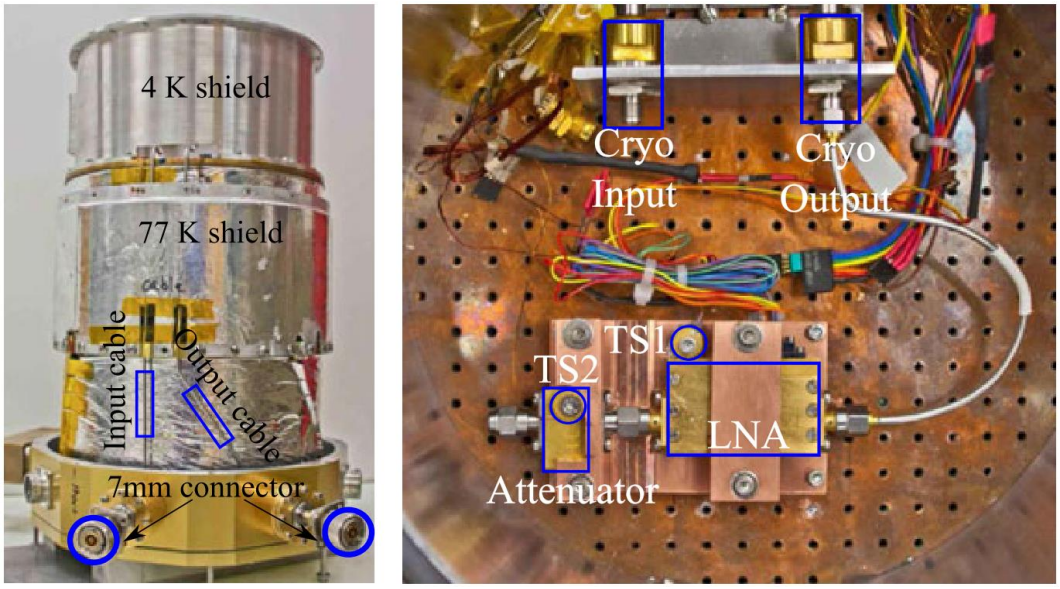

Figure 3.12. The open cycle liquid helium cryostat used by Gu *et al.* (2013). TS1 and TS2 are temperature sensors [49].

3.5.1 Transmission line property extraction

The low loss coaxial transmission (TX) lines are used to connect the ambient temperature vacuum feedthroughs to the AUT. These cables can be chosen to utilise a stainless-steel outer conductor in order to minimise the thermal conductance between the cold head and the ambient temperature outer wall of the cryostat. Thus, they have a large temperature gradient across them which makes analytical determination of loss and noise a complex issue.

Transmission line gain determination

The TX line characterisation measurement used in Gu *et al.* (2013) is shown in Figure 3.13. The TX lines are connected using a short low loss jumper cable and a standard Y-factor measurement is carried out.

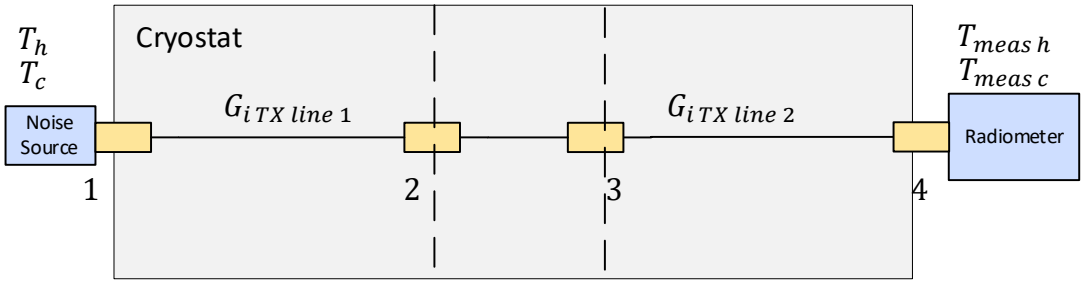

Figure 3.13. Setup for measuring G_i (<1) through TX lines [23][48][49].

An adapted form of equation (3.5) is used [49]:

$$G_{i\,TX\ line\ 1}G_{i\,TX\ line\ 2} = \frac{T_{meas\,h} - T_{meas\,c}}{T_h - T_c} \tag{3.12}$$

Where:

- $G_{i\,TX\ line\ 1}G_{i\,TX\ line\ 2}$ is the G_i (<1) of TX line 1 in series with TX line 2 in W/W.
- $T_{meas\,h}$ is the noise temperature measured by the radiometer when T_h is connected to port 1 in K.
- $T_{meas\,c}$ is the noise temperature measured by the radiometer when T_c is connected to port 1 in K.
- T_h is the noise temperature of the hot load in K.
- T_c is the noise temperature of the cold load in K.

The TX lines are chosen to be well matched so that the following assumption can be made in order to determine the individual TX line gain values [49]:

$$G_{i\,TX\ line\ 1} = G_{i\,TX\ line\ 2} = \sqrt{G_{i\,TX\ line\ 1}G_{i\,TX\ line\ 2}} \tag{3.13}$$

Transmission line noise temperature

The noise temperature of the transmission line ($T_{n\,TX\ line\ 1}$ or $T_{n\ TX\ line\ 2}$) will add directly to the noise temperature of the cooled passive termination (T_{PT}). The measurements are performed as per Figure 3.14 and Figure 3.15 to determine the TX line noise temperature contribution. These measurements require a well characterised radiometer with sufficient gain and stability in order to be useful. Randa *et al.* (2006) and Gu *et al.* (2013) demonstrated this using a purpose-built radiometer named NFRad [23][48][49].

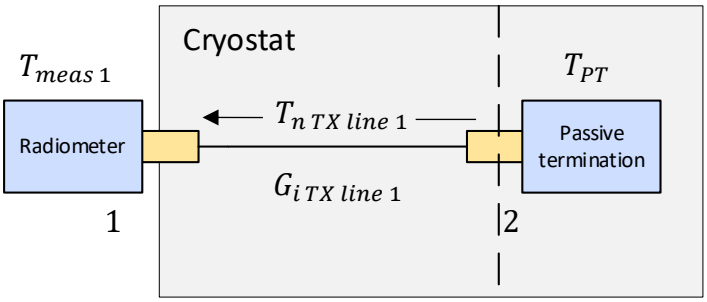

Figure 3.14. Measuring the noise added by the TX line 1 [23][48][49].

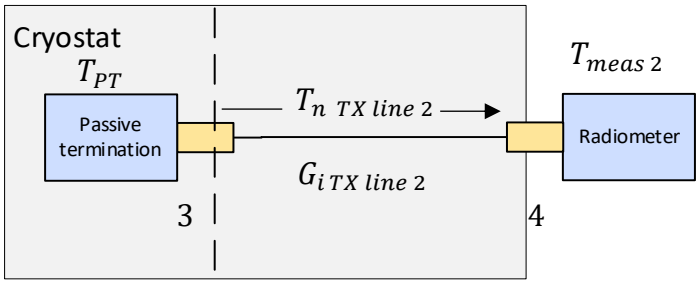

Figure 3.15. Measuring the noise added by the TX line 2 [23][48][49].

Equation (2.8) is adapted to measurements shown in Figure 3.14 and Figure 3.15 to build the following equations [49]:

$$T_{n\,TX\,line\,1} = T_{meas\,1} - G_{i\,TX\,line\,1}T_{PT} \tag{3.14}$$

$$T_{n\,TX\,line\,2} = T_{meas\,2} - G_{i\,TX\,line\,2}T_{PT} \tag{3.15}$$

Where:

- $G_{i\,TX\,line\,1}$ is the G_i (<1) of TX line 1 in W/W.
- $G_{i\,TX\,line\,2}$ is the G_i (<1) of TX line 2 in W/W.
- $T_{meas\,1}$ is the T_n measured with the radiometer connected to port 1 with the T_{PT} connected to port 2 in K.
- $T_{meas\,2}$ is the T_n measured with the radiometer connected to port 4 with the T_{PT} connected to port 3 in K.
- T_{PT} is the T_n available from the cold passive termination calculated using formula (2.8) in K.

Note that the $T_{n\,TX\ line\ 1}$ measured from point 2 to 1 does not equal the $T_{n\,TX\ line\ 1}$ measured from point 1 to 2. The TX line can be seen as a distributed cascade of varying physical temperature. In the cascade it matters what order the elements with the different T_n values are located [49].

3.5.2 AUT Measurement of G_a and T_e

The three AUT measurements are described in this section. The first is a Y-factor measurement shown in Figure 3.16 used to determine the gain of the whole cascade.

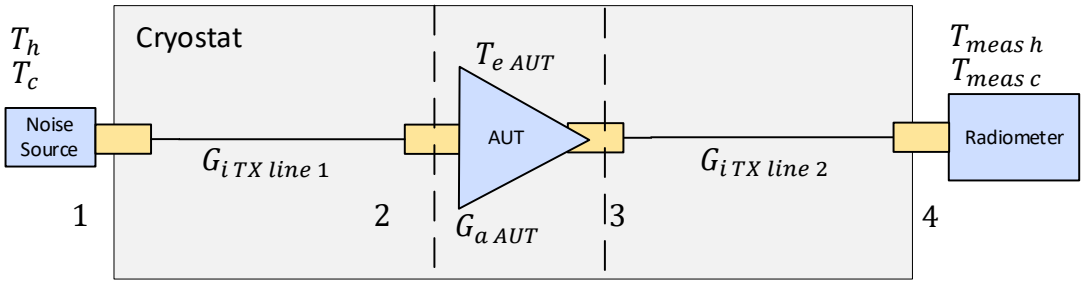

Figure 3.16. Measurement of G_a [23][48][49].

During the cold source measurements shown in Figure 3.17 and Figure 3.18 an excellent match is presented by the passive termination, thus it is assumed that the source reflection coefficient (Γ_s) is zero. This results in a simplified equation (3.16) to determine the $G_{a\ AUT}$. This equation (3.11) given in Gu *et al.* (2013) shows how the available gain of the AUT ($G_{a\ AUT}$) can be determined from the gain of the whole cascade taken in the measurement shown in Figure 3.16. Only the output reflection coefficient of the AUT ($\Gamma_{out\ AUT}$) needs to be known [49]:

$$G_{i\,TX\ line\ 1}G_{i\,TX\ line\ 2}G_{a\ AUT} = \frac{T_{meas\ h} - T_{meas\ c}}{T_h - T_c}\frac{1 - |\Gamma_{out\ AUT}|^2}{1 - (|\Gamma_{out\ AUT}|^2 / G_{i\,TX\ line\ 1}G_{i\,TX\ line\ 2})} \qquad (3.16)$$

Where:

- $G_{i\,TX\ line\ 1}$ is the G_i (<1) of the TX line 1 in W/W.
- $G_{i\,TX\ line\ 2}$ is the G_i (<1) of the TX line 2 in W/W.
- $G_{a\ AUT}$ is the G_a (>>1) of the AUT in W/W.
- $\Gamma_{out\ AUT}$ is the output reflection coefficient of the AUT.

The final two measurements, shown in Figure 3.17 and Figure 3.18 are carried out in order to determine the $T_{e\ AUT}$.

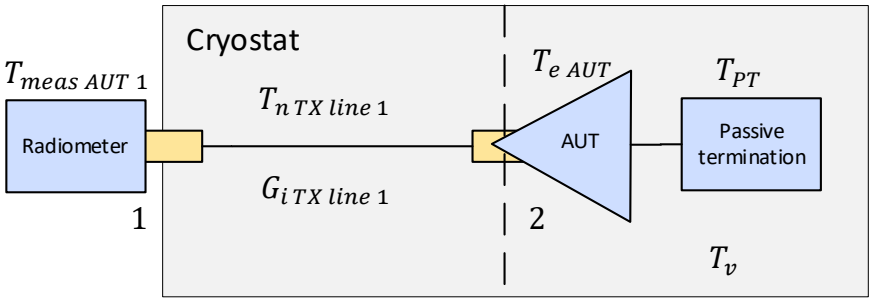

Figure 3.17. Measuring the $T_{meas\ AUT\ 1}$ [23][48][49].

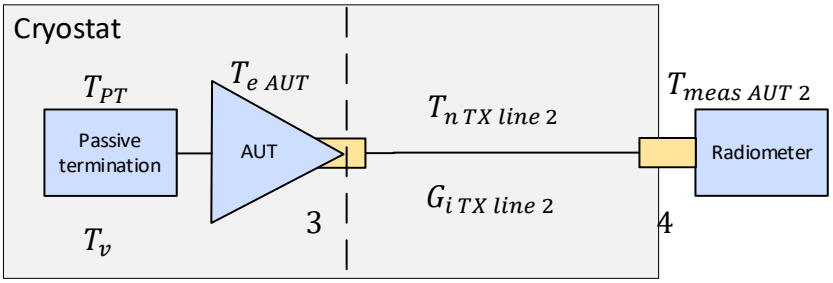

Figure 3.18. Measuring the $T_{meas\ AUT\ 2}$ [23][48][49].

For the final measurements a different definition for T_n than that presented in formula (2.5) and (2.8) is described by the equation [23]:

$$T_{meas} = G_{a\ AUT}(T_{PT} + T_{e\ AUT} + T_V) \tag{3.17}$$

Where:

- T_{meas} is the noise temperature measured at the output port in K.
- $G_{a\ AUT}$ is the available gain of the amplifier in W/W.
- T_{PT} is the noise temperature of the passive termination in K.
- $T_{e\ AUT}$ is the effective noise temperature of the AUT in K.

The term T_V is to account for the noise added by the random vacuum fluctuations and can be described by the equation:

$$T_V = \frac{hf}{2k} \tag{3.18}$$

Where

- T_V is the noise temperature added at the amplifier input by vacuum fluctuations in K.
- $h = 6.62607015 \times 10^{-34}$ is Planck's constant in J/Hz.
- f is the center frequency of the bandwidth in Hz.
- $k = 1.380\ x\ 10^{-23}$ is Boltzmann's constant in J/K.

The T_e of the AUT can be calculated using the equation derived by Randa *et al.* (2006) and Gu *et al.* (2013) [23][49]:

$$T_{e\ AUT} = \sqrt{\frac{(T_{meas\ AUT\ 1} - T_{n\ TX\ line\ 1})(T_{meas\ AUT\ 2} - T_{n\ TX\ line\ 2})}{G_{i\ TX\ line\ 1} G_{i\ TX\ line\ 2} G_{a\ AUT}}} - T_{PT} - T_V \tag{3.19}$$

Where:

- $T_{e\ AUT}$ is the equivalent noise temperature of the AUT in K.
- $T_{meas\ AUT\ 1}$ is the noise temperature measured in Figure 3.17 in K.
- $T_{meas\ AUT\ 2}$ is the noise temperature measured in Figure 3.18 in K.
- $T_{n\ TX\ line\ 1}$ is the noise temperature added by the TX line measured in Figure 3.14.
- $T_{n\ TX\ line\ 2}$ is the noise temperature added by the TX line measured in Figure 3.15.

Gu *et al.* (2013) uses a very comprehensive uncertainty analysis to calculate ±0.3 K as the uncertainty for this method. This is the lowest uncertainty quoted for any measurement method; however, the trade-off is that it requires six cool-heat cycles for the calibration of the test setup and initial measurement. Thereafter each measurement requires three cool-heat cycles per $T_{e\ AUT}$ measurement. The authors admit that this method is not quick, efficient, or easy. Additionally, it requires a custom-made attenuator to avoid thermal gradients. Lastly, a very stable, well characterised radiometer is required. Gu *et al.* (2013) uses the NFRad that was designed and built for this purpose. Table 3.1 shows the cold source measurements found in the literature for comparison. Note that the measurement uncertainty of the noise temperature of the AUT is below 0.33 K for all measurements [49].

Table 3.1. Cold source measurement method comparisons.

Source	Frequency (GHz)	AUT Gain (dB)	T_{phys} (K)	$T_{e\ AUT}$ (K)	$\Delta T_{e\ AUT}$ (K)
Gu *et al.* (2013) [49]	4-8	44	4	<2	0.18 - 0.33
Randa *et al.* (2006) [23]	1-11	33.4-35.8	4	<5.5	0.3

Gu *et al.* (2013) suggested the following improvements to the passive termination to reduce uncertainty:

- A more isothermal passive termination to lower the temperature gradient.
- A matched passive termination with a higher reflection loss.
- Integrating the temperature sensor into the body of the passive termination.
- Measuring the physical temperature as close as possible to the actual termination element.
- Adding a heating element to the passive termination will allow a few reference noise temperatures directly to the AUT [49].

3.6 The cold source measurement method with a variable temperature source

This method is a variation on the cold source method. Simbierowicz *et al.* (2021) present a noise source with an integrated heating element that can vary its thermal noise temperature from 0.1 K to 5 K without causing heat transfer to the other components [50].

A room temperature LNA with a T_e of 10 K was tested by Simbierowicz *et al.* (2021) using this measurement method as illustrated in Figure 3.19 [51].

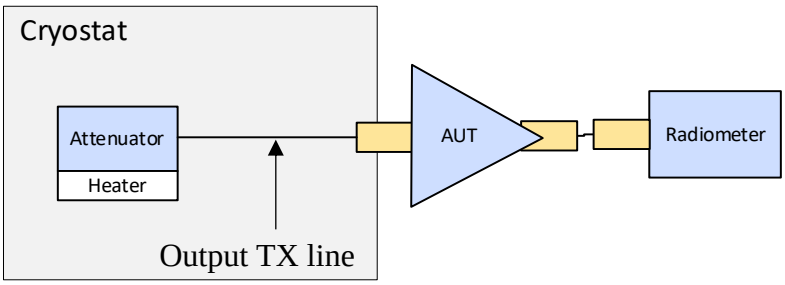

Figure 3.19. The cold source measurement method with a variable temperature attenuator with the AUT outside the cryostat [51].

Gu *et al.* (2013) suggested that adding an integrated heating element to the passive termination will allow a few reference noise temperature values to be applied directly to the AUT input as an improvement to the cold source method. This concept is shown in Figure 3.20 [49].

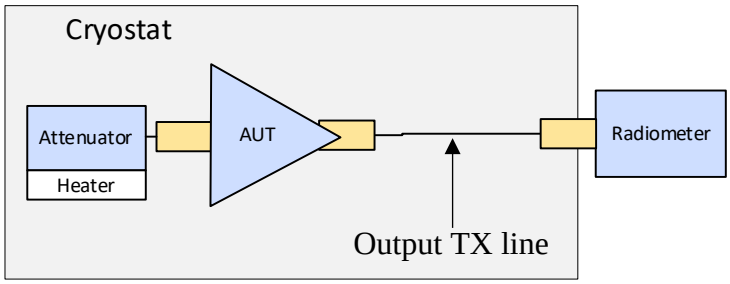

Figure 3.20. The cold source measurement method with a variable temperature attenuator connected directly to the AUT input port [49].

This could be considered as a future improvement if the cold source method is selected.

3.7 Noise measurement with a vector network analyser

Russell (2013) gives a description of another way of representing the noise in a two-port network known as noise wave analysis. Figure 3.21 shows the noise wave B_s originating from the source. The imperfect matching at the input of the noiseless network results in the source noise wave (B_s) being separated into the noise wave reflected back towards the source (B_n) and the noise wave incident on the network (A_n) [52].

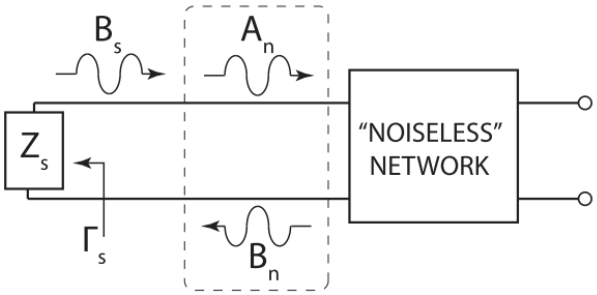

Figure 3.21. S-parameter measurement including the source noise wave B_s, the incident noise wave A_n and the reflected noise wave B_n [52].

A vector network analyser (VNA) with a built-in noise receiver is able to perform measurements based on the cold-source technique. The benefit of this method is that the noise can be measured for many different values of the source and the load impedance, which is beneficial for determining the optimum matching for a low noise transistor when designing a low noise amplifier [53][54].

This method is able to extract the noise parameters of an amplifier or a single transistor.

Figure 3.22. A high-accuracy noise figure measurements using the PNA-X series network analyser [55].

Garelli, Ferrero and Bonino (2009) present a noise and scattering parameters test set using a vector network analyser (VNA), a noise figure analyser (NFA), a noise source, microwave couplers, microwave switches and a microwave tuner. This test set can measure S-parameters and noise waves and these measurements can be transformed via a matrix transformation to extract the noise parameters [56].

The measurement method based on noise wave formalism has been shown to be viable in the literature, but no evidence was found of this methods' widespread use in ultra-low noise cryogenic LNA measurements. Uncertainty values from institutions using this method were not available for comparison with the other methods reviewed [43].

3.8 The cold attenuator measurement method

This method was first developed and used by Weinreb and Kerr and the National Radio Astronomy Observatory (NRAO) [41].

The cold attenuator measurement method addresses most of the issues with the classic Y-factor method. This method uses a cryogenically cooled attenuator that is coupled directly to the input port of the amplifier under test (AUT). Figure 3.23 shows a diagram of the test method. The attenuator is cooled by the same cold plate as the AUT. When the noise diode is unbiased, the attenuator behaves like the cold load. When the noise diode is biased, the noise temperature it produces is reduced by the insertion loss of the attenuator to a level suitable for testing extremely low noise cryogenic LNAs. The loss between the noise source and the AUT as well as the noise contribution of the other elements in the cascade are factors that influence the accuracy of the final equivalent noise temperature value [57].

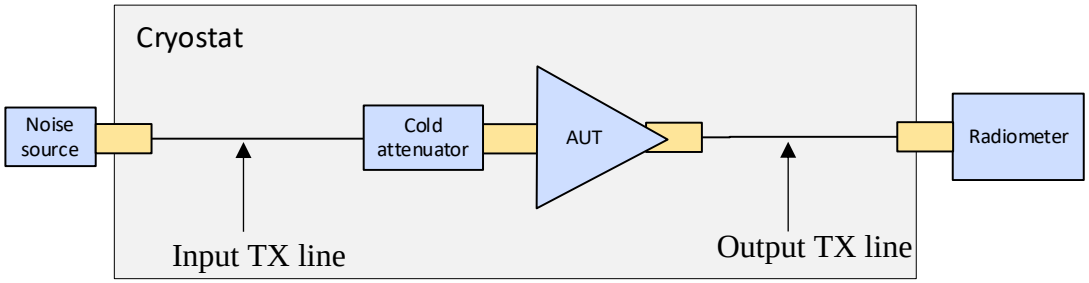

Figure 3.23. The cold attenuator measurement method [58].

A noise diode is connected via a vacuum feedthrough and low loss transmission (TX) line to the attenuator. When the noise diode is switched on, the noise temperature delivered to the AUT is dominated by the hot noise temperature (T_h) from the noise diode attenuated by the input TX line and the attenuator. When the noise diode is switched off, the noise temperature delivered

to the AUT is dominated by the equivalent noise temperature of the attenuator ($T_{e\,ATT}$) with a small contribution from the noise diode T_c and the input TX line [58].

3.8.1 Transmission line property extraction

Low loss coaxial TX lines are used to connect the ambient temperature vacuum feedthrough adaptors to the AUT. These TX lines have large temperature gradients across them and their noise temperature T_n and G_i (<1) need to be determined.

For the first measurement, TX line 1 and TX line 2 are connected in series using a low loss short jumper cable. Referring to Figure 3.24, the TX lines are thermally anchored to the cold plate at planes 2 and 3 and thermally anchored to the ambient temperature feedthrough adaptors at planes 1 and 4. The system is cooled and a two-port S-parameter measurement is carried out. The TX lines are created with identical characteristics in order for the assumption expressed by the equation $G_{i\,TX\,line1} = \sqrt{G_{\mathrm{i}\,TX\,line1} G_{\mathrm{i}\,TX\,line2}}$ to be valid [41]. Two methods are shown for measuring $G_{\mathrm{i}\,TX\,line1} G_{\mathrm{i}\,TX\,line2}$ in Figure 3.24 and Figure 3.25.

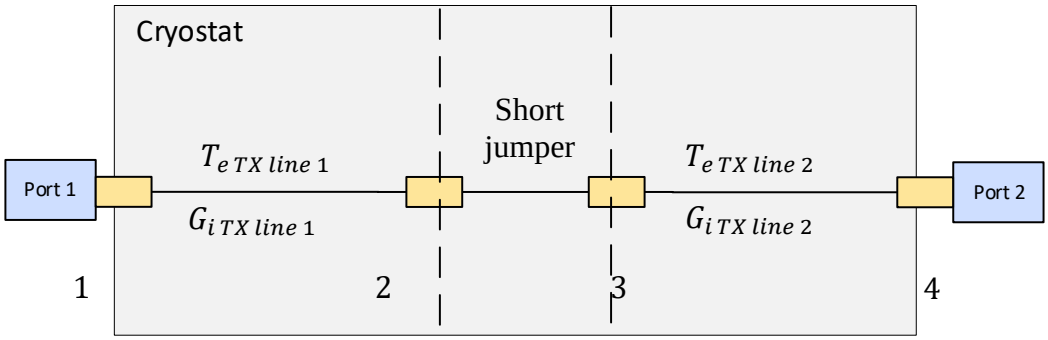

Figure 3.24. Measurement of $G_{i\,TX\,line\,1} G_{i\,TX\,line\,2}$ using a VNA [41].

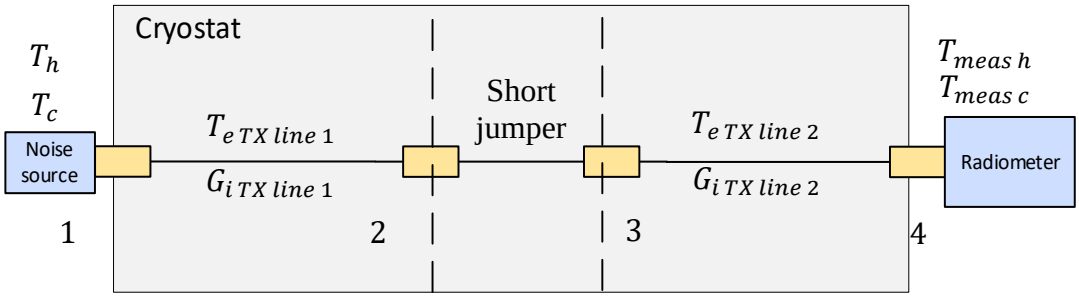

Figure 3.25. Measurement of $G_{i\,TX\,line\,1} G_{i\,TX\,line\,2}$ using the classic Y-factor method [23][48][49].

The total loss through the TX lines is determined through a Y-factor measurement and a modified form of equation (3.5) [49].

$$G_{i\,TX\ line\ 1}G_{i\,TX\ line\ 2} = \frac{T_{meas\ h} - T_{meas\ c}}{T_h - T_c} \tag{3.20}$$

The $T_{e\,TX\ line\ 1}$ can be estimated by the assumption shown in the following equation [58]:

$$T_{phys\,TX\ line\ 1} = \frac{T_{amb} + T_{phys\ ATT}}{2} \tag{3.21}$$

Where:

- T_{amb} is the physical temperature of the vacuum feedthrough in K.
- $T_{phys\ ATT}$ is the physical temperature of the attenuator in K.

3.8.2 The attenuator property extraction

The second measurement determines the attenuator insertion gain (G_i) when cooled to operating temperature. The S-parameter measurement is carried out with the TX lines and attenuator in place. The same low loss short jumper cable is used [41].

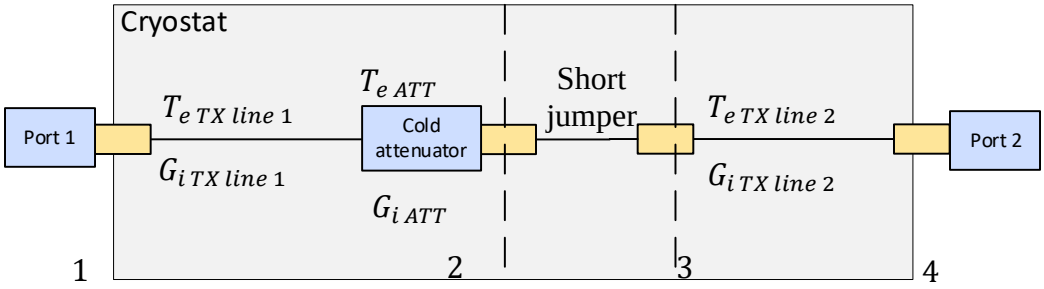

Figure 3.26. The S-parameter measurement of the TX lines and attenuator [41].

Once the test system calibration is complete, the cryogenic LNA can be measured in the next step.

3.8.3 Amplifier under test measurement

For the third measurement, available gain (G_a) is calculated for elements between the noise source and the AUT using the S-parameter data captured by the previous measurements.

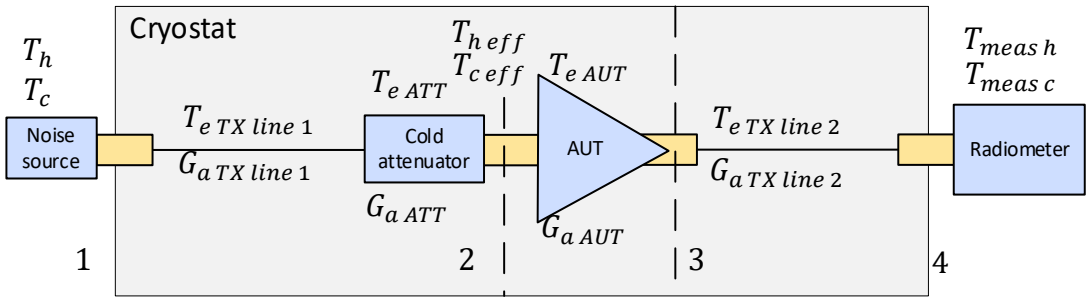

Figure 3.27. The cold attenuator measurement with the AUT and all elements connected [58][41].

The effective noise power $T_{h\,eff}$, $T_{c\,eff}$ delivered to the AUT is calculated. The simplified equation (neglecting the input TX line contribution) is as follows [41][58][59][60]:

$$T_{h\,eff} = \frac{T_h}{L_{ATT}} + T_{phys\,ATT}\left(1 - \frac{1}{L_{ATT}}\right) = T_h G_{a\,ATT} + T_{phys\,ATT}(1 - G_{a\,ATT}) \quad (3.22)$$

$$T_{c\,eff} = \frac{T_c}{L_{ATT}} + T_{phys\,ATT}\left(1 - \frac{1}{L_{ATT}}\right) = T_c G_{a\,ATT} + T_{phys\,ATT}(1 - G_{a\,ATT}) \quad (3.23)$$

The cascaded equivalent noise temperature $T_{e\,cas}$ can be calculated from the effective noise temperatures using the customised Y-factor equation:

$$T_{e\,cas} = \frac{T_{h\,eff} - YT_{c\,eff}}{Y - 1} \quad (3.24)$$

$$Y = \frac{T_{meas\,hot}}{T_{meas\,cold}} \quad (3.25)$$

Where (in reference to equations (3.22), (3.23), (3.24) and (3.25)):

- $T_{h\,eff}$ is the effective noise temperature at the input of the AUT when the noise diode is on in K.
- $T_{c\,eff}$ is the effective noise temperature at the input of the AUT when the noise diode is off in K.

- T_h is the noise temperature at the output port of the noise diode when the noise diode is on in K.
- T_c is the noise temperature at the output port of the noise diode when the noise diode is off in K.
- $T_{phys\ ATT}$ is the physical temperature of the attenuator in K.
- $G_{a\ ATT}$ is the available gain of the attenuator in W/W (<1).
- L_{ATT} is the loss of the attenuator in W/W (>1)
- $T_{e\ cas}$ is the combined equivalent noise temperature of the AUT, the output TX line, the pre-amplifier and the radiometer in K.
- $T_{meas\ hot}$ is the measured noise temperature when the noise diode is on in K.
- $T_{meas\ cold}$ is the measured noise temperature when the noise diode is off in K.

In the case of equation (3.22), the $T_{h\ eff}$ value will be dominated by the attenuated noise diode hot noise temperature (T_h). Equation (3.23) shows that the $T_{c\ eff}$ will be dominated by the physical temperature of the attenuator ($T_{phys\ ATT}$) with a small contribution from the unbiased noise diode which is a thermal source at room temperature.

Equation (3.22) and (3.23) can be expanded further to include the input TX line contribution [61]:

$$T_{h\ eff} = (T_h + T_{e\ TX\ line\ 1})G_{a\ TX\ line\ 1}G_{a\ ATT} + T_{phys\ ATT}(1 - G_{a\ ATT}) \quad (3.26)$$

$$T_{c\ eff} = (T_c + T_{e\ TX\ line\ 1})G_{a\ TX\ line\ 1}G_{a\ ATT} + T_{phys\ ATT}(1 - G_{a\ ATT}) \quad (3.27)$$

Where:

- $T_{h\ eff}$ is the effective noise temperature at the input of the AUT when the noise diode is on in K.
- $T_{c\ eff}$ is the effective noise temperature at the input of the AUT when the noise diode is off in K.
- T_h is the noise temperature at the output port of the noise diode when the noise diode is on in K.

- T_c is the noise temperature at the output port of the noise diode when the noise diode is off in K.
- $T_{e\ TX\ line\ 1}$ is the equivalent noise temperature of TX line 1 in K.
- $G_{a\ TX\ line\ 1}$ is the available gain of the input TX line in W/W (<1).
- $T_{phys\ ATT}$ is the physical temperature of the attenuator in K.
- $G_{a\ ATT}$ is the available gain of the attenuator in W/W (<1).

The 2nd stage contribution can be removed from T_{cas} using formula (3.10).

The benefits of the cold attenuator measurement method include the following [41][62]:

- Measurement speed is quick due to no physical changing of the measurement system required [41].
- The uncertainty due to the mismatch between the AUT and the noise source is drastically lowered by the isolation provided by the attenuator. This isolation also lowers the error caused by the impedance change between the on and the off states of the noise diode [41].
- The uncertainty of the $G_{TX\ Line\ 1}$ (<1) is much less significant when cascaded with an attenuator with a $G_{i\ ATT}$ = -20 dB [41].
- This method is able to take advantage of the following existing features of a commercial noise figure analyser:
    - Issuing commands and reading from the analyser using a computer.
    - Input loss compensation value and temperature.
    - Output loss compensation value and temperature.
    - Calibration to determine the noise contribution of the noise figure analyser.
    - Uploading the noise source ENR values.

The disadvantages of the cold attenuator measurement method:

- This method needs careful calibration of the noise source, the TX lines and the attenuator.
- Any uncertainty of the physical temperature of the attenuation element in the attenuator ($\Delta T_{phys\ ATT}$) due to thermal gradient or poor thermal conductivity has a significant effect on the uncertainty of the equivalent noise temperature of the AUT ($\Delta T_{e\ AUT}$).

3.9 The measurement uncertainty comparison

There are several factors that contribute to the amplifier under test noise temperature measurement uncertainty ($\Delta T_{e\ AUT}$) of the classic Y-factor method and the cold attenuator method [63]:

- The uncertainty of the ENR (ΔENR) of the noise source.
- The degree of the mismatch between the noise source and the AUT.
- The degree of the mismatch between the AUT and the radiometer.
- The equivalent noise temperature of the radiometer ($T_{e\ RAD}$) used for the measurement.
- The available gain of the AUT ($G_{a\ AUT}$).

This analysis will show that the measurement uncertainty of the equivalent noise temperature of the AUT ($\Delta T_{e\ AUT}$) due to the uncertainty of the ENR (ΔENR) alone is sufficient to recommend the cold attenuator method over the classic or corrected Y-factor measurement methods. The peak-to-peak calibration uncertainty of 0.1 dB to 0.25 dB for the ENR is expected from a commercial noise diode. The second stage contribution, the radiometer and the insertion loss uncertainties are neglected for this analysis. In this work the symbol delta (Δ) is used to denote uncertainty.

3.9.1 The measurement uncertainty of the classic Y-factor method

The equivalent noise temperature (T_e) determined by the classic Y-factor measurement method is given by equation (3.4) which is shown below for reference [43][64][65]:

$$T_e = \frac{T_h - YT_c}{Y - 1} \tag{3.28}$$

The uncertainty contribution for each of the terms in equation (3.28) is determined by taking the partial derivative for each term with respect to the equivalent noise temperature (T_e) and then multiplying the resultant equation by the term's uncertainty. This results in three separate equations[64][65]:

$$\left|\frac{\partial T_e}{\partial T_h}\right| \Delta T_h = \frac{\Delta T_h}{Y - 1} \tag{3.29}$$

$$\left|\frac{\partial T_e}{\partial T_c}\right| \Delta T_c = \frac{-\Delta T_c}{1 - 1/Y} \tag{3.30}$$

$$\left|\frac{\partial T_e}{\partial Y}\right| \Delta Y = \frac{T_c - T_h}{(Y-1)^2} \Delta Y \tag{3.31}$$

Where:

- ΔT_h is the T_h uncertainty resulting from the ΔENR in K.
- ΔT_c is the T_c uncertainty resulting from the noise source physical temperature uncertainty in K.
- ΔY is the Y-factor uncertainty resulting from both ΔT_h and ΔT_c. ΔY can be expressed by adapting equation (3.2) to form the equation [64][65]:

$$\Delta Y = \frac{T_e + (T_h + \Delta T_h)}{T_e + (T_c - \Delta T_c)} \tag{3.32}$$

Assuming the uncertainties of the individual terms are uncorrelated, the root square sum (RSS) method is used to calculate the worst case total uncertainty ΔT_e shown in the equation [63][64] [65]:

$$\Delta T_e = \sqrt{\left(\left|\frac{\partial T_e}{\partial T_h}\right| \Delta T_h\right)^2 + \left(\left|\frac{\partial T_e}{\partial T_c}\right| \Delta T_c\right)^2 + \left(\left|\frac{\partial T_e}{\partial Y}\right| \Delta Y\right)^2} \tag{3.33}$$

3.9.2 The measurement uncertainty of the cold attenuator method

The cold attenuator measurement method uses an adapted form of equation 3.28. The T_h and T_c are replaced by $T_{h\,eff}$ and $T_{c\,eff}$ resulting in the equation [43]:

$$T_e = \frac{T_{h\,eff} - Y T_{c\,eff}}{Y - 1} \tag{3.34}$$

Equations (3.22) and (3.23) for $T_{h\,eff}$ and $T_{c\,eff}$ are shown for reference:

$$T_{h\,eff} = T_h G_{a\,ATT} + T_{phys\,ATT}(1 - G_{a\,ATT}) \tag{3.35}$$

$$T_{c\,eff} = T_c G_{a\,ATT} + T_{phys\,ATT}(1 - G_{a\,ATT}) \tag{3.36}$$

The uncertainty contribution for each of the terms in equation (3.34) is determined by taking the partial derivative for each term with respect to the T_e and then multiplying the resultant equation by the term's uncertainty. This results in three separate equations [64][65]:

$$\left|\frac{\partial T_e}{\partial T_h}\right| \Delta T_{h\,eff} = \frac{\Delta T_{h\,eff}}{Y-1} \tag{3.37}$$

$$\left|\frac{\partial T_e}{\partial T_c}\right| \Delta T_{c\,eff} = \frac{-\Delta T_{c\,eff}}{1-1/Y} \tag{3.38}$$

$$\left|\frac{\partial T_e}{\partial Y}\right| \Delta \mathrm{Y} = \frac{\mathrm{T_{c\,eff}} - \mathrm{T_{h\,eff}}}{(Y-1)^2} \Delta \mathrm{Y} \tag{3.39}$$

Where:

- $\Delta T_{h\,eff}$ is the $T_{h\,eff}$ uncertainty resulting from the ΔENR in K.
- $\Delta \mathrm{T}_{c\,eff}$ is the $T_{c\,eff}$ uncertainty resulting from the noise source physical temperature uncertainty in K.
- ΔY is the Y-factor uncertainty resulting from both $\Delta T_{h\,eff}$ and $\Delta\, T_{c\,eff}$. ΔY can be expressed by adapting equation (3.2) to form the equation [43]:

$$\Delta Y = \frac{T_e + \left(T_{h\,eff} + \Delta T_{h\,eff}\right)}{T_e + \left(T_{c\,eff} - \Delta T_{c\,eff}\right)} \tag{3.40}$$

Assuming the uncertainties of the individual terms are uncorrelated, the root square sum (RSS) method is used to calculate the worst case total uncertainty ΔT_e shown in the equation [63][64] [65]:

$$\Delta T_e = \sqrt{\left(\left|\frac{\partial T_e}{\partial T_{h\,eff}}\right| \Delta T_{h\,eff}\right)^2 + \left(\left|\frac{\partial T_e}{\partial T_{c\,eff}}\right| \Delta T_{c\,eff}\right)^2 + \left(\left|\frac{\partial T_e}{\partial Y}\right| \Delta Y\right)^2} \tag{3.41}$$

The ΔENR effect on ΔT_e for the classic Y-factor and the cold attenuator measurement methods is represented on Figure 3.28. The following parameters were set for the calculation:

- The ENR values used are 5 dB to 30 dB in 5 dB steps. The ΔENR set to 0.1 dB for all ENR values.
- An attenuator with a G_a = -20 dB at a $T_{phys\ ATT}$ = 15 K with a $\Delta T_{phys\ ATT}$ = 0.5 K.
- The noise diode ambient temperature (T_o) = 290 K.
- The $T_{e\ AUT}$ = 3 K.

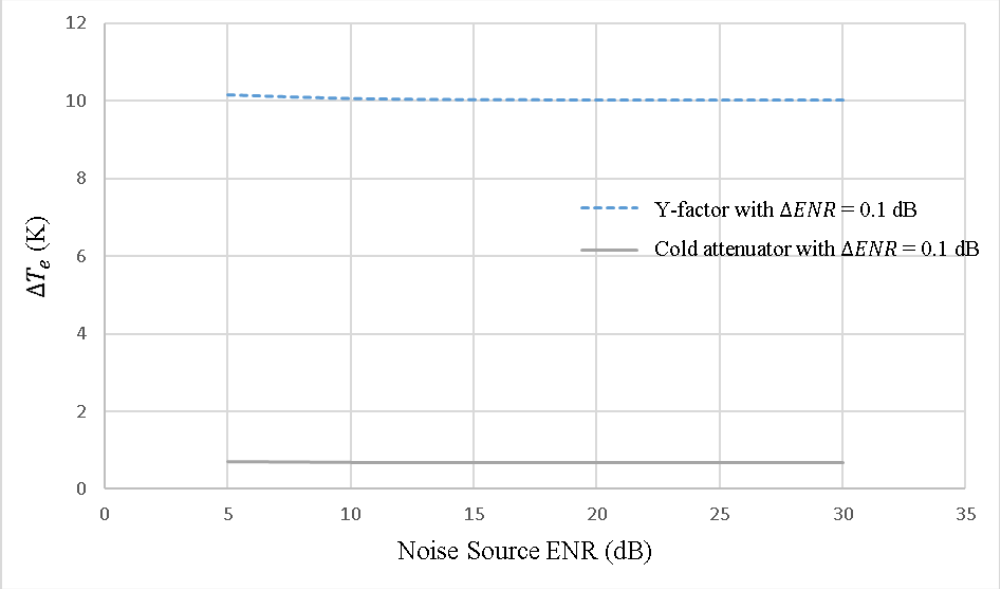

Figure 3.28. The effect of ΔENR on the cold attenuator method and classic Y-factor method.

3.10 Summary

Further consideration is not given to the classic and corrected Y-factor methods as the uncertainty is unacceptably high. The VNA based noise-wave measurement method is excluded as it requires access to a VNA with built-in noise receiver. The two most viable measurement methods are compared in Table 3.2.

Table 3.2. Comparison of viable measurement methods.

	Method	
	Cold source	**Cold attenuator**
Uncertainty	Lowest uncertainty	Acceptable for cryogenic LNA
Equipment	NFA or radiometer Isothermal attenuator Noise source	NFA or radiometer Isothermal attenuator VNA Noise source
Speed of measurement	Slow Requires three cool-down cycles per AUT tested	Quick After calibration only requires one cooldown per AUT tested
Complexity of measurement	Medium complexity	Low complexity

The cold attenuator method is selected as the preferred cryogenic LNA T_e measurement method. Comparable hardware is used for the cold source measurement method, thus cold source measurements are not excluded in possible future testing.

Furthermore, Table 3.3 shows examples of the cold attenuator measurement method used by multiple institutions specifically testing LNAs intended for radio astronomy use. The test equipment used is similar to that available during this investigation.

Table 3.3. Reported cold attenuator measurement by various institutions.

Source	Institution	f (GHz)	Gain (dB)	T_{phys} (K)	T_e (K)	ΔT_e (K)	$G_{i\ ATT}$ (dB)	Equipment used
Liu and Weinreb (2017) [66]	National Sun Yat-sen University	3.5	N/A[7]	24	0.55	N/S[8]	-20	N8975A
Montazeri and Bardin (2018) [67]	University of Massachusetts	2-4	28	16.5	3.3-4	N/S	N/S	N/S
Russel and Weinreb (2012) [68]	California Institute of Technology	1-6	N/S	4.2	5 - 15	±1	-20	N/S
Akgiray *et al.* (2013) [69]	California Institute of Technology	0.7 - 16	38	21	< 10	N/S	N/S	N/S
		2 - 18	20-26	22	< 10	± 1	N/S	N/S
		6 – 40	26	20	≤ 20	± 2	N/S	N/S
Cano and Artel (2009) [70]	University of Cantabria	6-18	30	18	8	± 2	-20	346C N8975A
Fernandez (1998) [41]	Jet Propulsion Labs	2-2.6	N/S	15	2 – 6.5	±1.34	-20	HP 8970B 346A
Jiang *et al.* (2018) [71]	NRC Herzberg	0.9 -1.67	41.6	15	2	N/S	N/S	N/S
Weinreb, Bardin and Mani (2007) [72]	California Institute of Technology	1 – 3	28	15	2	±1	-20	N4002A N8975A
Cano Wadefalk and Gallego-Puyal (2010) [73]	University of Cantabria	4-12	N/S	N/S	7	1.7	-20	346CK01
Schleeh *et al.* (2016) [51]	Low Noise Factory	0.35-1.05	50	300[9]	10	0.05 dB[10]	-20	N/S
Fernández (2002) [74]	Centro Astronómico de Yebes	4-8	25.8	14	4	±1	-15	346 A, 346 C HP 8970 B DC block

The comparisons in this chapter resulted in a high level of confidence in the preferred measurement method. The next chapter expands on the selected method to show the implementation of the proposed solution.

[7] Liu and Weinreb (2017) was a filter measured using the cold attenuator method.

[8] Not specified (N/S).

[9] This measurement was carried out on an AUT that operates at room temperature.

[10] The uncertainty was given in dB.

Chapter 4

Proposed solution and implementation

In the previous chapter, the cold attenuator measurement method was selected as the most suitable option. In this chapter, the major system components are discussed, and the proposed measurement solution is presented.

At the end of this chapter, the reader should have a good understanding of the measurement hardware and steps.

The following system components are discussed:

- The cryogenic system
- Input and output transmission line
- Choice of broadband noise source
- The cold attenuator
- The cryogenic temperature sensor
- The radiometer

Finally, a summary of the major components and the measurement procedure is presented.

4.1 The cryogenic system

The LNA and attenuator need to operate at a physical temperature of 18 K. In the MeerKAT receiver the cooling power is provided by the Oxford Cryosystems Coldstar 2/9. This is a two-stage Gifford McMahon refrigeration cycle cryocooler. It can deliver 9 W of cooling power to the 18 K cooler second stage and 9 W of cooling power to the 77 K cooler first stage. This is a closed cycle cooling system with the helium compressor providing the high-pressure helium supply and accepting the low-pressure helium return. The cryocooler system is shown in Figure 4.1 [75].

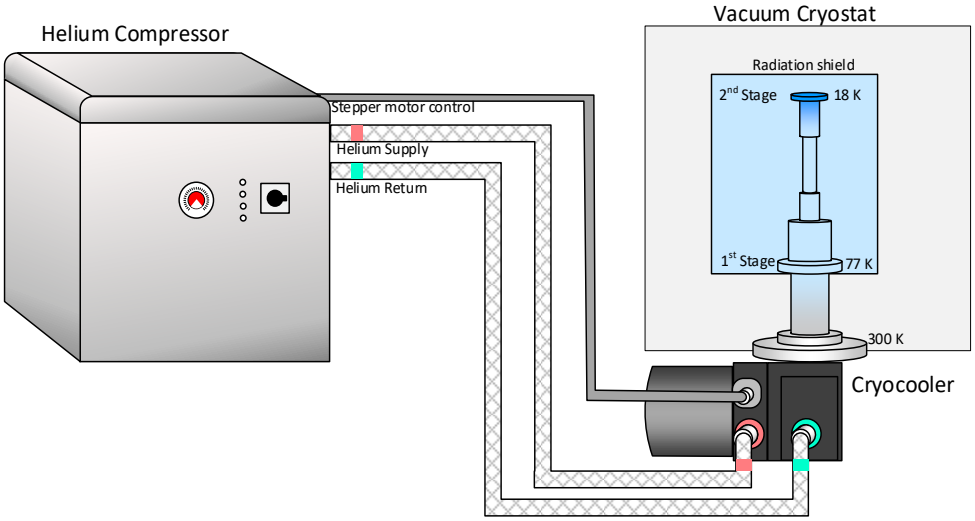

Figure 4.1. The Oxford Cryosystems Coldstar 2/9 cold head attached to the K450 helium compressor.

The two greatest heat loads on the cold head are the conduction and convection through the air. By installing the cold head inside a vacuum cryostat and pumping the system down to a high vacuum, the conduction and convection effects are mitigated. However, radiation heat transfer becomes more efficient in a high vacuum. Radiation heat transfer is highly dependent on the temperature difference between the two surfaces, thus a radiation shield thermally connected to stage 1 of the cryocooler greatly reduces the thermal load on stage 2 of the cryocooler. [76]

Additional heat loads on the cold head are the thermal conduction of the input and output transmission lines, the thermal conduction of the LNA bias harnesses, the radiation load and the dissipation of the amplifier under test.

4.2 Input and output transmission line

The input and output transmission (TX) lines are the coaxial cables that carry the signals from the noise diode to the attenuator and from the amplifier under test (AUT) to the noise figure analyser (NFA). Shown in Figure 4.2, the TX lines have a temperature gradient of approximately 280 K across each, with the cold side attached to a component on the 18 K cold plate and the hot side attached to the vacuum cryostat outer wall at 300 K.

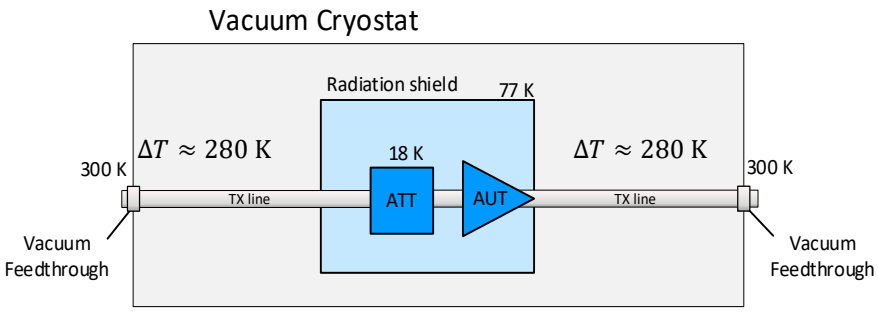

Figure 4.2. The temperature gradient across the input and output TX lines.

The input and output transmission lines need to be able to survive repeated heating and cooling cycles without performance degradation. The thermal conductivity of the cable should be low enough to not cause excessive heat loading of stage 2 of the cryocooler, whilst also having low insertion loss to radio frequency signals. The Times Microwave 0.090-inch outer diameter coaxial cable with high purity silicone dioxide (Si02) dielectric addresses these issues. The SiO2 dielectric is unaffected by thermal cycling. The thermal conductivity is reduced by making the outer shield stainless steel with a thinner outer copper conductor. The centre conductor is copper. The cable is shown in Figure 4.3 with the welded hermetic N-type vacuum feedthrough connector [77].

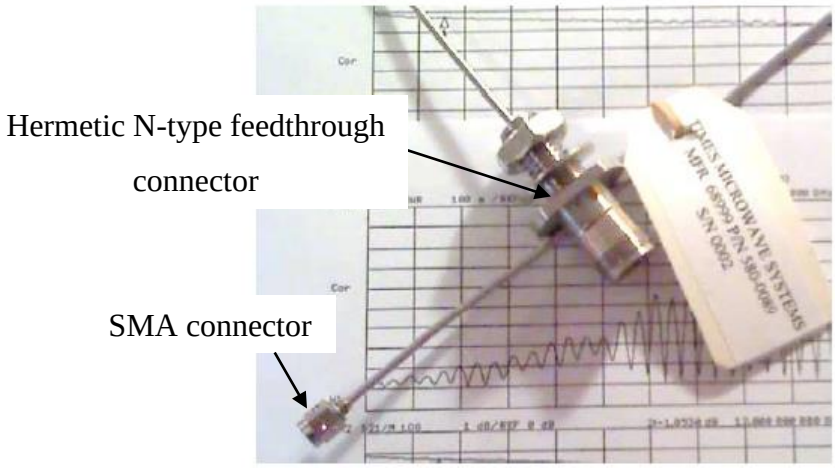

Figure 4.3. The vacuum feedthrough connector [78].

4.3 Choice of broadband noise source

The hot noise temperature (T_h) and cold noise temperature (T_c) are provided by a broadband active noise source. Figure 4.4 highlights the location of the noise source. The cold attenuator is a type of passive noise source that is examined in the following section.

In this section, the excess noise ratio (ENR) is defined and the equation for determining it is given. A method for determining the optimum value of ENR is shown.

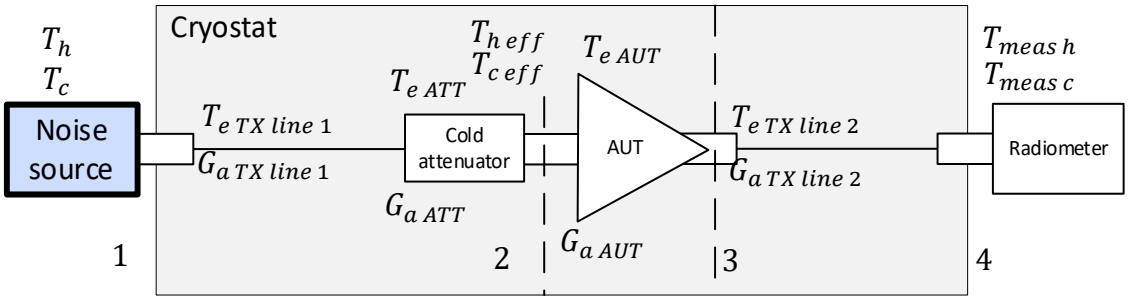

Figure 4.4. The cold attenuator measurement method with the noise source highlighted.

4.3.1 Excess noise ratio of an active noise source

Using a noise source based on an active device such as a diode, transistor, or tube has the benefit that it is able to generate two different noise temperatures. The most popular active noise source shown in Figure 4.5 uses a purpose-built diode producing T_h when reverse biased into avalanche breakdown. Shown in Figure 4.6 is the thermal noise T_c produced by the attenuator when the diode is unbiased. A disadvantage is that the active device characteristics drift over time hence the noise source requires regular calibration. An advantage of this type of source is that no external radio frequency switches are needed to switch between T_h and T_c [5][21].

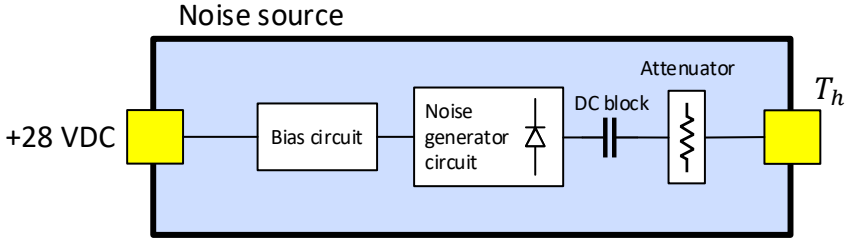

Figure 4.5. The noise source has been switched on and the diode-based noise generation circuit produces a noise temperature of T_h at the output terminal [27].

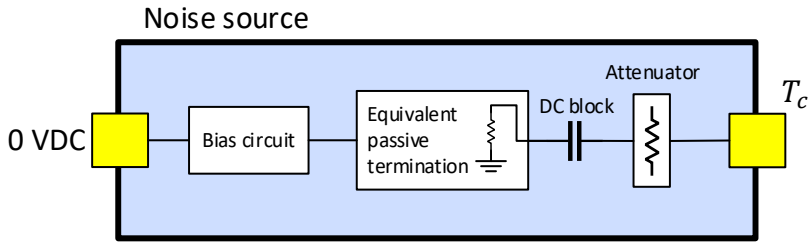

Figure 4.6. The noise source has been switched off and the noise generation circuit has been replaced with an equivalent passive termination producing a noise temperature of T_c at the output terminal [27].

T_h is the noise temperature available at the output port when the active device is biased in the avalanche breakdown region. T_h is much greater than the thermal noise and may be represented by the excess noise ratio (ENR), which is defined as the difference between the noise generated by the source biased in avalanche breakdown and the noise generated by a passive termination at physical temperature T_c. The ENR of a noise source is given by the equations [21]:

$$ENR = 10log\frac{T_h - T_c}{T_c} \tag{4.1}$$

$$T_h = T_c\left(1 + 10^{\frac{ENR}{10}}\right) \tag{4.2}$$

Where:

- ENR is the excess noise ratio of the noise source in dB.
- T_h is the noise temperature at the output port when the source is biased in avalanche breakdown in K.
- T_c is the noise temperature at the output port when the source is unbiased and represented as a thermal source in K.

Assuming a T_c of 295 K, the T_h for a 5.5 dB ENR noise source is approximately 1341 K and the T_h for a 15 dB ENR noise source is approximately 9623 K.

In the measurement steps, the case temperature of the noise source is measured using a thermocouple and this value is used as T_c. Table 4.1 shows the specifications of the two noise sources that were available during the measurement.

Table 4.1. Noise sources available during measurements.

Model	Uncertainty at 1 GHz	ENR at 1 GHz
N4000A	0.091 dB	5.559 dB
346 B	0.2 dB	14.99 dB

4.3.2 Choosing the optimum ENR value and attenuator value

Cano, Wadefalk and Gallego-Puyol (2010) suggest that the measurement uncertainty due to fluctuations in the power measured by a radiometer can be determined by the equation [73]:

$$\Delta T_{e\,AUT} = \sqrt{\frac{2}{BW \cdot \tau}} \cdot \frac{\left(T_{h\,eff} + T_{e\,AUT}\right)\left(T_{c\,eff} + T_{e\,AUT}\right)}{\left(T_{h\,eff} - T_{c\,eff}\right)} \tag{4.3}$$

$$T_{h\,eff} = T_h \cdot G_{a\,ATT} + T_{phys\,ATT}(1 - G_{a\,ATT}) \tag{4.4}$$

$$T_{c\,eff} = T_c \cdot G_{a\,ATT} + T_{phys\,ATT}(1 - G_{a\,ATT}) \tag{4.5}$$

Where:

- $\Delta T_{e\,AUT}$ is the uncertainty of the equivalent noise temperature of the amplifier under test in this case only due to random fluctuations in the radiometer measured power in K.
- BW is the bandwidth of the pre-detection filter in Hz. This is the resolution bandwidth when using a noise figure analyser or a spectrum analyser.
- τ is the integration time per sample in s.
- $T_{h\,eff}$ is the effective noise temperature at the input of the AUT when the noise diode is on in K.
- $T_{c\,eff}$ is the effective noise temperature at the input of the AUT when the noise diode is off in K.
- T_h is the noise temperature at the output port of the noise diode when the noise diode is on in K.
- T_c is the noise temperature at the output port of the noise diode when the noise diode is off in K.
- $T_{phys\,ATT}$ is the physical temperature of the attenuator in K.

- $G_{a\ ATT}$ is the available gain of the attenuator in W/W (<1).

In the noise figure analyser, the number of sweep points determines how many samples of data are collected across the frequency band of interest. Each sweep point requires a certain amount of integration time for the measurement to settle before taking a measurement. The sweep time is the time taken to complete a measurement at all sweep points in the set band of interest. The integration time per sample can be calculated by dividing the sweep time by the number of points according to the equation [73]:

$$\tau = \frac{sweep\ time}{number\ of\ sweep\ points} = \frac{12}{128} = 0.09\ s. \tag{4.6}$$

Shown in Figure 4.7 are plots showing the attenuation of the attenuator versus the equivalent noise temperature uncertainty (ΔT_e) for two different ENR values. The orange plot is for the 5.5 dB ENR noise source and the blue plot is for the 15 dB ENR noise source. The values were determined for each datapoint using equation (4.3), with the following values used in the calculation:

- $T_c = 295$ K,
- $T_{e\ AUT} = 2\ K$,
- $T_{phys\ ATT} = 18$ K,
- Resolution bandwidth (RBW) = 4 MHz.

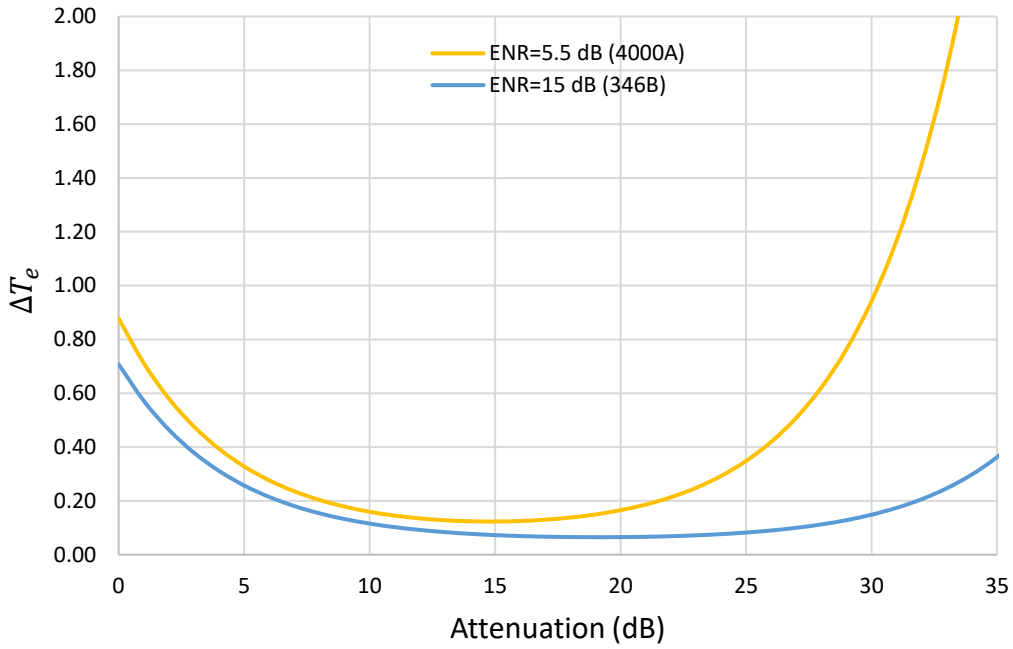

Figure 4.7. Attenuation of the attenuator versus equivalent noise temperature uncertainty for two different ENR value noise sources.

It can be seen from Figure 4.7 that the optimum attenuator insertion loss for the 15 dB ENR noise source is 20 dB. The optimum attenuator insertion loss for the 5.5 dB ENR noise source is between 15 dB. It can also be seen that the higher ENR noise source is preferable as it results in the lowest uncertainty.

4.3.3 Noise diode reflection coefficient

One other factor to consider when selecting the noise source is the return loss and the change in reflection coefficient between the on and the off state.

Figure 4.8 shows the measured reflection coefficient across the band for the 346B noise source. The effect of the difference between the on and off values is shown in determination of $G_{a\ ATT}$ in section 5.1.3. Figure 4.9 shows that the measured $|S_{11}|$ across the band for the N4000A noise source is greater than 35 dB.

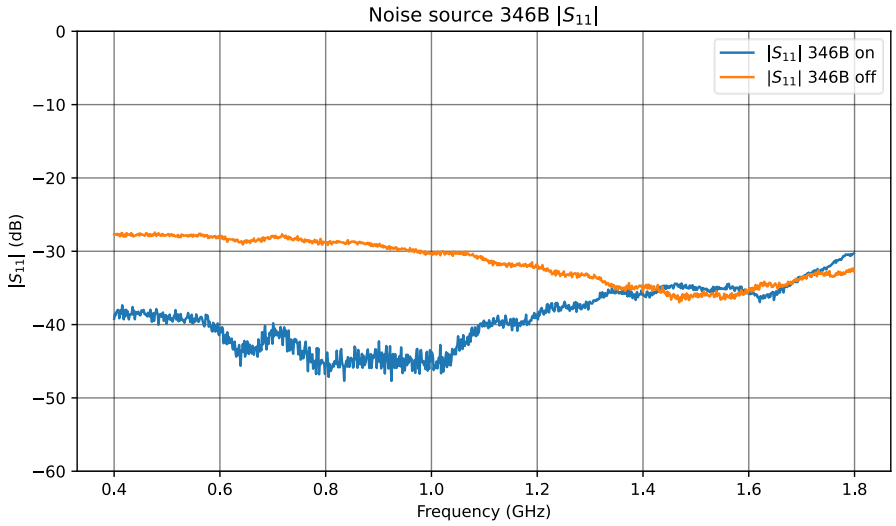

Figure 4.8. The 346B noise source measured $|S_{11}|$ values.

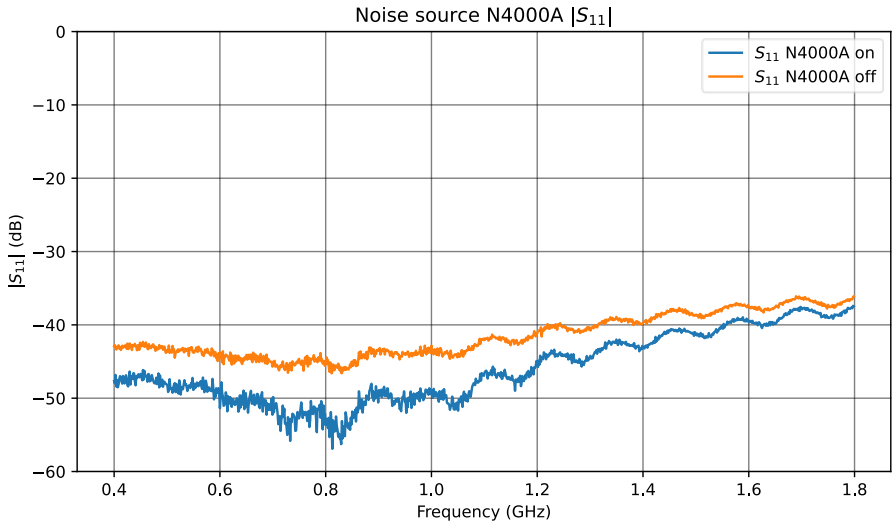

Figure 4.9. The N4000A noise source measured $|S_{11}|$ values.

The effect of the change of reflection coefficient in the 346B between the on and off state can be seen in the slightly different values for available gain of the feed cable and attenuator between the on and off state of the noise source as shown in the plot Figure 5.8. This effect is insignificant for the N4000A. Selecting the 346B in this instance adds slightly to calculation complexity in compensating for the slight difference in available gain in the on and off states. This error is offset by using available gain in the calculation. The 346B is selected due to the lower uncertainty when using the 20 dB attenuator as shown in the plots in Figure 4.7. The uncertainty added by a lower ENR noise source cannot be offset through calculation.

4.4 Cold attenuator

The most basic noise source is a passive termination (PT) held at a stable physical temperature other than room temperature. This passive termination produces broadband noise that is equal to $kTBW$. This type of noise source is known as a thermal noise source. Figure 4.10 shows a commercial thermal noise source that consists of a passive termination cooled using liquid nitrogen (LN_2). Figure 4.11 shows a simplified block diagram representation of a thermal noise source [21][22][79].

Figure 4.10. Model MT7025J99 cryogenic noise termination and controller [79].

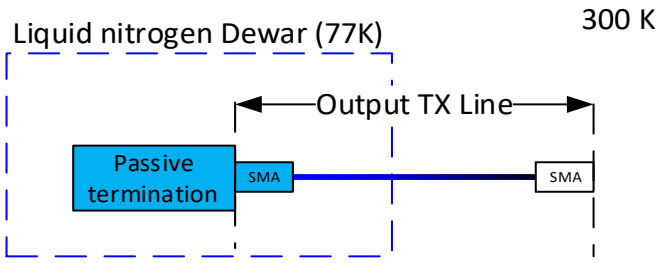

Figure 4.11. Simplified block diagram of an LN_2 thermal noise standard.

The benefit of a thermal noise source is that the accuracy of the noise generated by the passive termination can be determined to a high level of accuracy if the physical temperature is known. The disadvantage is that the output transmission line transitions from the cold temperature to ambient temperature. An intricate calculation of the transmission line insertion loss and noise temperature is required to add to the passive termination to produce the final noise temperature at the output port [22].

4.4.1 The cold attenuator as a thermal noise source

The cold attenuator method uses the attenuator as a thermal noise source coupled directly to the AUT. Referring to Figure 4.12, both the attenuator and the AUT are at the same physical temperature and the compensation for the output transmission line is not an issue. The accuracy of the noise source effective temperature calculation is determined by the accuracy of the measurement of the physical temperature of the attenuation element in the attenuator. The complexity with this measurement is in thermally isolating the centre conductor of the coaxial transmission line from the attenuation element within the attenuator. A higher temperature centre conductor may raise the physical temperature of the attenuation element in the attenuator resulting in the physical temperature measured on the case being different to the physical temperature of the attenuation element.

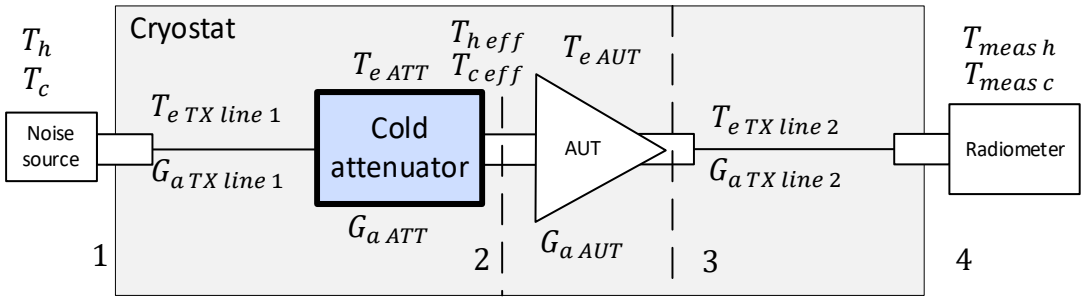

Figure 4.12. The cold attenuator measurement method with the attenuator highlighted [41].

Figure 4.13 shows the attenuator used by Akgiray *et al*. (2013) as an example. There is a coaxial in-line style attenuators that has been clamped into machined copper blocks that contact the attenuator body on all sides to give good thermal conductivity. The temperature sensor is attached as close as possible to the attenuator [68][69].

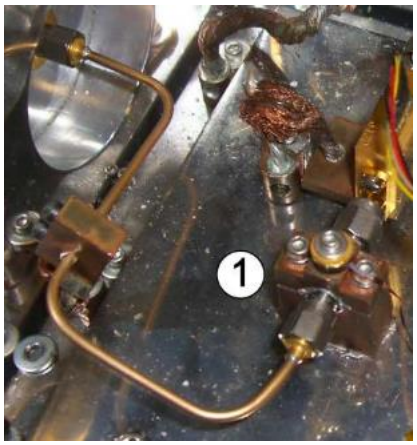

Figure 4.13. The attenuator used in Akgiray *et al*. (2013) [69].

4.4.2 The Quantum Microwave QMC-CRYOATT-20

Cano, Wadefalk and Gallego-Puyol (2010) designed and built a chip attenuator for the Yebes Observatory[11] using crystal quartz substrate for maximum thermal conductivity [73]. The Quantum Microwave thermalized cryogenic attenuator QMC-CRYOATT-20 is an off-the-shelf cryogenic attenuator that is designed with the same goal of maximum thermal conductivity. The substrate is crystal quartz, and this is bonded using silver epoxy to a machined gold-plated copper enclosure. The attenuator is shown in Figure 4.14 [80].

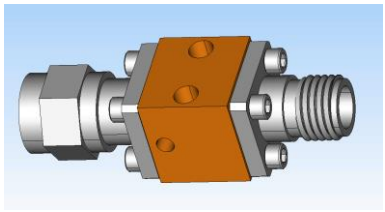

Figure 4.14. The Quantum Microwave cryogenic attenuator QMC-CRYOATT-20 [80].

A custom-milled copper block as used by Akgiray *et al*. (2013) as shown in Figure 4.13 is not required to fit around the attenuator as the QMC-CRYOATT-20 as shown in Figure 4.14 is able to be fastened directly to the cold plate. Additionally, the temperature sensor is able to be fixed directly to the attenuator case.

[11] Yebes Observatory or Centro Astronómico de Yebes (CAY) is an astronomical observatory located at Yebes, Castilla-La Mancha, Spain.

4.5 Cryogenic temperature sensor

The physical temperature of the cold attenuator needs to be known to a high degree of accuracy. Figure 4.15 and Figure 4.16 show two examples of the DT-670-CU temperature sensors from Lakeshore Cryotronics [62].

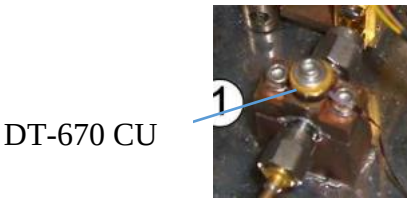

Figure 4.15. The DT-670-CU temperature sensor used in Akgiray *et al*. (2013) [69].

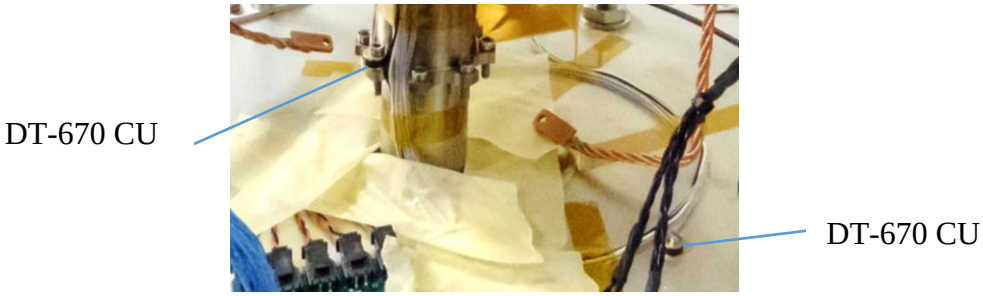

Figure 4.16. The DT-670-CU temperature sensors used in the MeerKAT receiver.

The DT-670B1-CU and DT-670-CU-1.4L are cryogenic temperature sensors manufactured by Lakeshore Cryotronics. The package for both sensors is the same and is shown in Figure 4.17. The sensor is mounted using a standard M3 fastener. The leads are 36 American wire gauge (AWG) phosphor bronze to minimise thermal loading. The leads are wound around and epoxied to the gold-plated copper bobbin that forms the outer package. This bobbin thermally anchors the leads and prevents them from influencing the temperature reading [81][82].

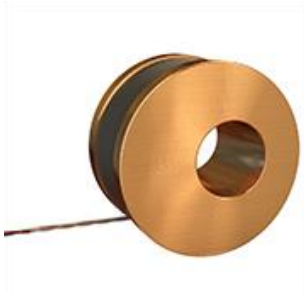

Figure 4.17. Lakeshore Cryotronics DT-670-CU silicon diode temperature sensor [82].

The DT-670B1-CU is the uncalibrated version of the sensor. It follows a standard curve with a tolerance of ± 0.5 K at a physical temperature of 18 K. This makes it suitable for general temperature sensing and control of the cold plate temperature controller.

The DT-670-CU-1.4L is calibrated between the physical temperatures 1.4 K to 325 K. This sensor is double the cost of the uncalibrated sensor. It has a calibrated accuracy of ± 0.012 K at 18 K and is used exclusively to measure the physical temperature of the cold attenuator [82].

The physical temperature of the attenuator ($T_{phys\ ATT}$) needs to be known to calculate both the effective hot and cold temperatures ($T_{h\ eff}$ and $T_{c\ eff}$) presented to the AUT. The plot in Figure 4.18 is generated using the equation (3.38), reproduced below:

$$\left|\frac{\partial T_e}{\partial T_c}\right| \Delta T_{c\ eff} = \frac{-\Delta T_{c\ eff}}{1 - 1/Y} \tag{4.7}$$

A cascaded calculation was set up to determine the resultant Y-factor value based on the worst case variation of the physical temperature of the attenuator due to the sensor uncertainty. This is shown in Appendix C - .. This Y-factor value was used with the uncertainty of the temperature sensor being directly responsible for the uncertainty of the effective cold temperature ($\Delta T_{c\ eff}$). The orange trace in Figure 4.18 is generated using the uncertainty of the uncalibrated temperature sensor and hence $\Delta T_{c\ eff}$ = 1 K peak to peak. The grey trace in Figure 4.18 is generated using the uncertainty of the calibrated temperature sensor and hence $\Delta T_{c\ eff}$ = 0.025 K peak to peak.

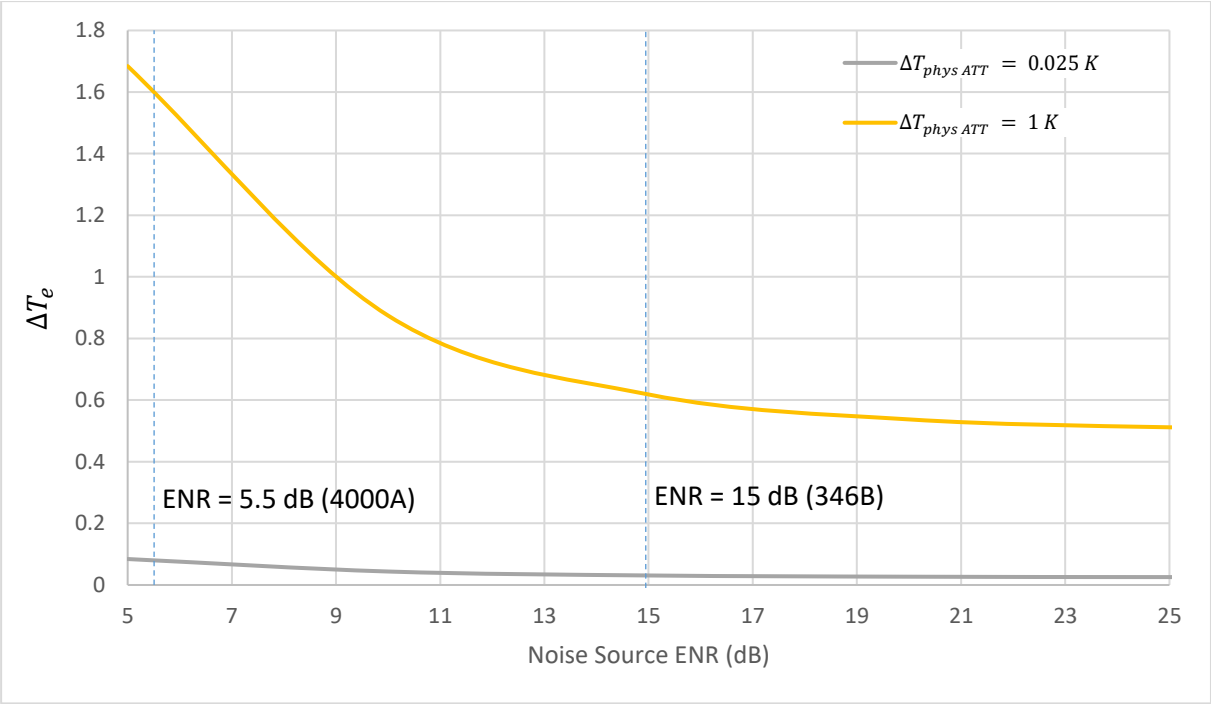

Figure 4.18. The effect of the physical temperature uncertainty of the cold attenuator ($\Delta T_{phys\ ATT}$) for different noise diode ENR values.

Figure 4.18 is a plot of the uncertainty resulting in the final $T_{e\ AUT}$ measurement due to the uncertainty of the calibrated and uncalibrated temperature sensors only. This shows the benefit of using the calibrated DT-670-CU-1.4L for the temperature measurement on the cryogenic attenuator.

4.6 Radiometer

As mentioned in section 2.2.3, a radiometer is a sensitive receiver designed to measure the noise power of radio and microwave radiation. In the cold attenuator measurement system it is responsible for measuring the noise power used for the Y-factor calculation.

Cano and Artel (2009) and Akgiray *et al*. (2013) both demonstrated the use of the Keysight N8975A noise figure analyser for cold attenuator noise temperature measurements [69][70].

The N8975A noise figure analyser was selected as the primary radiometer based on equipment utilized by labs in the literature as summarised in Table 3.3. The FSU 26 spectrum analyser was used as a secondary radiometer for verification.

4.6.1 Linearity

The values of T_h = 9623 K for a 15 dB ENR noise source were calculated using equation (2.9) and assuming T_c = 295 K. For a detailed calculation, refer to Appendix B.

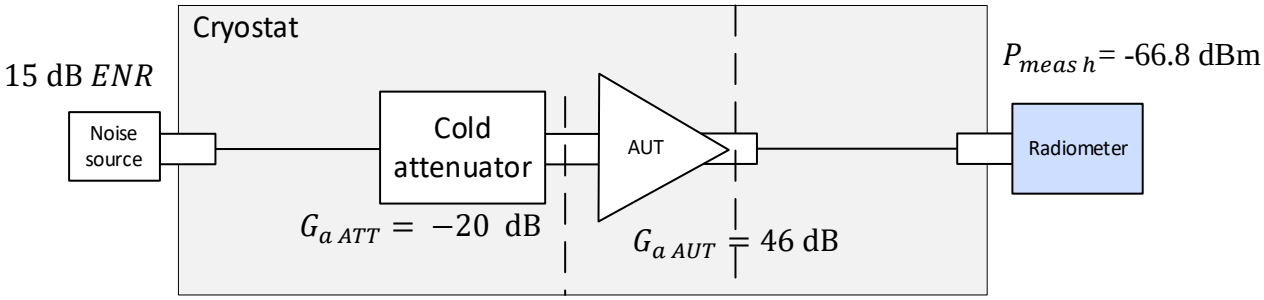

Figure 4.19. The cold attenuator measurement method with the radiometer highlighted showing the calculated $P_{meas\,h}$ using Appendix B [41].

Figure 4.19 shows the measurement system with approximately 26 dB total gain. Using a 15 dB ENR noise source results in a calculated final input power to the radiometer of -66 dBm. This is well within the -30 dBm that is recommended as the maximum power at 0 dB attenuation.

4.6.2 Radiometer input matching

An input attenuation of 20 dB selected on the noise figure analyser gives an input reflection coefficient of greater than 20 dB across the entire band as shown in Figure 4.20. This decreases the uncertainty caused by the mismatch between the AUT and the input to the noise figure analyser.

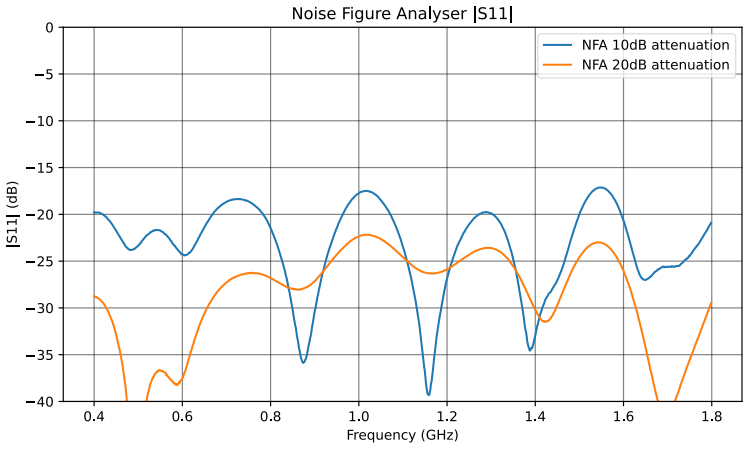

Figure 4.20. The measured $|S_{11}|$ for the N8975A noise figure analyser

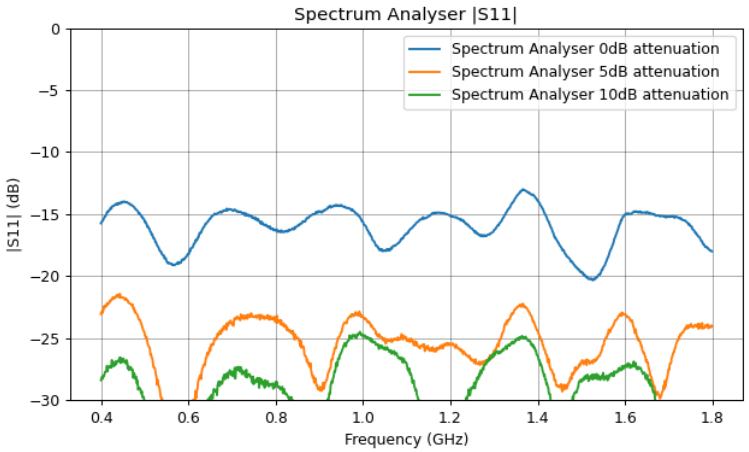

Figure 4.21. The measured $|S_{11}|$ of the FSU 26 spectrum analyser

The plot in Figure 4.21 shows the reflection coefficient for three attenuation levels of the FSU 26 spectrum analyser for comparison.

The noise figure analyser is to be used at 20 dB or more input attenuation and the spectrum analyser is to be used at 5 dB or more input attenuation to achieve greater than 20 dB return loss.

4.7 Conclusion

4.7.1 Major components

For the input and output transmission lines, the existing silicon dioxide (SiO_2) cable was available and was used. Figure 4.22 shows the two UT-085 semi rigid cable lengths that were built to bypass the existing second amplification stage.

Figure 4.22. The UT-085 jumper cables.

The Keysight 346B noise source was used and the Keysight N4000A noise source was used for secondary measurement. A thermocouple measures the noise source case temperature. The Quantum Microwave QMC-CRYOATT-20 thermalised cryogenic attenuator is used as the cold attenuator. The attenuation value was selected as 20 dB to be compatible with both noise sources. The Lakeshore DT-670-CU silicon diode cryogenic temperature sensor is used to measure the attenuator temperature. The Keysight N8975A noise figure analyser and a Rohde and Schwarz FSU 26 spectrum analyser are used as the radiometers. The data is captured and processed via a Python script.

This chapter has discussed the major components of the measurement system. Figure 4.23 shows a block diagram representation of this system.

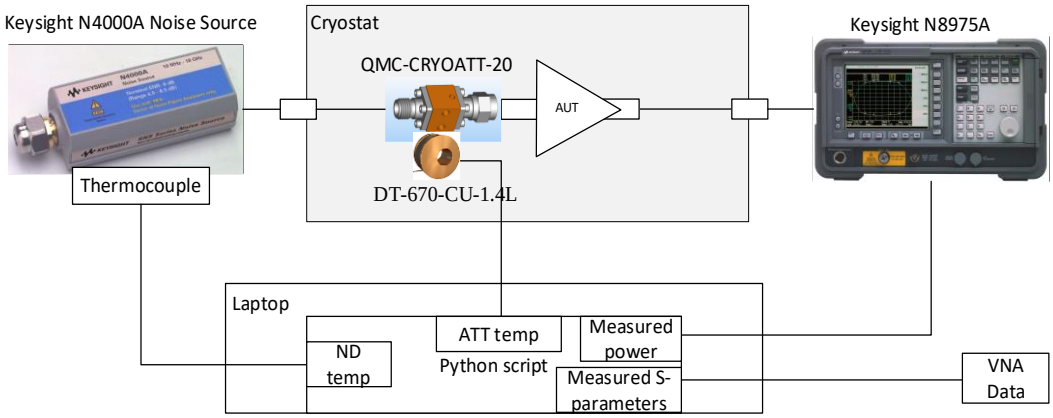

Figure 4.23. The cold attenuator measurement block diagram.

4.7.2 Measurement procedure overview

The measurement procedure is outlined here. The main purpose of steps one, two and three are to measure the values needed to solve the equations:

$$T_{h\,eff} = (T_h + T_{e\,TX\,line\,1})G_{a\,TX\,line\,1}G_{a\,ATT} + T_{phys\,ATT}(1 - G_{a\,ATT}) \tag{4.8}$$

$$T_{c\,eff} = (T_c + T_{e\,TX\,line\,1})G_{a\,TX\,line\,1}G_{a\,ATT} + T_{phys\,ATT}(1 - G_{a\,ATT}) \tag{4.9}$$

Step 1: The gain and noise temperature of the preamp and radiometer are measured using a standard Y-factor measurement and a vector network analyser. The $|S_{11}|$ values are measured between all components.

Step 2: The transmission lines are connected via a short jumper cable as per Figure 4.24 and the system is cooled to operating temperature. The insertion gain of the cascade ($G_{i\,TX\,line\,1}G_{i\,TX\,line\,2}$) is measurement using the VNA and the noise figure analyser. $G_{i\,TX\,line\,1}$ is estimated by calculating the square root of the cascaded measurement.

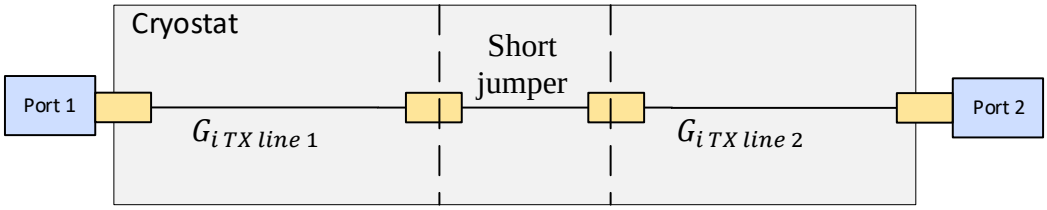

Figure 4.24. Measurement of $G_{i\,TX\,line\,1}G_{i\,TX\,line\,2}$ using a VNA [41].

The equivalent noise temperature of transmission line 1 ($T_{e\,TX\,line\,1}$) is estimated by equations:

$$T_{phys\,TX\,line\,1} = \frac{T_{amb+}T_{cold}}{2} \tag{4.10}$$

$$T_{e\,TX\,line\,1} = T_{phys\,TX\,line\,1}\left(\frac{1}{G_a} - 1\right) \tag{4.11}$$

Step 3: The attenuator is installed in-line as shown in Figure 4.25 and the system is cooled to operating temperature. The VNA measurement is carried out to measure the S-parameters of the cascaded network. The value for insertion gain of the attenuator ($G_{i\,ATT}$) is calculated based on the previous results.

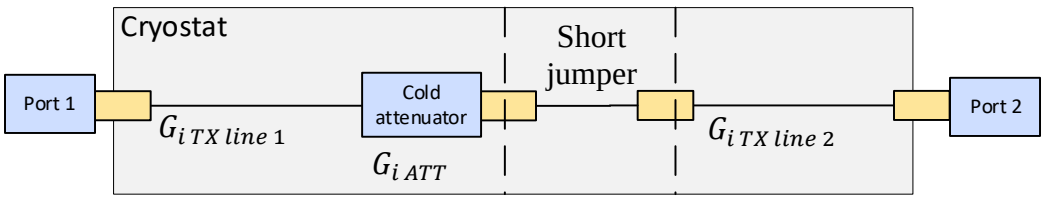

Figure 4.25. The S-parameter measurement of the TX lines and attenuator [41].

Step 4: The amplifier under test (AUT) is fitted as per Figure 4.26. In this last step, the $T_{meas\ hot}$ and $T_{meas\ cold}$ are measured and used to find the Y-factor value. The temperature sensor attached to the cold attenuator is recorded and used as the $T_{phys\ ATT}$. The temperature sensor attached to the noise source is recorded and used to calculate the T_h value for this measurement.

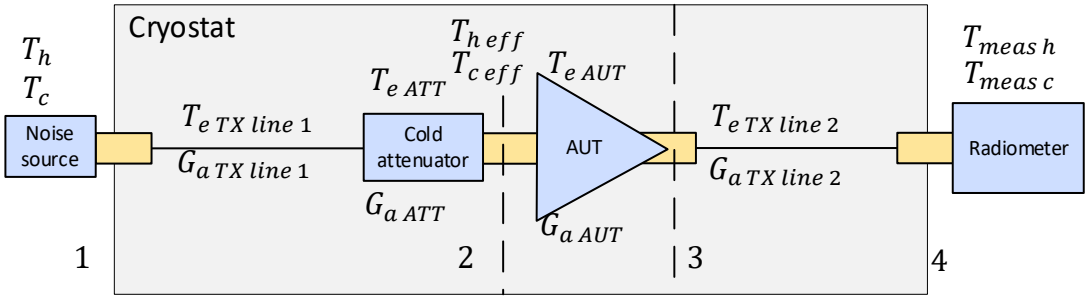

Figure 4.26. The cold attenuator measurement with the AUT and all elements connected.

Equations 4.12 and 4.13 can be used to calculate the cascaded equivalent noise temperature ($T_{e\ cas}$):

$$T_{e\ cas} = \frac{T_{h\ eff} - YT_{c\ eff}}{Y - 1} \tag{4.12}$$

$$Y = \frac{T_{meas\ hot}}{T_{meas\ cold}} \tag{4.13}$$

Once $T_{e\ cas}$ is calculated, equation 4.14 is used to remove the second stage effect of transmission line 2, test cable and the radiometer to determine $T_{e\ AUT}$.

$$T_{e\ AUT} = T_{e\ cas} - \frac{T_{e\ 2nd\ stage}}{G_{a\ AUT}} \tag{4.14}$$

The next chapter details how the practical measurements were carried out, the issues encountered, the improvements to the test method and the results obtained from the measurements.

Chapter 5

Measurement and results

To test the concepts discussed in Chapter 4, the testing was separated into three measurement campaigns:

- **Measurement campaign 1** was carried out in the lab in the SARAO office located at Black River Park using liquid nitrogen as the cryogen to cool the attenuator to 77 K. This allowed a demonstration test method to understand any issues with the setup before continuing to the next phase.

- **Measurement campaign 2** was carried out in Carnarvon at the Klerefontein receiver support base using a MeerKAT UHF-band receiver as the test cryostat. This was the first measurement carried out with the attenuator cooled to 18 K using the helium cooler. The goal of this measurement was to carry out the test, process the results and compare them with the supplier test. The main issue identified was the accurate determination of temperature of the attenuation element inside the attenuator.

- **A thermal study** was carried out to gain a deeper understanding of the heat distribution around the components on the cold plates. An improved configuration was implemented that anchored the transmission cable to the cold plate before connection to the attenuator.

- **Measurement campaign 3** was also carried out in Carnarvon at the Klerefontein receiver support base using a MeerKAT UHF-band receiver as the test cryostat. This was the second measurement carried out with the attenuator cooled to 18 K. The goal of this measurement was to implement improvements to reduce the thermal gradient across the attenuator to measure the physical temperature of the resistive element internal to the attenuator more accurately.

For the testing using the MeerKAT UHF-band receiver, a cooldown cycle of six hours and a warmup cycle of six hours was required per measurement. This means that only one measurement was able to be carried out per day.

5.1 Measurement campaign 1: Liquid nitrogen testing

5.1.1 Introduction

In order to prove the cold attenuator measurement method, a test was done in the lab using liquid nitrogen (LN_2) as the cryogen to cool the attenuator to 77 K. Figure 5.1 and Figure 5.2 illustrate the measurement setup. In this configuration, the amplifier under test (AUT) is an ambient temperature amplifier and is located outside the cryogen. Consequently, both transmission lines need to be characterised and the $T_{e\,TX\,line\,2}$ will add significantly to the noise generated by the cold attenuator. This differs significantly from the final test configuration where the attenuator is directly connected to the AUT.

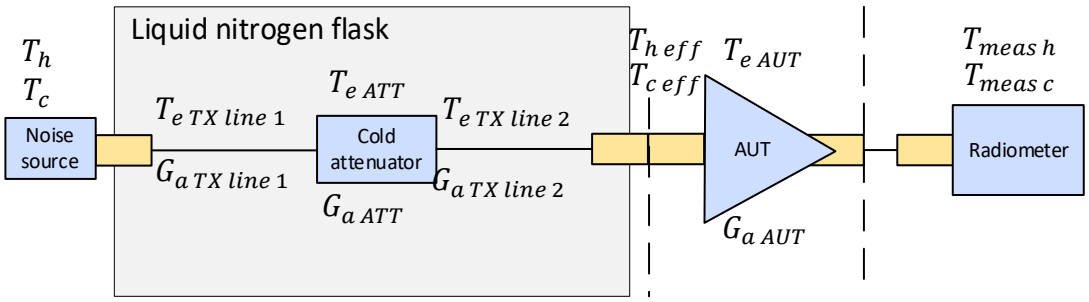

Figure 5.1. The LN_2 cold attenuator measurement block diagram.

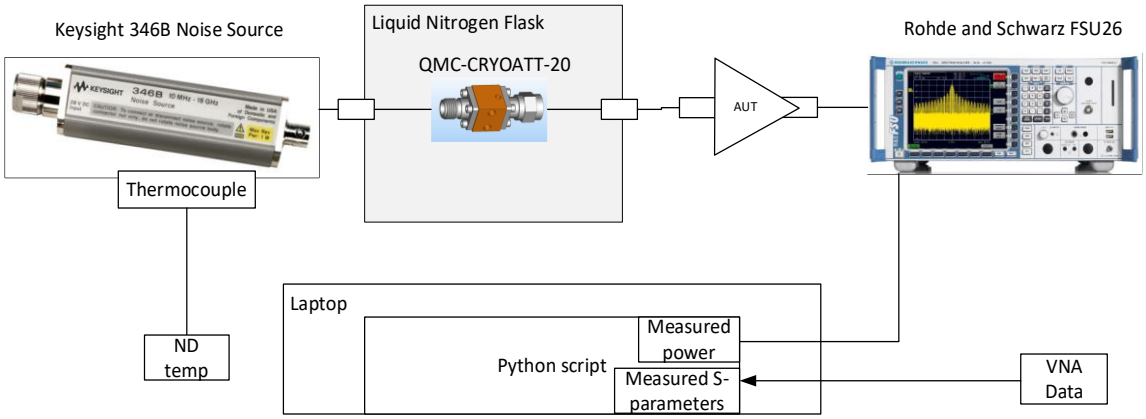

Figure 5.2. The cold attenuator measurement LN_2 block diagram.

The main purpose of the first few steps are to measure the values required to solve the equations (5.1) and (5.2) :

$$T_{h\,eff} = [(\mathrm{T_h} + T_{e\,TX\,line\,1})G_{a\,TX\,line\,1}G_{a\,ATT} + (T_{phys\,ATT}(1 - G_{a\,ATT}) + T_{e\,TX\,line\,2})]G_{a\,TX\,line\,2} \quad (5.1)$$

$$T_{c\,eff} = [(\mathrm{T_c} + T_{e\,TX\,line\,1})G_{a\,TX\,line\,1}G_{a\,ATT} + (T_{phys\,ATT}(1 - G_{a\,ATT}) + T_{e\,TX\,line\,2})]G_{a\,TX\,line\,2} \quad (5.2)$$

5.1.2 Finding T_h and T_c

The measured ENR of both noise sources is specified at discreet frequency points from the manufacturer. In order to generate an array of ENR values over the band of interest for use in the noise calculations, an interpolation[12] was carried out as shown in Figure 5.3 and Figure 5.4. In both plots:

- The blue trace is the ENR values provided by the manufacturer.
- The red bars show the uncertainty specified by the manufacturer.
- The orange trace is the resultant interpolated array used in the calculations.

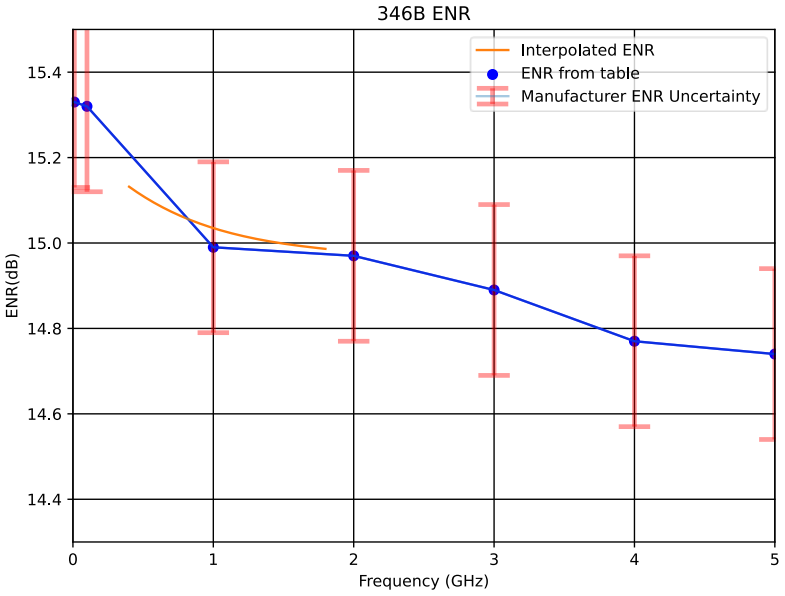

Figure 5.3. The ENR interpolation for the 346B noise source.

[12] Refer to Appendix E - Interpolation script for noise diode ENR values. A 10th order polynomial fit was used to generate the array.

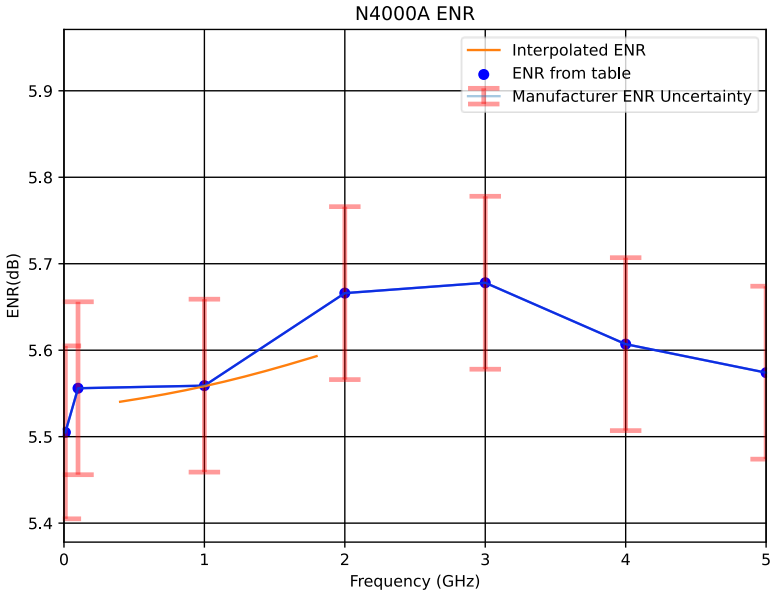

Figure 5.4. The ENR interpolation for the N4000A noise source.

The value for T_c is recorded using a multimeter and thermocouple that was manually recorded by the author during the test. The method was automated by reading the temperature via the serial port in measurement campaign 3. Once T_c is known, then T_h can be calculated using the ENR table and equation (4.2) to result in the plot shown in Figure 5.5. This is used to calculate $T_{h\,eff}$ and $T_{c\,eff}$ delivered to the amplifier under test.

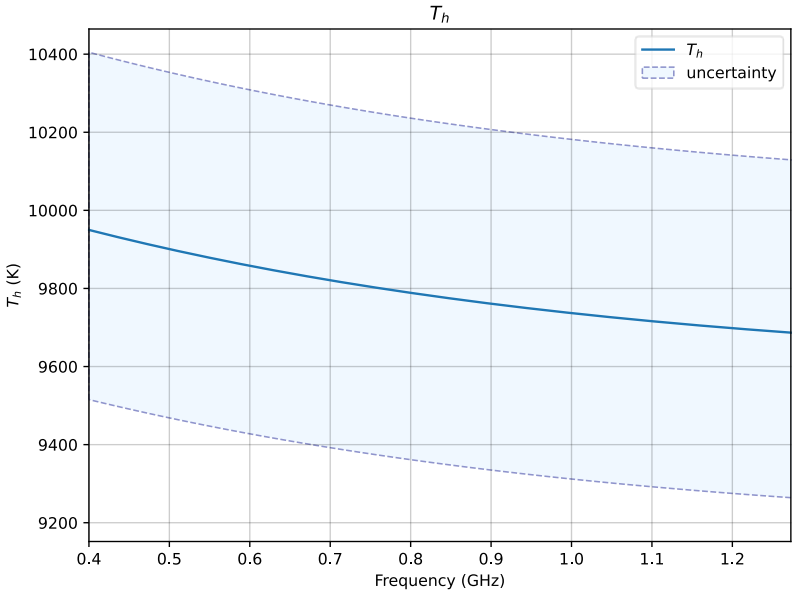

Figure 5.5. Plotted T_h values showing the uncertainty due to the noise source calibration uncertainty.

5.1.3 Finding $G_{a\ ATT}$

The attenuator was tested using liquid nitrogen (LN_2) to determine the change in attenuation from 300 K to 77 K. It is not possible to measure the attenuator directly when it is cooled, thus the measurement shown in Figure 5.6 was carried out using the following measurement steps:

Step 1: The VNA measurement of the attenuator and transmission (TX) lines was carried out at an ambient temperature of 300 K.

Step 2: The transmission lines were connected and submerged in the LN_2 and the VNA measurement of the $|S_{21\ TX\ line\ 1}|\text{dB} + |S_{21\ TX\ line\ 2}|\text{dB}$ was taken.

Step 3: The attenuator was inserted between the TX lines and then submerged in the liquid nitrogen and the measurement $|S_{21\ TX\ line\ 1}|\text{dB} + |S_{21\ ATT}|\text{dB} + |S_{21\ TX\ line\ 2}|\text{dB}$ was taken.

Step 4: The attenuator loss was calculated by de-embedding the attenuator $|S_{21}|$ value from the cascade. The result is plotted on Figure 5.7.

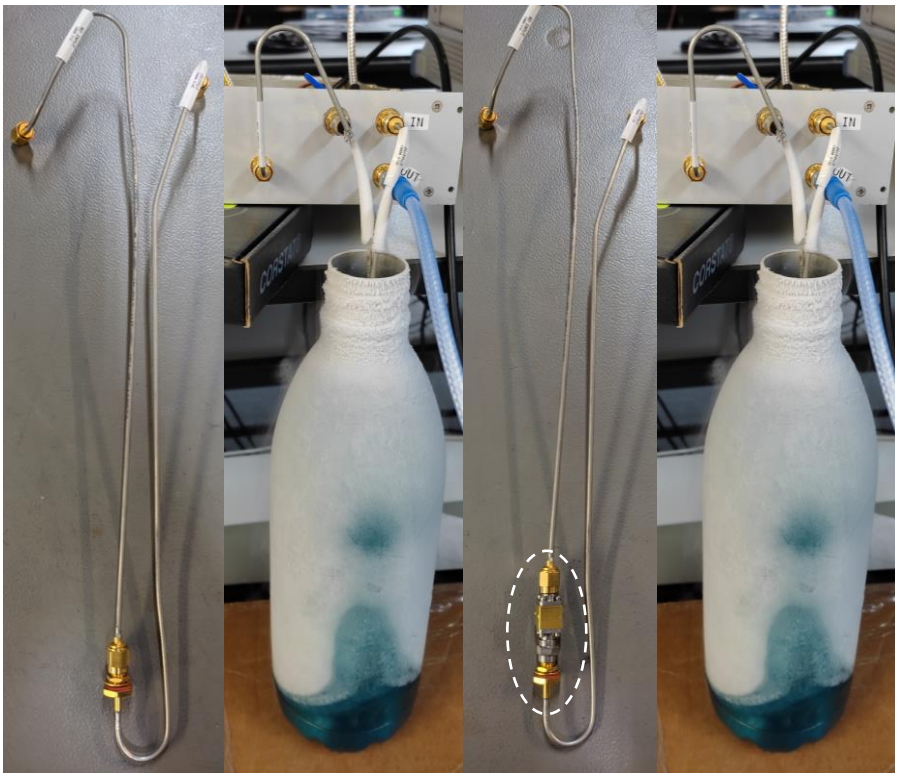

Figure 5.6. The TX lines and attenuator measured at a physical temperature of 77K. The attenuator is circled.

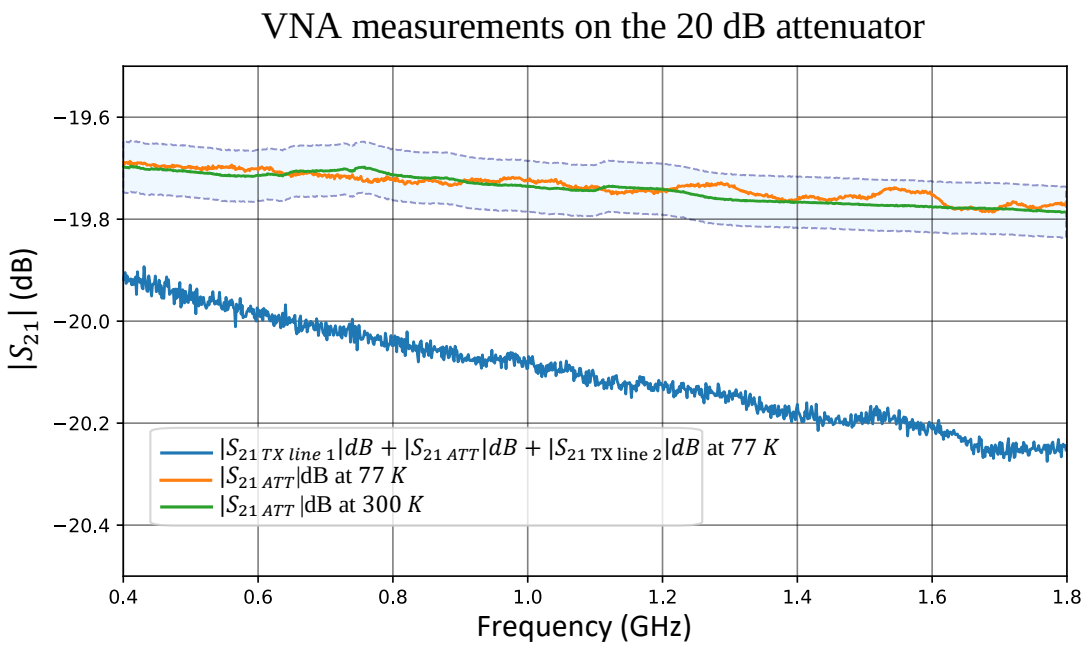

Figure 5.7. The $|S_{21}|$dB of the attenuator measured directly at ambient temperature and de-embedded at a physical temperature of 77 K. The measurement accuracy of 0.1 dB is shown.

Based on these results, the $|S_{21\,ATT}|$dB of the attenuator is assumed to be invariant with physical temperature between 300 K and 77 K.

Based on the noise source S_{11} measurements Figure 4.8 and Figure 4.9, the available gain (G_a) of the attenuator is calculated and shown in Figure 5.8.

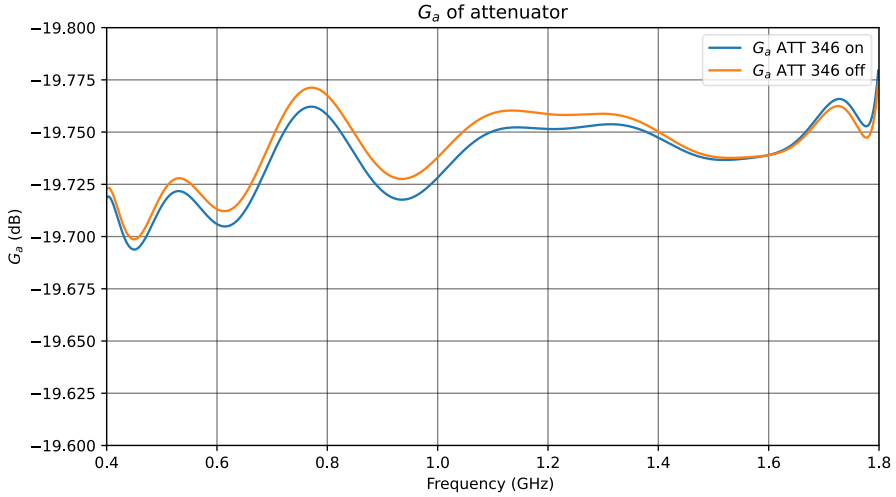

Figure 5.8. $G_{a\,ATT}$ for different noise diodes states.

5.1.4 Finding $G_{i\,TX\,line\,1}$ and $T_{e\,TX\,line\,1}$

Note that for this section, the $G_{i\,TX\,line\,1}$ is equal to the magnitude of the S-parameter power ratio measured across the transmission line $|S_{21}|$ and these terms are used interchangeably. The transmission lines are connected back-to-back, and the cold side was submerged in the LN_2 as shown in Figure 5.9 and Figure 5.10. $G_{i\,TX\,line\,1}G_{i\,TX\,line\,2}$ is measured using the VNA. $G_{i\,TX\,line\,1}$ is estimated by taking the square root $\sqrt{G_{i\,TX\,line\,1}G_{i\,TX\,line\,2}}$.

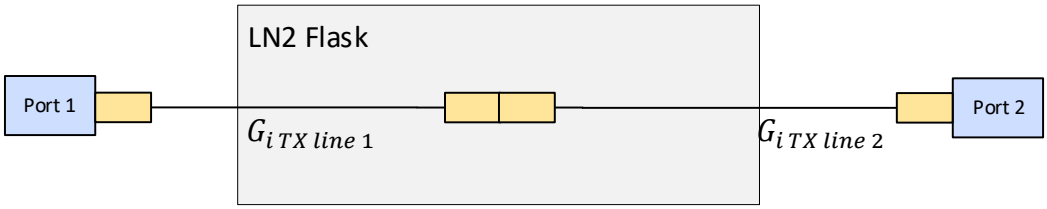

Figure 5.9. Measurement of $G_{i\,TX\,line\,1}G_{i\,TX\,line\,2}$ using a VNA.

Figure 5.10. The transmission lines and attenuator measured at 77 K.

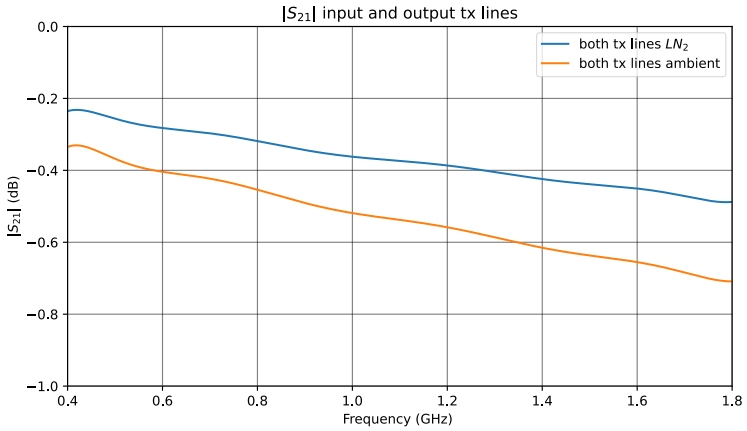

Figure 5.11. The $|S_{21}|$ of both the transmission lines measured directly at ambient temperature and at a physical temperature of 77K.

Figure 5.11 shows the $|S_{21}|$ values of both transmission lines measured directly using the VNA with the transmission lines at ambient and cooled using the LN_2. Referring to Figure 5.12, the $G_{i\,TX\,line\,1}$ is estimated by calculating $\sqrt{G_{i\,TX\,line\,1}G_{i\,TX\,line\,2}}$. This value is reasonable when compared to a VNA measurement of a single transmission line at ambient temperature.

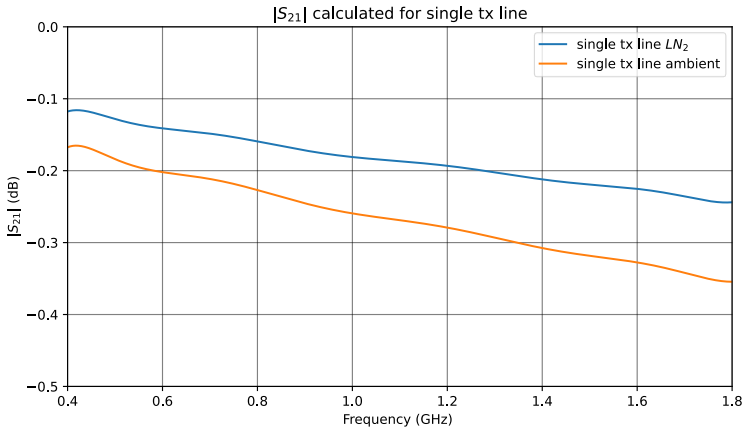

Figure 5.12. Estimated cooled $G_{i\,TX\,line\,1}$ (blue trace) compared to the measured ambient $|S_{21}|$ $(orange\ trace)$.

5.1.5 Determining $T_{e\,TX\,line\,1}$

Once the value for $G_{i\,TX\,line\,1}$ is determined, the physical temperature can be used to estimate the noise temperature.

$T_{e\,TX\,line\,1}$ can be estimated by a variation of equation (3.21):

$$T_{phys\,TX\,line\,1} = T_{phys\,TX\,line\,2} = \frac{T_{amb} + T_{cold}}{2} \tag{5.3}$$

In this case, $T_{amb} = 300$ K and $T_{cold} = 77$ K and the $T_{phys\,TX\,line\,1} = 188.5\ K$

The equivalent noise temperature of the transmission line can be found by adapting equation (2.7) to form the following:

$$T_{e\,TX\,line1} = T_{phys\ TX\,line\,1}\left(\frac{1}{G_{iTX\,Line\,1}} - 1\right) \tag{5.4}$$

This calculation was performed using the $G_{iTX\,Line\,1}$ plotted in Figure 5.12 and the result is plotted in Figure 5.13.

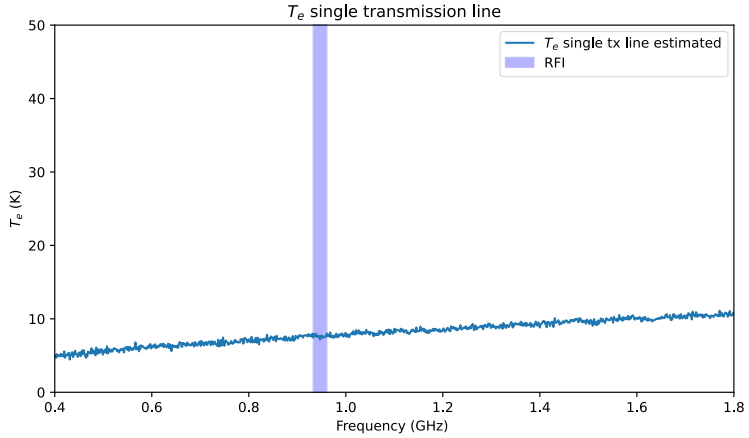

Figure 5.13. Equivalent noise temperature of the transmission line ($T_{e\,TX\,line\,1}$). Note the RFI[13] masked using the purple block.

5.1.6 Determining $T_{e\,cas}$ from a Y-factor radiometer measurement

The values for $T_{h\,eff}$ and $T_{c\,eff}$ were calculated according to the equations (5.1) and (5.2). The resultant arrays are plotted in Figure 5.14.

[13] The RFI that is present is due to the 900 MHz GSM band that is present and unavoidable in the lab at Black River Park. Although it is possible to perform the measurement in a RFI shielded environment, the additional effort is not justified as the measurement results are still adequate.

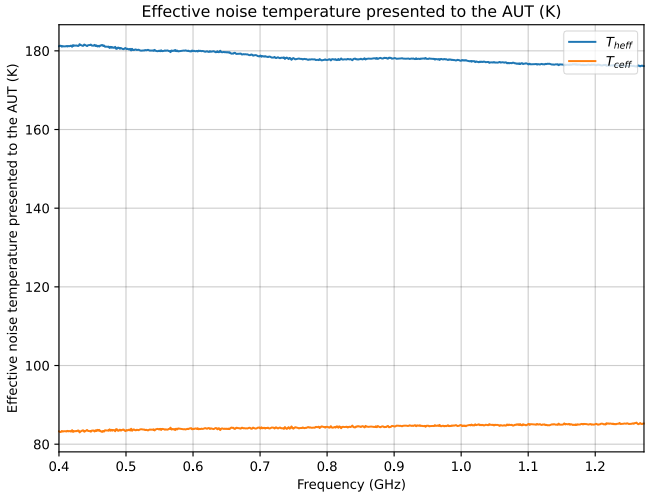

Figure 5.14. $T_{h\,eff}$ and $T_{c\,eff}$ presented to the AUT.

The Y-factor measurement is carried out with the AUT connected as per Figure 5.15. The measured Y-factor is plotted in Figure 5.16.

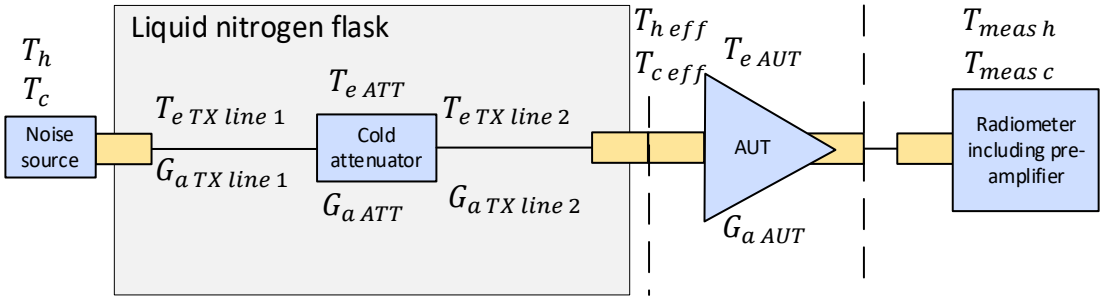

Figure 5.15. The LN_2 cold attenuator measurement block diagram.

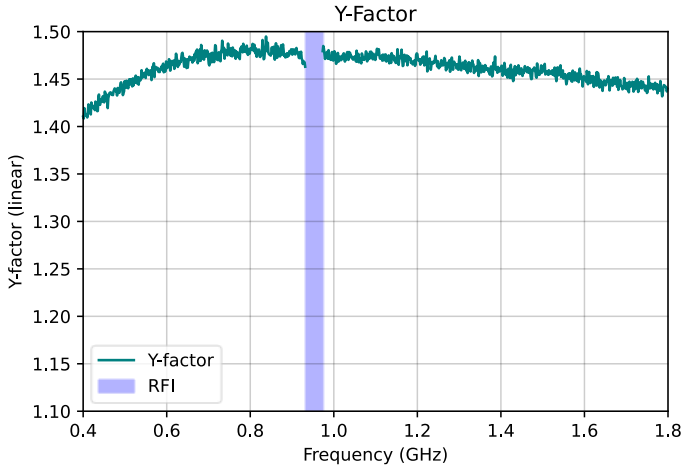

Figure 5.16. Measured Y-factor.

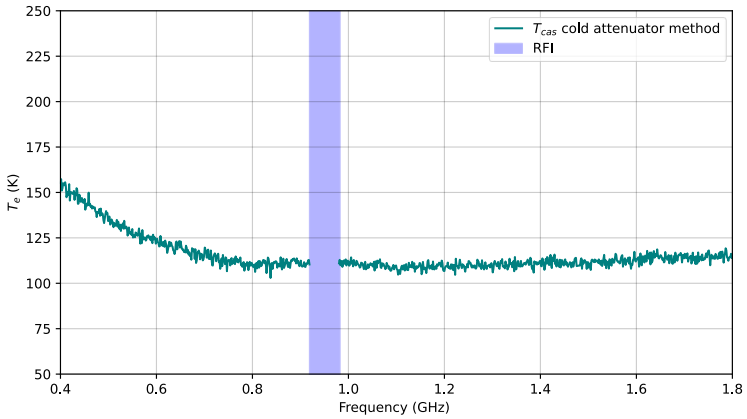

Figure 5.17. Measured cascaded equivalent noise temperature.

The Y-factor is used to calculate the cascaded noise temperature T_{cas}, shown on Figure 5.17. The noise contribution of the pre-amplifier and spectrum analyser need to be removed to determine the noise temperature of the amplifier under test ($T_{e\ AUT}$).

5.1.7 Second stage effect removal

Equation 5.5 is used to remove the second stage effect and determine $T_{e\ AUT}$.

$$T_{e\ AUT} = T_{e\ cas} - \frac{T_{e\ 2nd\ stage}}{G_{a\ AUT}} \tag{5.5}$$

5.1.8 Gain of the AUT ($G_{a\ AUT}$)

The vector network analyser was used to measure the S-parameters of the AUT. Figure 5.18 shows the results of the insertion gain (G_i), calculated from the $|S_{21}|^2$ and the available gain, calculated using the S-parameters for the AUT and the measured output S_{22} of the transmission line, attenuator and transmission line.

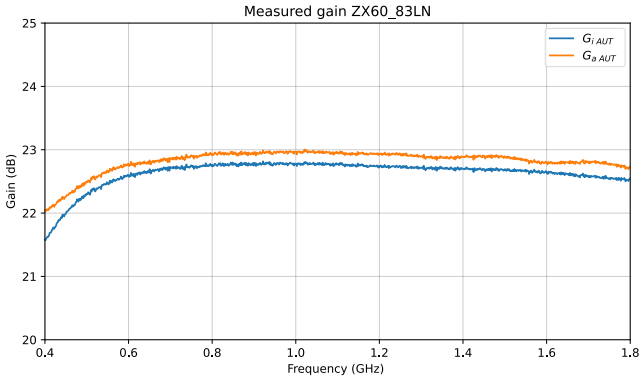

Figure 5.18. The measured insertion gain (G_i) and available gain (G_a) of the AUT.

5.1.9 Equivalent noise temperature of the second stage network

The equivalent noise temperature of the second stage network is determined using a standard Y-factor measurement. Figure 5.19 shows a block diagram of this measurement and Figure 5.20 shows the resultant equivalent noise temperature.

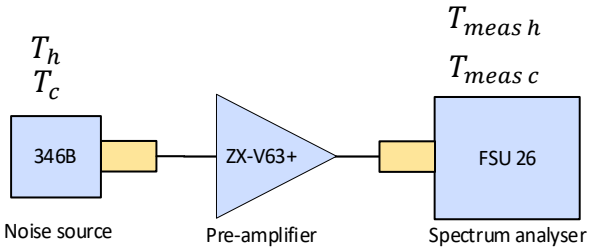

Figure 5.19. The second stage equivalent noise temperature measurement block diagram.

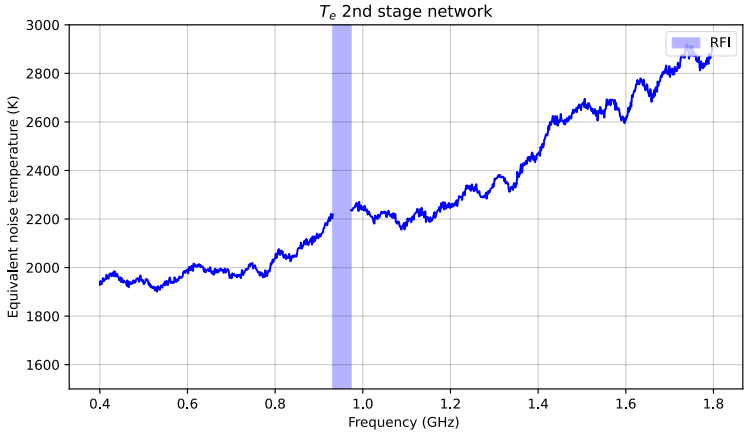

Figure 5.20. The measured equivalent noise temperature of the second stage network.

5.1.10 Measurement campaign 1 results, conclusions and suggestions

The final result is shown in Figure 5.21. It shows the measured cascaded equivalent noise temperature and the de-embedded amplifier under test equivalent noise temperature.

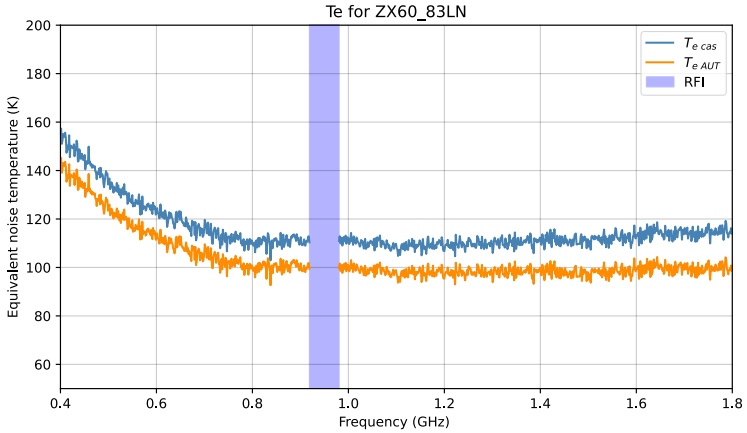

Figure 5.21. Measured cascaded noise temperature and de-embedded equivalent noise temperature.

To give context to the measured values, a standard Y-factor measurement was carried out and the noise figure was extracted from the datasheet. These are compared in Figure 5.22 and show good agreement.

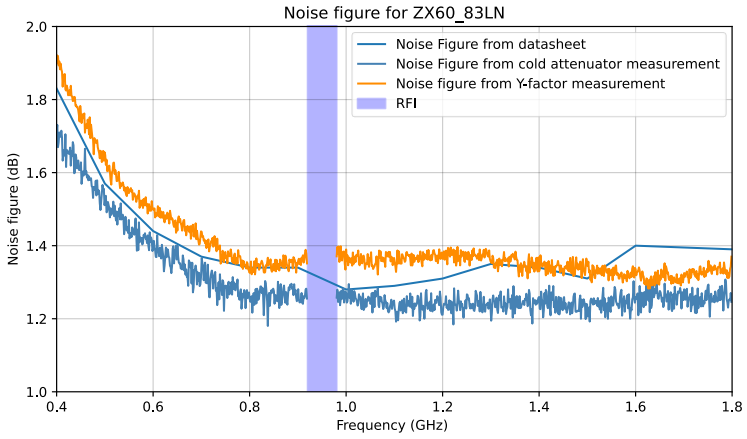

Figure 5.22. Noise figure measured from the cold attenuator method compared to the standard Y-factor method and the data extracted from the datasheet.

The largest potential source of experimental error was determining the noise contribution of the output transmission line. This does not present an issue with measurement campaign 2 and 3 as

the attenuator is the same temperature as the AUT and the output transmission line from the attenuator to the AUT is kept very short to minimise insertion loss.

The second largest source of experimental error is the accurate determination of the physical temperature or the attenuator attenuation element. The cryogenic temperature sensors were not available for this testing so it was assumed that the attenuator case and attenuation element inside were cooled to 77.355 K with no temperature gradient.

The third largest source of experimental error is controlling the level of the LN_2 in the Dewar. The variation results in the length of the transmission cables submerged in the liquid changing as the level of the LN_2 changes.

During this testing the method for interpolation of the T_h value for the noise diode was created, the attenuation of the attenuator was declared to be essentially invariant when cooled to 77 K, and the noise sources and radiometers were characterised on the network analyser.

The cold attenuator method was successfully completed and measurement campaign 2 was planned to proceed.

5.2 Measurement campaign 2: Cryostat with helium refrigerant cryocooler

5.2.1 Introduction

The planning of this measurement campaign presented two main challenges. Firstly, each measurement required a cooldown cycle and warmup cycle. The cryostat cold head requires six hours to cool down and six hours to warm up to room temperature. This meant that only one measurement was able to be completed per day. Additionally, one of the days was lost due to equipment malfunction.

The measurement procedure is outlined here with the measurement block diagram presented in Figure 5.23. The main purpose of steps one, two and three are to measure the values required to solve the equations :

$$T_{h\,eff} = (T_h + T_{e\,TX\,line\,1})G_{a\,TX\,line\,1}G_{a\,ATT} + T_{phys\,ATT}(1 - G_{a\,ATT}) \tag{5.6}$$

$$T_{c\,eff} = (T_c + T_{e\,TX\,line\,1})G_{a\,TX\,line\,1}G_{a\,ATT} + T_{phys\,ATT}(1 - G_{a\,ATT}) \tag{5.7}$$

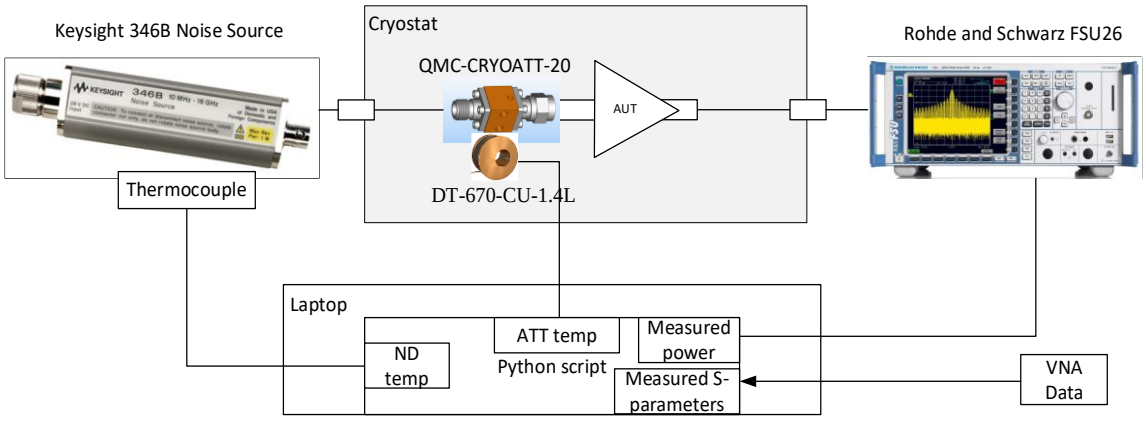

Figure 5.23. The cold attenuator measurement block diagram.

5.2.2 Finding T_h and T_c

The noise diode excess noise ratio (ENR) interpolation arrays that were generated in the first measurement campaign were used to determine T_h and T_c. The multimeter with thermocouple was used to measure the noise diode case temperature.

Figure 5.24. Recording the T_c value.

Once T_c is known, then T_h can be calculated using the ENR table and equation (4.2) to result in the plot shown in Figure 5.25.

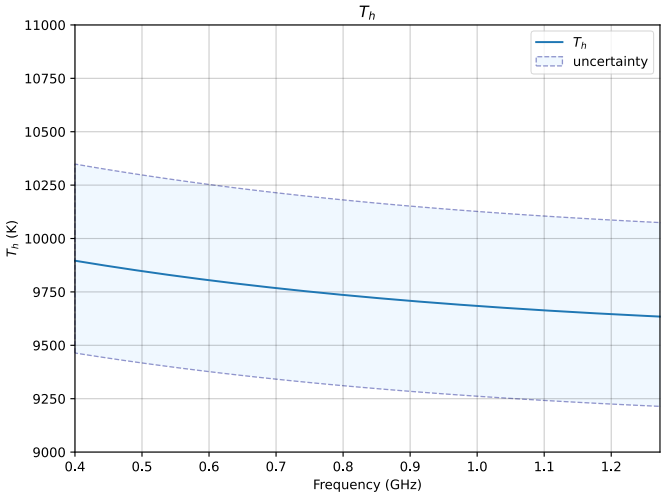

Figure 5.25. Plotted T_h values.

5.2.3 Finding $G_{a\ ATT}$

The S-parameters of the attenuator is measured at ambient using a vector network analyser. It was shown in section 5.1.3 that the attenuator insertion loss is invariant from 300 K to 77 K. This will be assumed[14] to be valid to 18 K for this test.

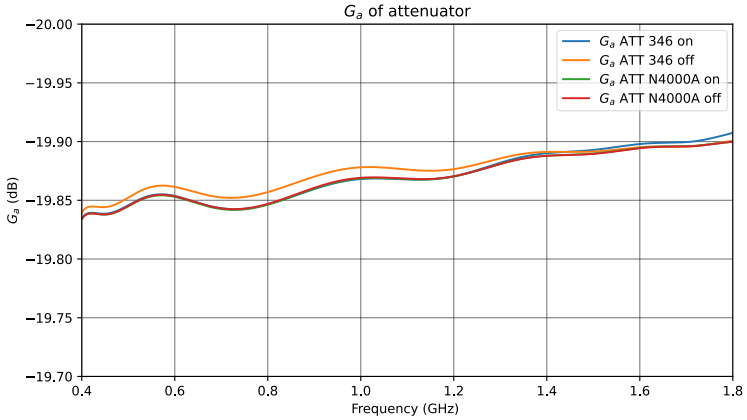

Figure 5.26. $G_{a\ ATT}$ for different noise diodes and states. Note that three of the traces are essentially identical, while the $G_{a\ ATT}$ for the 346 in the off state is slightly different.

Using the equation (2.10), the available gain of the attenuator ($G_{a\ ATT}$) is calculated for the noise diode on and noise diode off states. Figure 5.26 shows the available gain of the attenuator. Note the slight different between the on and off state for the 346 B noise source due to the difference in matching.

5.2.4 Finding $T_{e\ TX\ line\ 1}$ and $G_{a\ TX\ line\ 1}$

During this test there was not a convenient way of anchoring the transmission lines to the cold plate on their own. Instead, two attenuators were mounted to the cold head and the short jumper cable was connected in-line to create a through-path. If the assumption is valid that the attenuator is invariant with temperature, then the characteristics of the transmission lines can be determined from this measurement. Figure 5.27 shows a block diagram of the measurement.

[14] This assumption is also based on the information shown in the manufacturer datasheet [80].

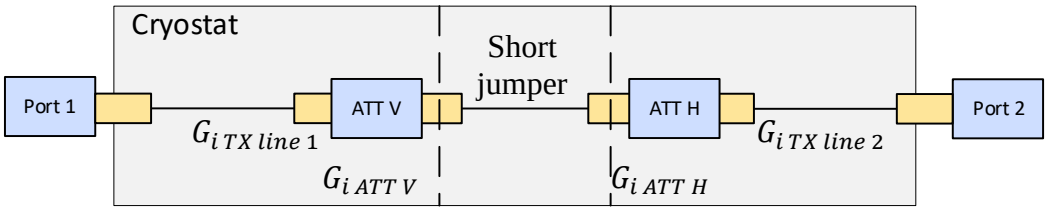

Figure 5.27. Measurement of $G_{i\,TX\,line\,1}G_{i\,TX\,line\,2}$ using a VNA. Note the two attenuators used to thermally anchor the cold side of the transmission lines to the cold plate.

The cold head is shown in Figure 5.28. The female-to-female SMA adaptors are included as part of the attenuators for the calibration.

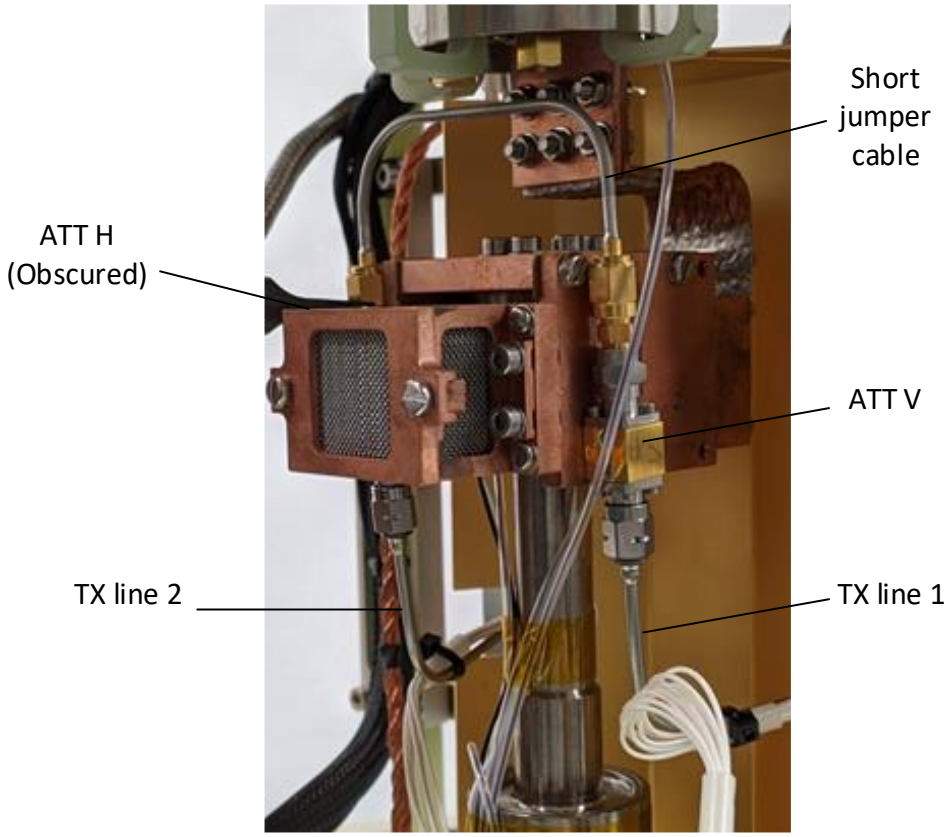

Figure 5.28. The cold head configuration used for the measurement of $G_{i\,TX\,line\,1}G_{i\,TX\,line\,2}$ using a VNA. Note the attenuators used to thermally anchor the cold side of the transmission lines to the cold plate.

The cryostat was cooled down and the measurement was carried out of the entire cascade consisting of the two attenuators and the transmission lines. The results are presented in Figure

5.29 and compared with the same measurement taken at ambient temperature to show the change in insertion loss of approximately 0.2 dB between ambient and cooled.

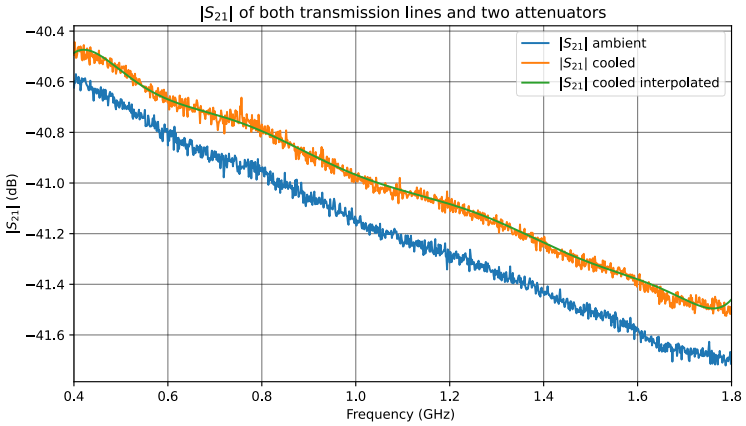

Figure 5.29. The measured G_{i} for the cascade including transmission lines and two attenuators.

The attenuators (including female-to-female SMA adaptors) are measured using the VNA at ambient and then subtracted from the results of the measurement as displayed in Figure 5.29 to result in Figure 5.30. Additionally, shown in Figure 5.30 are the two transmission lines measured at ambient temperature separately and summed.

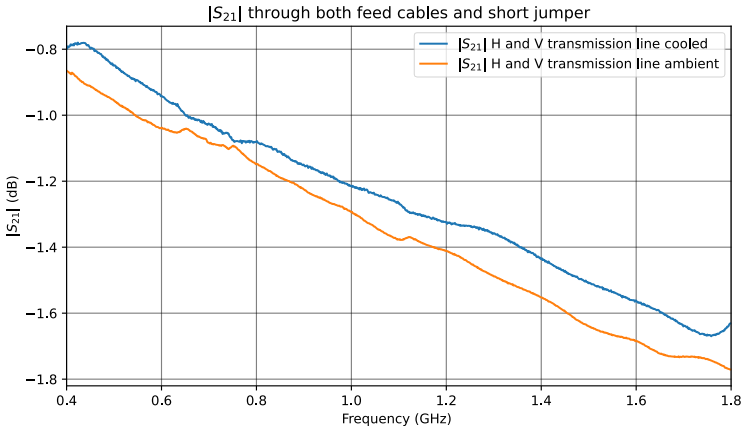

Figure 5.30. The measured G_{i} for the two transmission lines including the short jumper cable.

Note that the channels are labelled horizontal polarisation (H) and vertical polarisation (V) in the system that was used as the testbed. V is used as TX Line 1 and H is used as TX line 2.

$G_{i\,TX\ line\,1}$ is estimated from the values in Figure 5.30 by applying the formula $\sqrt{G_{i\,TX\ line\,1}G_{i\,TX\ line\,2}}$ to result in Figure 5.31. Also shown is the $G_{i\,TX\ line\,1}$ measured directly using the VNA at ambient temperature before closing the cryostat. This showed good agreement.

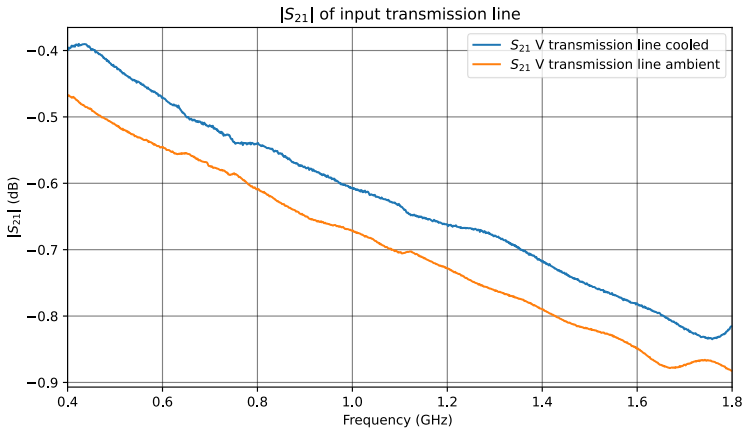

Figure 5.31. The calculated cooled $G_{i\,TX\ line\,1}$ (blue trace). The ambient $|S_{21}|$ is measured using the VNA (orange trace).

Physical temperature estimation of T_e

$T_{e\,TX\ line\,1}$ and $T_{e\,TX\ line\,2}$ can be estimated by a variation of equation (3.21):

$$T_{phys\,TX\ line\,1} = T_{phys\,TX\ line\,2} = \frac{T_{amb} + T_{phys\ ATT}}{2} \tag{5.8}$$

For this calculation, the following are used:

- The $T_{amb} = 300$ K,
- the $T_{phys\ ATT} = 18$ K,
- the $T_{phys\,TX\ line\,1} = 159\ K$.

The equivalent noise temperature of the transmission line ($T_{e\,TX\ line\,1}$) can be determined using the below equation and is plotted in Figure 5.32:

$$T_{e\,TX\ line\,1} = T_{phys\ TX\ line\,1}\left(\frac{1}{G_{i\,TX\ Line\,1}} - 1\right) \tag{5.9}$$

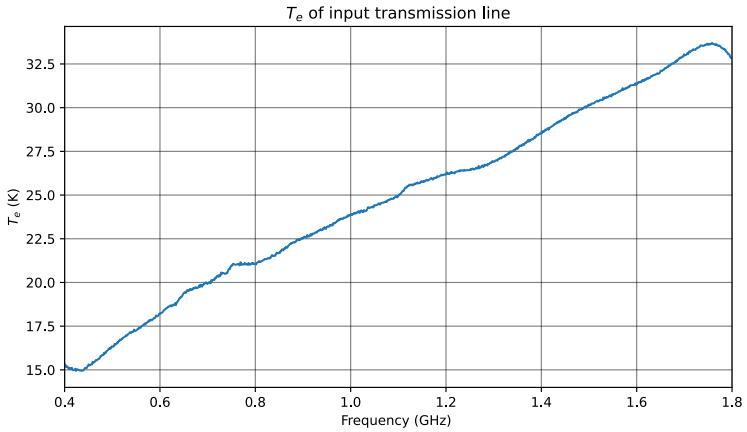

Figure 5.32. The effective noise temperature of the input transmission line ($T_{e\,TX\,line\,1}$).

This noise contribution is added to the noise source and then attenuated by the attenuator.

5.2.5 Determining $T_{e\,cas}$ from a Y-factor radiometer measurement

The amplifier under test was installed and the final measurement was carried for the full cascade as shown in Figure 5.33 and Figure 5.34.

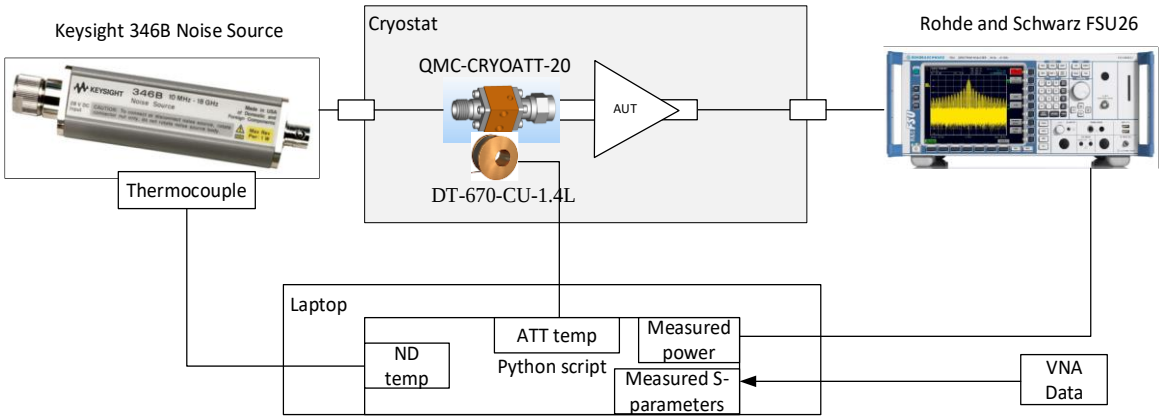

Figure 5.33. The cold attenuator measurement block diagram.

Figure 5.34. The cold attenuator measurement with the AUT on the cold plate.

Figure 5.35 shows the Y-factor based on the spectrum analyser measurements. This shows that there is a good ratio between the hot and cold measurements. Leffel and Daniel (2012) suggest that a good Y-factor ratio is 5 dB or a linear ratio of 3.16 [42].

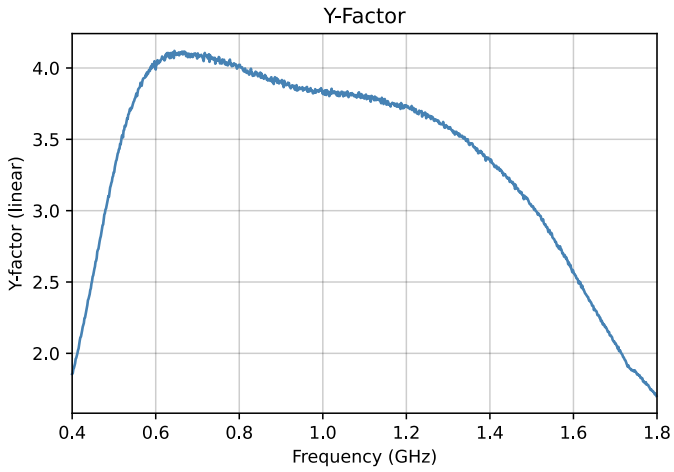

Figure 5.35. Measured Y-factor.

After the Y-factor is measured, the effective noise temperature presented to the AUT can be calculated. Equations (3.26) and (3.27) are used to calculate the $T_{h\,eff}$ and $T_{c\,eff}$ values presented to the AUT. The results of this are shown on Figure 5.36.

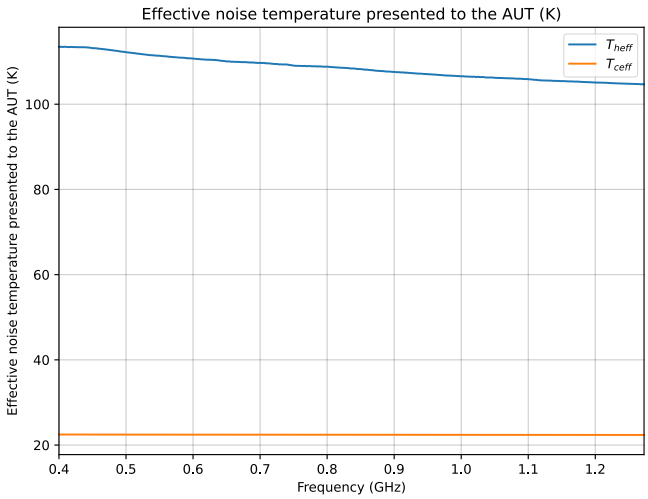

Figure 5.36. $T_{h\,eff}$ and $T_{c\,eff}$ presented to the AUT.

The Y-factor is used with equations (3.24) and (3.25) to calculate the equivalent noise temperature of the cascade. The result is shown on Figure 5.35. Note that the effect of the second stage needs to be removed.

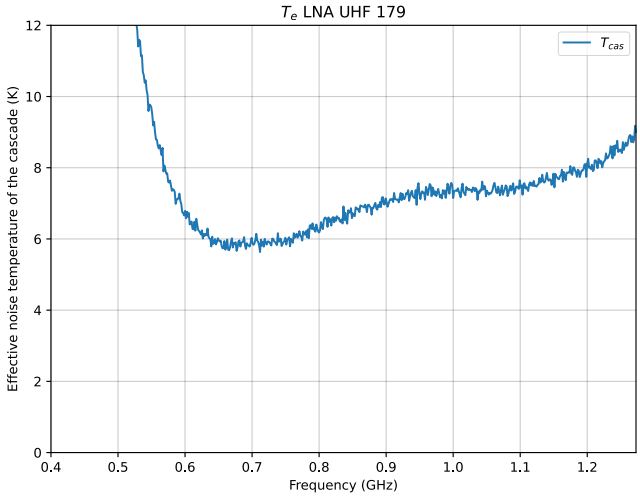

Figure 5.37. The effective noise temperature of the cascade.

5.2.6 Second stage effect removal

Once $T_{e\,cas}$ is calculated, the below equation is used to remove the second stage effect and determine $T_{e\,AUT}$.

$$T_{e\,AUT} = T_{e\,cas} - \frac{T_{e\,2nd\,stage}}{G_{a\,AUT}} \tag{5.10}$$

The second stage terms are found in the preceding sections.

5.2.7 Gain of the AUT ($G_{a\ AUT}$)

Figure 5.38. shows the insertion gain derived from the de-embedding the AUT $|S_{21}|$ value from the VNA measurement taken with the attenuator, transmission lines and the AUT. The $|S_{11}|$ and $|S_{22}|$ data provided by the AUT supplier was used to generate the G_a plot.

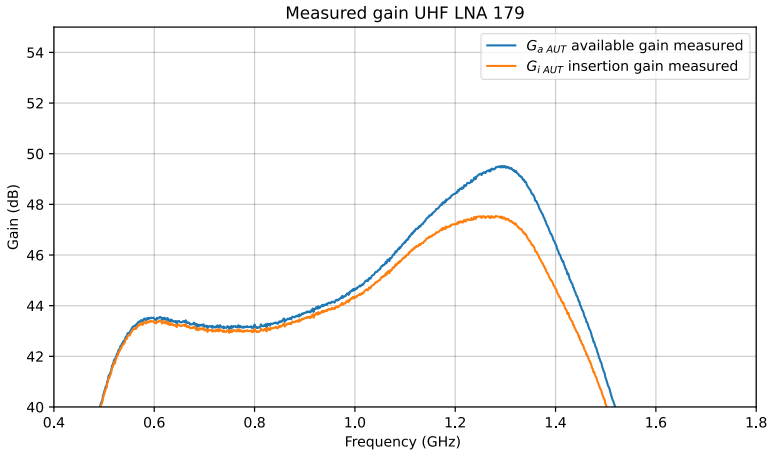

Figure 5.38. AUT Gain.

5.2.8 Equivalent noise temperature of the radiometer ($T_{e\ 2nd\ stage}$)

The spectrum analyser set to 5 dB attenuation and an external preamp is used for this measurement as shown in the block diagram of Figure 5.39. The result is shown in Figure 5.40.

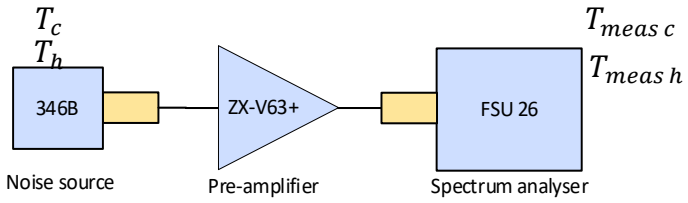

Figure 5.39. The second stage equivalent noise temperature measurement block diagram.

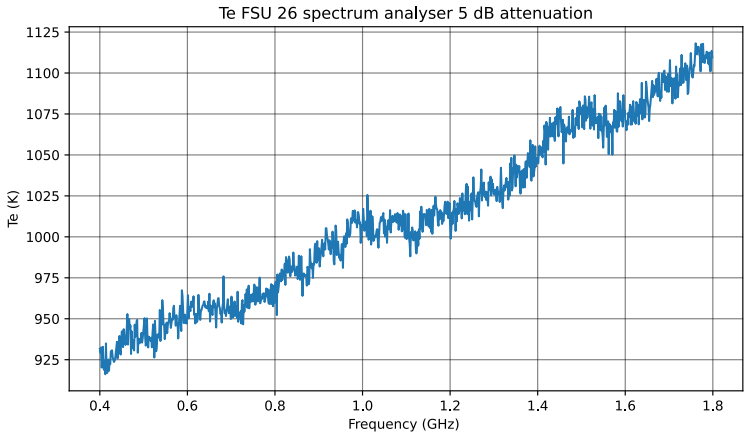

Figure 5.40. The measured equivalent noise temperature of the second stage.

5.2.9 Measurement campaign 2 results, conclusions and suggestions

The final measurement is shown in Figure 5.41. This is higher than expected as the supplier test data showed that the equivalent noise temperature of the LNA is less than 2 K between 600 MHz and 1.1 GHz.

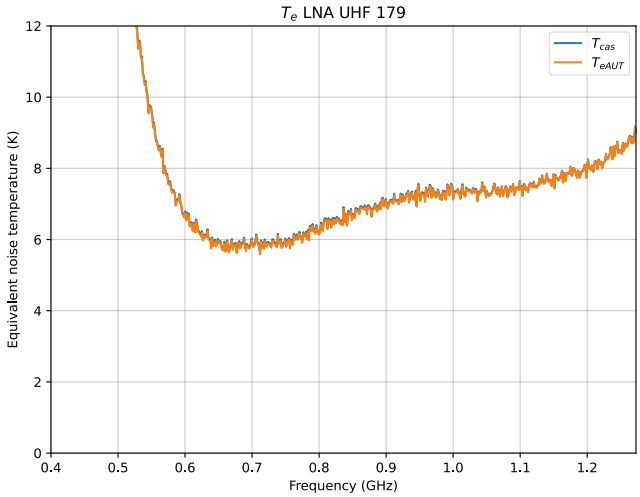

Figure 5.41. The equivalent noise temperature of the cascade and the AUT. Due to the use of the preamplifier and the high gain of the AUT both traces are very similar and essentially overlayed.

The largest source of experimental error is the uncertainty of the physical temperature of the resistive element inside the attenuator. The attenuator forms a thermal noise standard during the measurement; thus any uncertainty will contribute directly to an offset in the equivalent noise temperature. Figure 5.42 shows the location of the attenuator and the temperature sensor on the other side of the cold plate. Examining Russel and Weinreb (2012), Cano, Wadefalk and

Gallego-Puyol (2010), and Akgiray *et al*. (2013), the temperature sensor is usually installed inside or on the attenuator casing. An improvement would be to fix the sensor directly to the case [68][69][73].

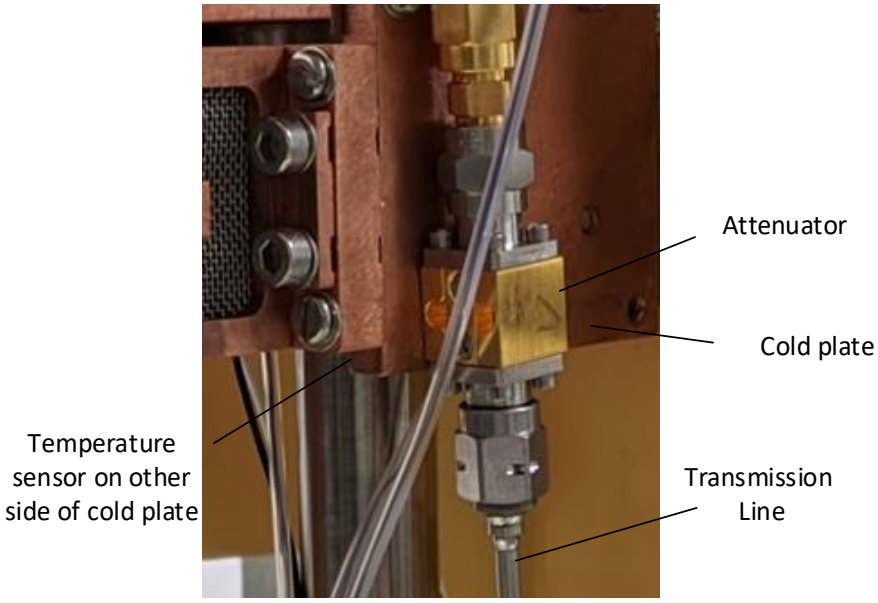

Figure 5.42. The cold attenuator location with the temperature sensor on the cold plate.

The equivalent noise temperature appears to be approximately 4 K higher than expected. Assuming that the temperature measurement is the cause of this error, 4 K was added to the temperature reading and the python script was run again to calculate the resultant equivalent noise temperature. The result of this is shown in Figure 5.43. There is a direct relationship between the attenuator temperature reading and the resultant equivalent noise temperature. The equivalent noise temperature data provided by the supplier is shown as the green trace for comparison.

A thermal study was conducted to determine if the thermal gradient across the attenuator can be in the order of 4 K.

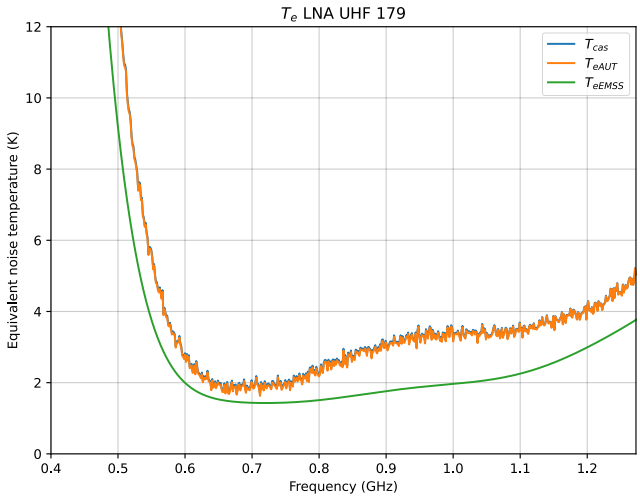

Figure 5.43. The effect of manually adding 4 K to the measured attenuator temperature.

A further improvement is the ability to read the temperature of the noise diode case directly into the python script via a serial port.

5.3 Thermal study

5.3.1 Introduction

The effective noise temperature that was measured in the measurement campaign 2 was approximately three times higher than expected. One of the possible explanations for this is that the temperature distribution around the cold head is not well understood. Specifically, there is a difference between the temperature measured and the actual temperature of the resistive element inside the attenuator.

This is a limited study with the goal of showing the temperature gradient across the attenuator and finding a solution that lowers the temperature uncertainty.

5.3.2 Simulation setup

The attenuator model step file was imported into the thermal simulation software and the cold head structure was built. The materials were set to stainless steel and copper and the surrounding medium was set to near perfect vacuum. The effect of radiation was disabled as the focus of this simulation was to understand the thermal distribution due to conduction through the

materials on the cold head [83]. The coaxial cable modelled with a centre conductor of solid copper and diameter of 0.66 mm. This results in a cross-sectional area of 0.34 mm^2. The outer conductor is copper with a 0.44 mm^2 cross sectional area. The stainless-steel jacket surrounds the outer conductor. Refer to Appendix F for more information about the thermal simulation.

5.3.3 Initial simulation result and issue confirmation

The model of the cold head with the copper plates was simulated and the resultant surface temperatures are shown in Figure 5.44. Looking at the spot measurements point one, two and four on Figure 5.44 show a 2.03 K difference between the attenuator case and the inner conductor and a 2.81 K difference between the attenuator case and the cold plate. This shows that this temperature gradient across the attenuator is the possible major source of the 4 K measurement difference.

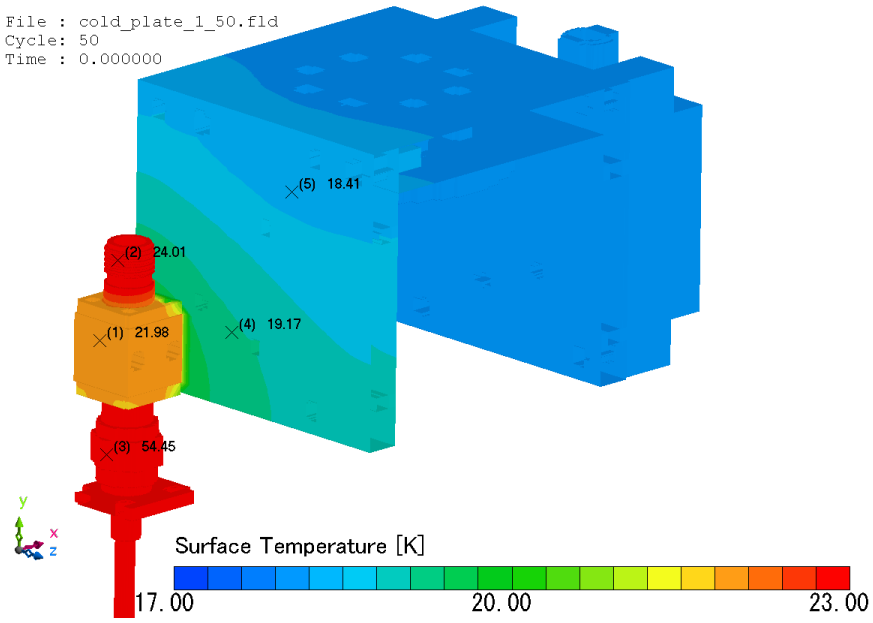

Figure 5.44. The thermal simulation showing the temperature gradient across the attenuator.

5.3.4 Final simulation verifying the proposed solution

It is not sufficient to measure the temperature of the attenuator on the cold plate, it must be measured on the attenuator body. The coaxial cable running between the cryostat wall and the attenuator should be thermally anchored to the cold plate before coupling to the attenuator. The solution shown in Figure 5.45 was chosen. This allows the coaxial transmission line to be pressed against the cold plate using two machined copper blocks, thus thermally anchoring the

outside of the cables before coupling to the attenuator. Figure 5.46 shows the simulated solution.

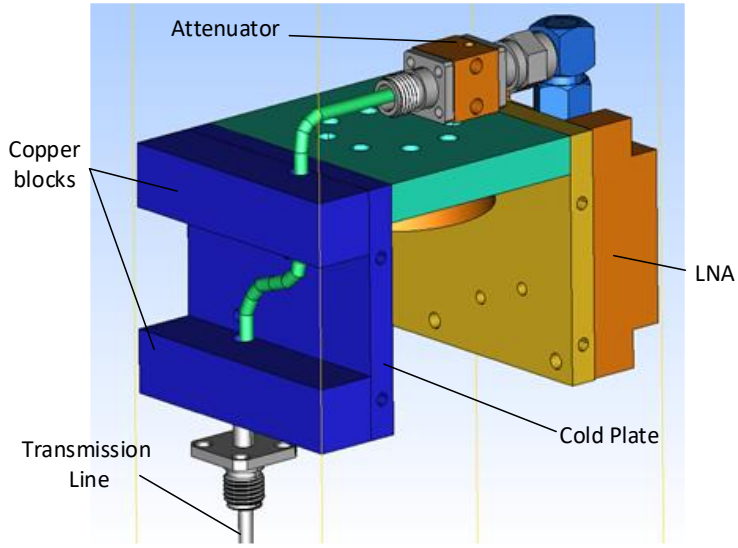

Figure 5.45. The suggested solution with the cable in contact with the cold plate

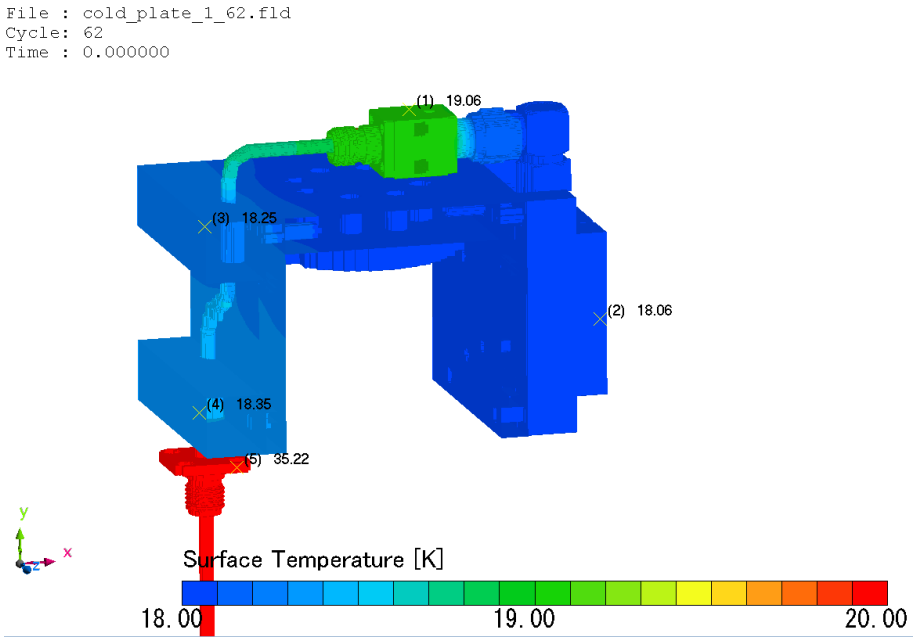

Figure 5.46. The suggested solution with the cable in contact with the cold plate. The worst-case predicted gradient across the attenuator is 1 K.

The attenuator is held in place by the right-angled SMA adaptor and the semi-rigid cable. Note that the attenuator is susceptible to vibration in this configuration. The coaxial cable was modelled without the PTFE dielectric. The utility of the simulation is to show that there is improvement, however due to assumptions made in the simulation it is unclear how well the centre conductor will carry the heat to the attenuator in practise.

5.4 Measurement campaign 3: Cryostat with helium refrigerant cryocooler, second test

5.4.1 Introduction

After the thermal study was completed, the copper anchoring blocks were manufactured.

This set of measurement was carried out at the receiver support facility located in Klerefontein[15]. The main goal was to address the uncertainty over the temperature sensing of the attenuator. For this measurement, the calibrated noise figure analyser was available and was used instead of the spectrum analyser. A serial-based temperature sensor was used to record the case temperature of the noise diode during the test. The test setup is shown in Figure 5.47. The new configuration of the cold head is shown in Figure 5.49.

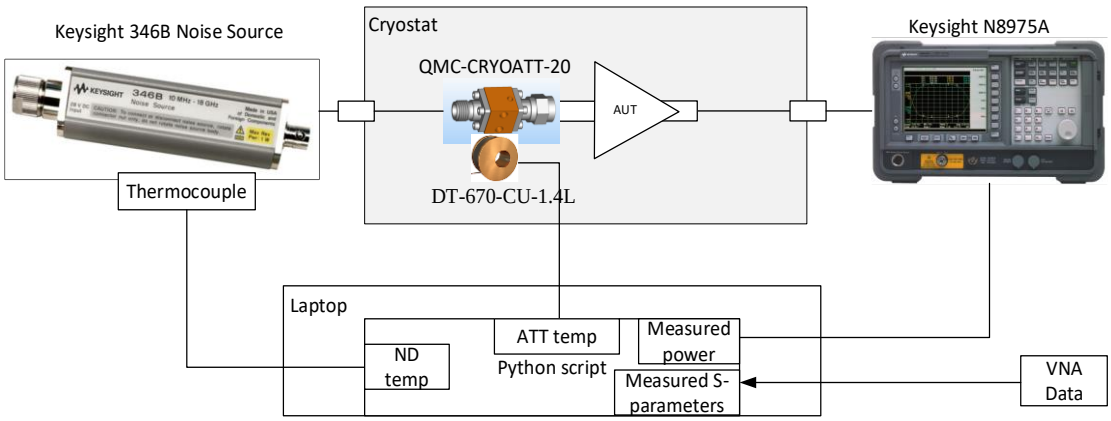

Figure 5.47. The final cold attenuator measurement block diagram.

Once again, the values required to solve the below equations need to be determined:

$$T_{h\,eff} = (T_h + T_{e\,TX\,line\,1})G_{a\,TX\,line\,1}G_{a\,ATT} + T_{phys\,ATT}(1 - G_{a\,ATT}) \tag{5.11}$$

$$T_{c\,eff} = (T_c + T_{e\,TX\,line\,1})G_{a\,TX\,line\,1}G_{a\,ATT} + T_{phys\,ATT}(1 - G_{a\,ATT}) \tag{5.12}$$

[15] The measurements are carried out in Klerefontein from the 06 December to 10 December 2021. The measurement data is saved according to the dates they were taken.

$G_{a\,TX\,line\,1}$ and $T_{e\,TX\,line\,1}$ were previously determined in section 5.2.4 and $G_{a\,ATT}$ was determined in section 5.2.3. These values are identical and do not need to be determined again.

5.4.2 Finding T_h and T_c

For this measurement, T_c is measured as the temperature of the noise diode case. In this case it is measured using a thermocouple and automatically captured by the python script. This is an improvement over the previous method which relied on a multimeter thermocouple that the author manually recorded. The result is plotted in Figure 5.48.

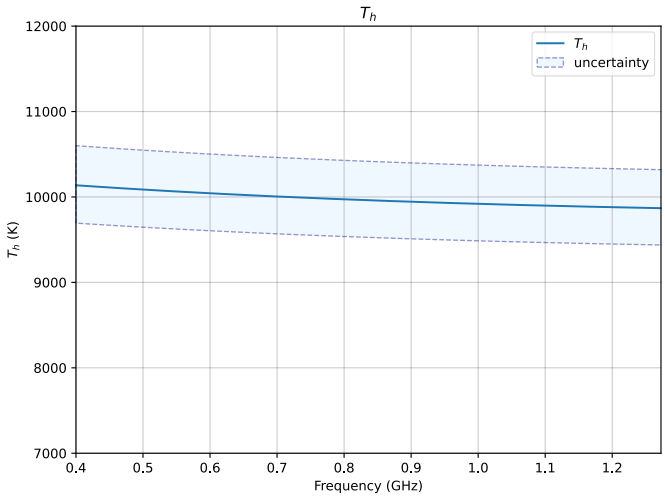

Figure 5.48. Plotted T_h values.

5.4.3 Finding $T_{phys\,ATT}$

Two measurements were carried out. The first measurement shown in Figure 5.49 was made without the braided copper conductor attached to the attenuator case. Figure 5.52 shows the temperature measured on the attenuator case was approximately 12 K higher than the temperature measured on the cold plate. Figure 5.50 clearly shows that there is an offset in the measured temperatures recorded for the two temperature sensors.

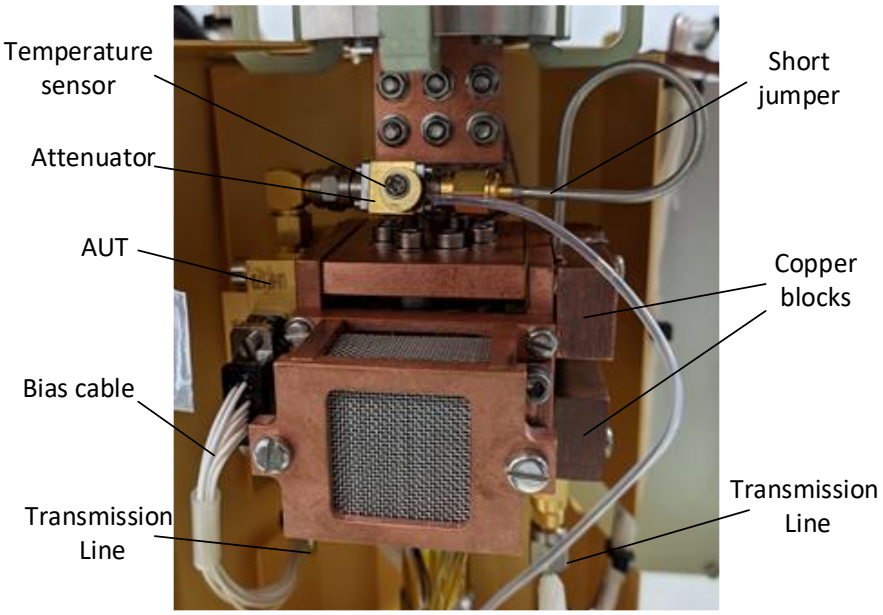

Figure 5.49. The attenuator installed without the braided copper conductor.

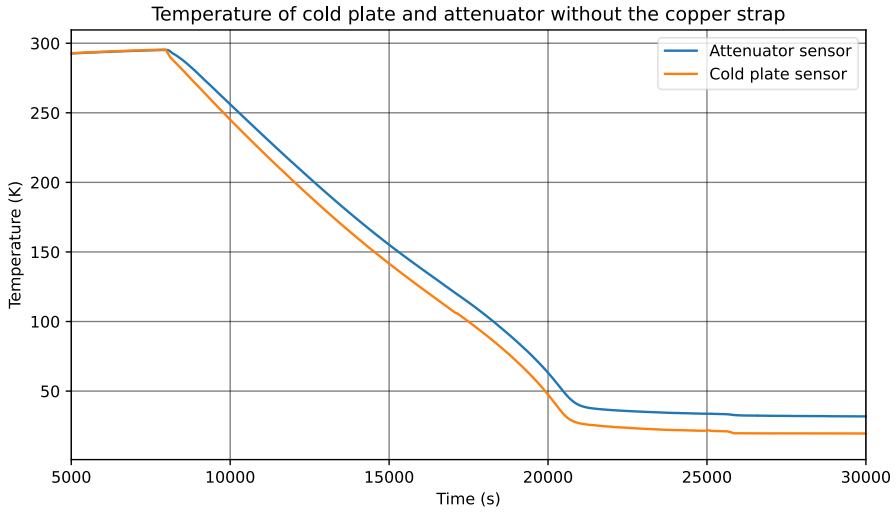

Figure 5.50. Plot of the recorded temperature of the attenuator sensor and the cold plate sensor without the braided copper thermal conductor.

The copper braided thermal conductor was added to connect the attenuator to the cold head as shown in Figure 5.51. Figure 5.52 shows that recorded temperature of the attenuator case is very close to the cold head temperature.

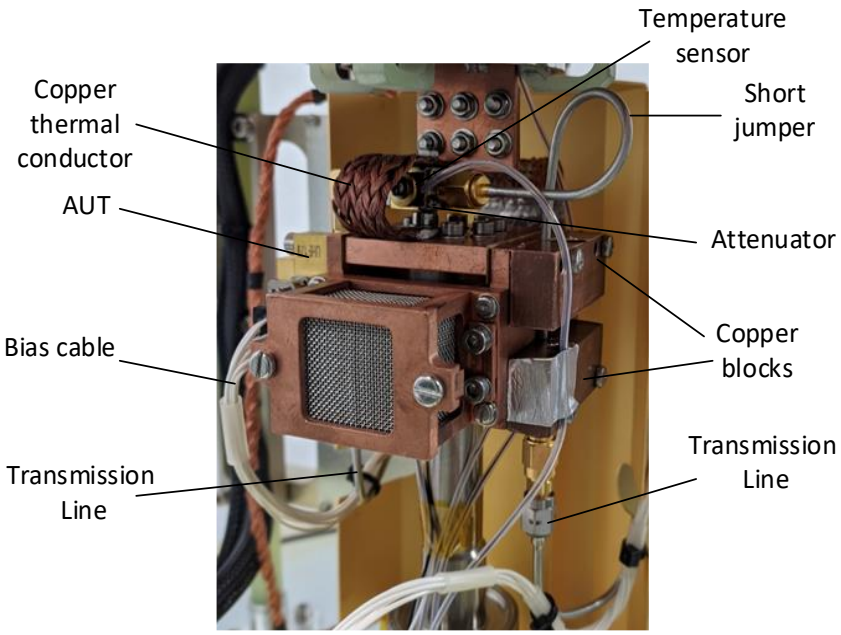

Figure 5.51. The addition of a copper thermal conductor.

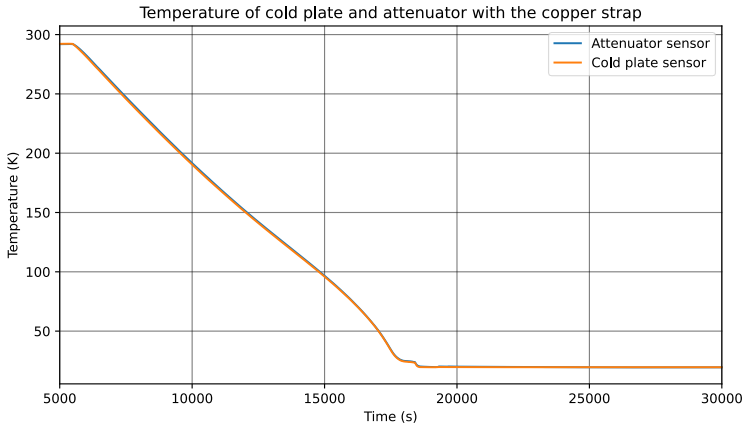

Figure 5.52. Plot of the recorded temperature of the attenuator sensor and the cold plate sensor after the addition of the copper thermal conductor. Note that both traces are almost identical and overlaid.

The difference in temperature between the cold plate and the attenuator case is shown in Figure 5.53. For the measurement without the strap attached to the attenuator case, the temperature difference appears to settle at 11.5 K. The source of this difference could be radiation loading from the 77 K heat shield and OMT or heat loading via the thermal sensor cable, however the most likely cause is thermal conduction through the centre conductor of the coaxial cable. If this is the case, then the strap that was attached to the case of the attenuator affectively ties the case of the attenuator and hence the temperature sensor to the cold head.

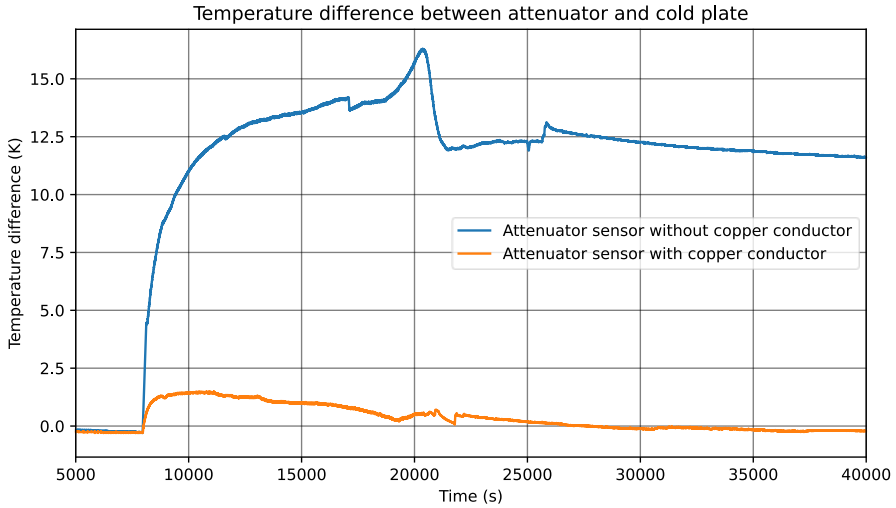

Figure 5.53. Plot of the difference between recorded temperature of the attenuator sensor and the cold plate sensor before and after the addition of the copper thermal conductor.

An interesting conclusion is that anchoring the attenuator case to the cold head via the copper strap effectively masks the effect of any heat conducted via the centre conductor. Conversely, leaving the attenuator case disconnected from the cold head reveals that there are heat loads acting on the attenuator, potentially via the centre conductor.

Another conclusion from Figure 5.53 is that the values are smaller than zero in some places. This implies that the reading from the temperature sensor located on the attenuator is 0.25 K colder than the reading from the temperature sensor located on the cold plate. This is not likely when the system is at room temperature. A more likely explanation is that this is due to the measurement error of the uncalibrated sensors.

5.4.4 Determining $T_{e\,cas}$ from a Y factor radiometer measurement

In this final step, the AUT is installed as shown in Figure 5.54 and the $T_{meas\,hot}$ and $T_{meas\,cold}$ are measured and used to find the Y-factor values. The temperature sensor attached to the cold attenuator is recorded and used as the $T_{phys\,ATT}$. The temperature sensor attached to the noise source is recorded and used to calculate the T_h value for this measurement.

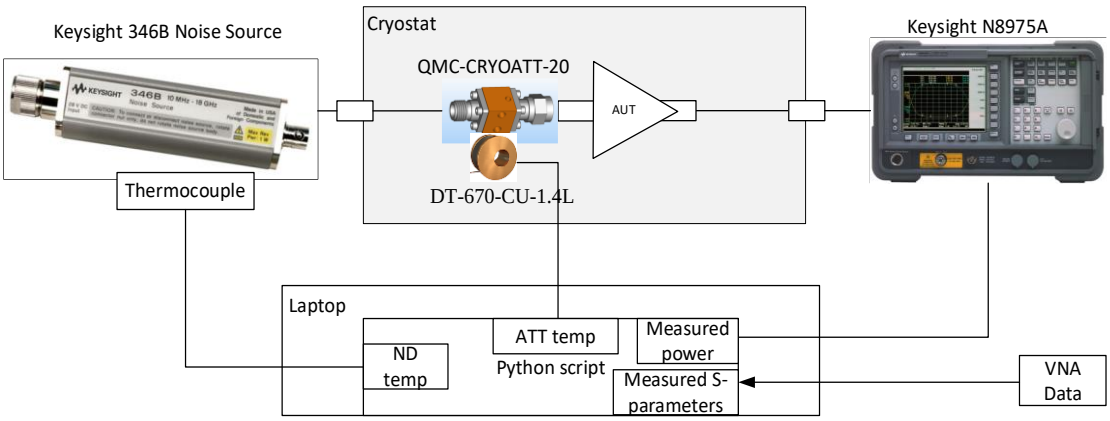

Figure 5.54. The final cold attenuator measurement block diagram.

Figure 5.55 shows the Y-factor based on the spectrum analyser measurements .This shows that even without a pre-amplifier and setting the 20 dB attenuation at the input of the noise figure analyser, there is a good ratio between the hot and cold measurements. Leffel and Daniel (2012) suggest that a good Y-factor ratio is 5 dB or a linear ratio of 3.16 [42].

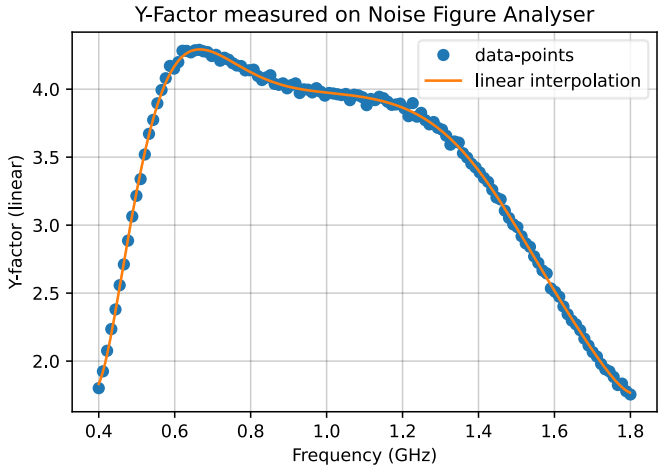

Figure 5.55. The cold attenuator measured Y-factor ratio.

5.4.5 Second stage effect removal

Once $T_{e\,cas}$ is calculated, the below equation is used to remove the second stage effect and determine $T_{e\,AUT}$.

$$T_{e\,AUT} = T_{e\,cas} - \frac{T_{e\,2nd\,stage}}{G_{a\,AUT}} \tag{5.13}$$

The $G_{a\ AUT}$ was determined in section 5.2.7 during measurement campaign 2. These values are identical and do not need to be determined again.

5.4.6 Equivalent noise temperature of the radiometer ($T_{e\ 2nd\ stage}$)

The noise figure analyser set to 20 dB attenuation with no external preamp for this measurement as shown in the block diagram of Figure 5.56. The result of the measurement is shown in Figure 5.57. The mismatch between the noise source and the noise figure analyser results in power being reflected and sets up a standing wave pattern that varies with frequency. The different reflection coefficients present at the noise source -on and -off states set up slightly different standing wave patterns. The resultant ripple over frequency after the Y-factor calculation is evident in the trace plotted in Figure 5.57.

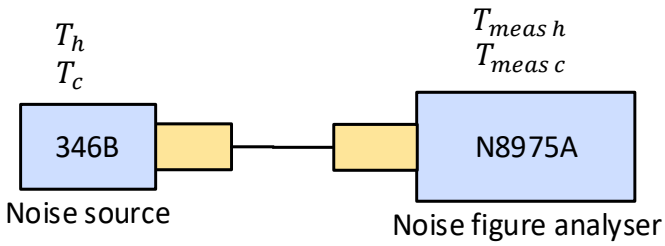

Figure 5.56. The second stage equivalent noise temperature measurement block diagram.

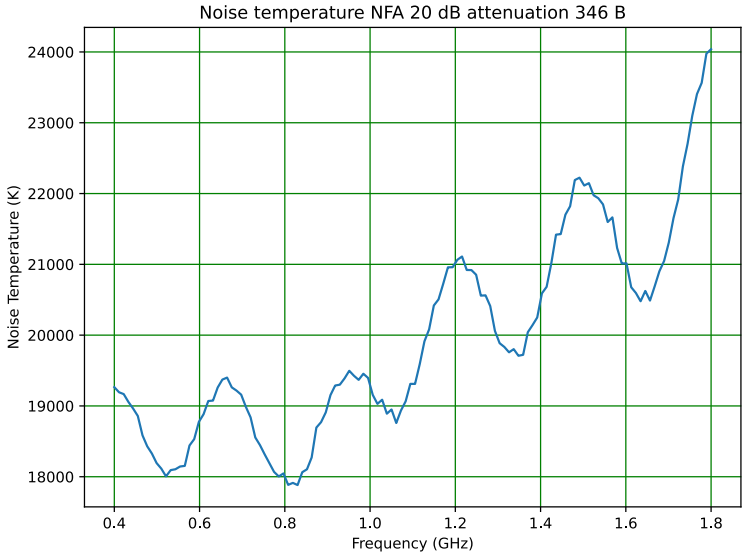

Figure 5.57. The measured equivalent noise temperature of the second stage.

5.4.7 Measurement campaign 3 results, conclusions and suggestions

Shown below are the results with and without the thermal strap attached for comparison. The blue trace in Figure 5.58 shows the effective noise temperature without the thermal strap attached to the attenuator. The physical temperature of the attenuator case was recorded as 30.82 K for this test. The orange trace in Figure 5.58 shows the effective noise temperature with the thermal strap attached. The physical temperature of the attenuator case was recorded as 19.27 for this test.

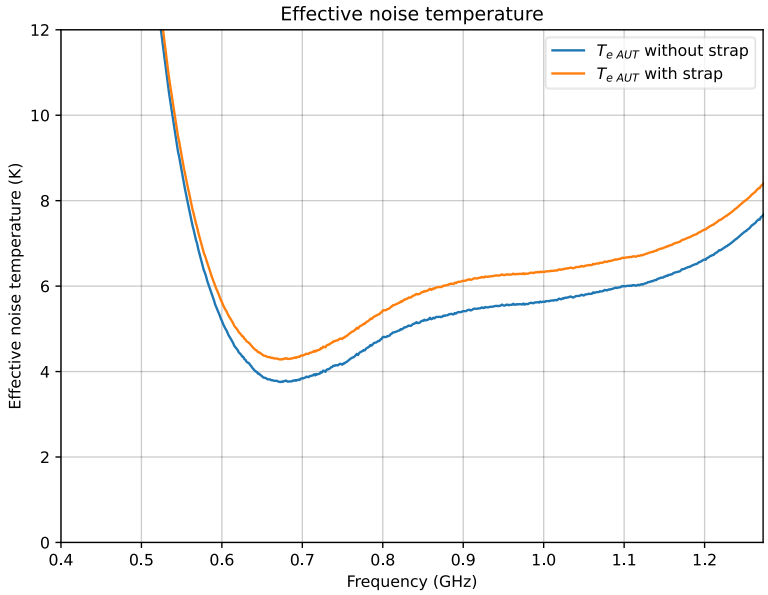

Figure 5.58. The equivalent noise temperature of the AUT using the cold attenuator measurement with and without the strap attached between the attenuator and the cold head.

Both results from measurement campaign 3 show a value 2 K lower than the values reported in measurement campaign 2, however this is still approximately 2 K higher than the value reported by the supplier.

This difference between measured data and supplier data is discussed in Chapter 6 in more detail, but may be due to the following points:

- The supplier data may be overly optimistic. There is the option to have an independent lab carry out a measurement as verification.
- The temperature of the attenuator is still not known to a high enough degree of accuracy due to a calibrated temperature sensor not being available.

- The temperature gradient across the attenuator is still a problem due to the heat carried by the centre conductor.

Chapter 6

Conclusions and suggestions

The importance of ultra-low-noise amplifiers was explained within the context of radio astronomy and the MeerKAT project. Terms relevant to the discussion of noise and measurement of noise in radio frequency circuits were presented in chapters 1 and 2.

The classic and corrected Y-factor measurement methods were discussed, along with the drawbacks with using this method. The cold source measurement method was also investigated but rejected due to the amount of hot cold cycles required and the lack of a well characterised thermally stabilised radiometer being available. The cold source measurement relies on a single thermal noise source measurement, thus the radiometer carrying out the measurement needs to have excellent absolute accuracy and long-term stability between calibration intervals.

The cold attenuator method was selected due to a few advantages. The use of a 20 dB attenuator addresses the mismatch error at the input of the AUT. Additionally, the uncertainty in the determination of the noise contribution and loss of the input transmission line becomes almost insignificant to the total measurement uncertainty due to the comparative insertion loss of the attenuator. The attenuator helps to mitigate the error due to the different impedance between the on- and off- state of the noise source. The mismatch error at the output of the AUT is minimised by selecting an input attenuation on the noise figure analyser or spectrum analyser that presents a greater than 20 dB return loss.

The cold attenuator method uses both an active noise source and a thermal noise source. The radiometer used in the measurement does not require the same excellent absolute accuracy compared to the cold source method. The stability is required only over the measurement sweeps, which may be two to three minutes.

The objective of examining the available literature and finding a suitable method was successful and resulted in the successful second objective of designing and building the T_e measurement system. The existing MeerKAT UHF-band cryostat was adapted and used as the test system.

The final objective of performing measurements on a cryogenic LNA and interpreting the results was also successfully carried out with the major findings and suggestions presented in section 6.1.

Additional to the original set of objectives, a thermal study was carried out which resulted in an improvement of the measurement method. However, the challenge of lowering the measurement uncertainty to below 1 K is still to be addressed and some suggestions for improvement are given in section 6.1.

The limitations that were encountered included the DT-670-CU-1.4L calibrated temperature sensor not being available at the time of measurement. Referring to Figure 4.18 this could contribute 0.6 K offset to the final measurement when using the 346 B noise source. The use of the existing cryostat meant limited space for the attenuator and no ideal mounting of the attenuator and no good way to anchor the coaxial cable. A purpose-built solution can simplify the thermal anchoring of the coaxial cables and mounting of the attenuator.

The results presented in this work represent major advances in the measurement of ultra-low-noise amplifiers within the context of the South African Radio Astronomy Observatory and the understanding gained through this process will be vital to the building of a cryogenic LNA test facility.

Referring to Figure 6.1 for an overview of the measurement results for measurement campaign 2 and measurement campaign 3. The first measurement using the helium cooled cryostat is shown in blue is the furthest from the manufacturer supplied data. The improved attenuator configuration measurement carried out in measurement campaign 3 without the copper strap shown as the orange is the closest to the manufacturer data. Finally, the green trace shows that the addition of the copper strap cooled the attenuator case, but resulted in a final equivalent noise temperature of the AUT further from the manufacturer data than without the copper strap.

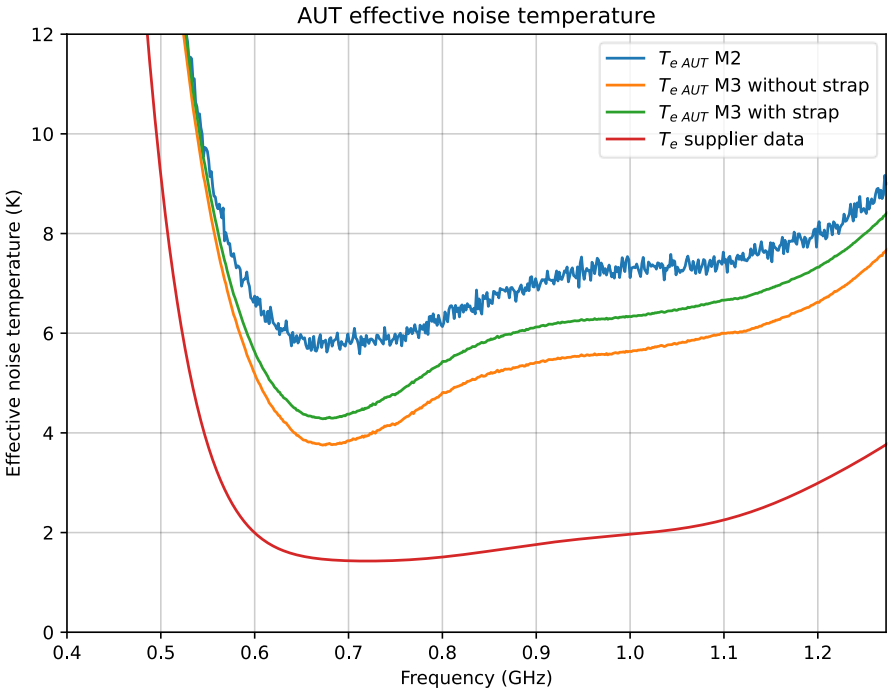

Figure 6.1. Comparison of 3 measurements with the supplier data

6.1 Suggestions for future work

Thermal gradient across the attenuator

Further examination of the thermal simulation heat path view shows that there is a lower thermal resistance at the transmission line inner conductor compared to the outer conductor. Referring to Figure 6.2, only the major heat conductors are shown. The heat flow is from the cryostat case to the cold head. The benefit of this analysis is a visual representation of the heat flow through the outer conductor and through the inner conductor of the coaxial cable. It also shows that most of the heat is flowing through the copper blocks, from the outer conductor to the cold plate and then from the cold plate to the cold head. Unfortunately the utility of this simulation is limited due to the fact that simplifications were made in order to model the inside of the attenuator and the SMA connector interfaces.

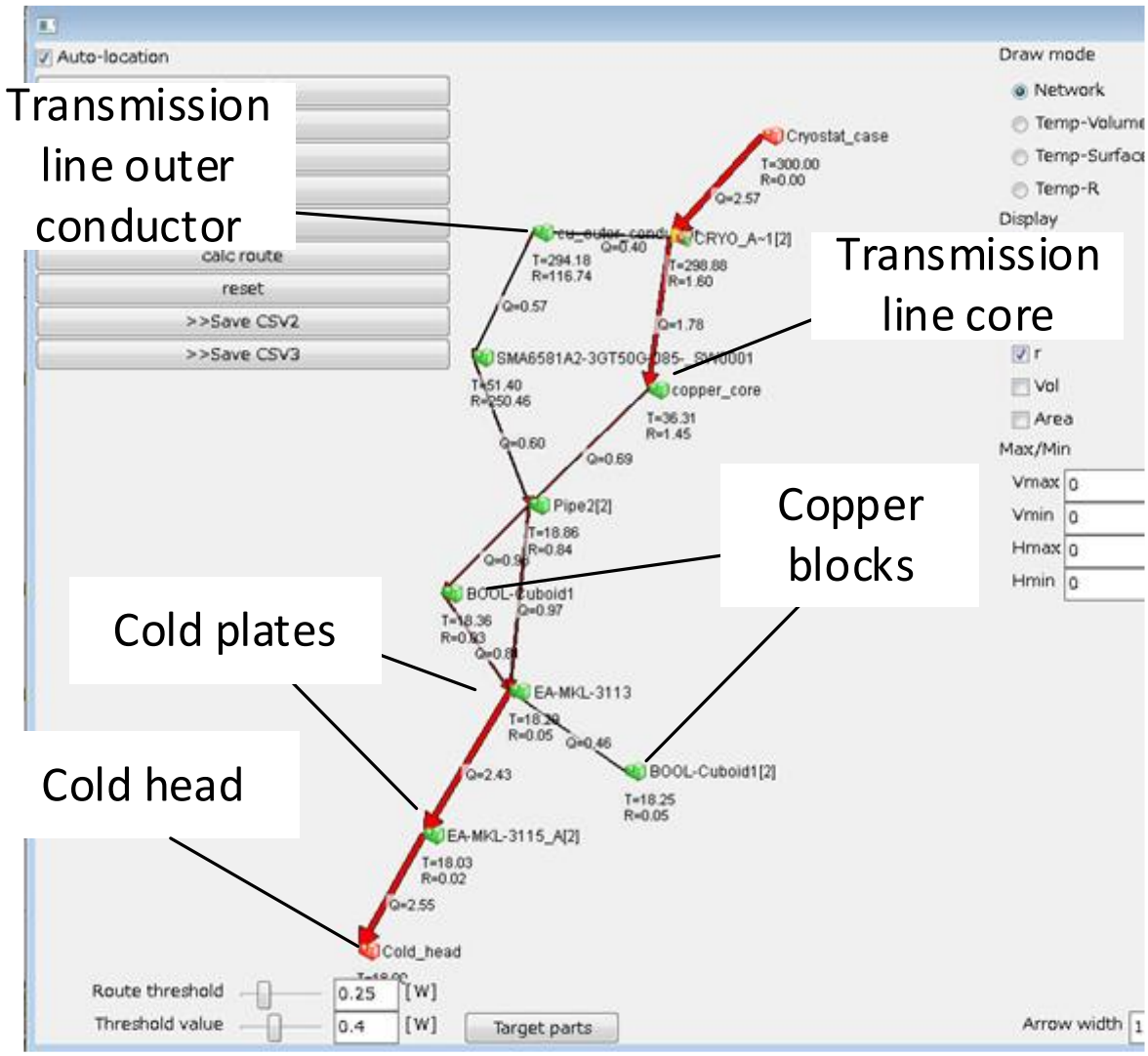

Figure 6.2. The thermal simulation heat path view showing a significant amount of heat flows through the transmission line centre conductor.

Gallego, López-Fernández and Diez (2009) described the problem of excess thermal gradient across the attenuator. Referring to Figure 6.3, the attenuator is thermally anchored using a machined copper block that makes contact with the attenuator body on all sides. It is difficult to accurately measure the physical temperature of the resistive element in the attenuator and a 1 K error in the measurement of the resistive element physical temperature translates directly to a 1 K error in the measured AUT equivalent noise temperature [62].

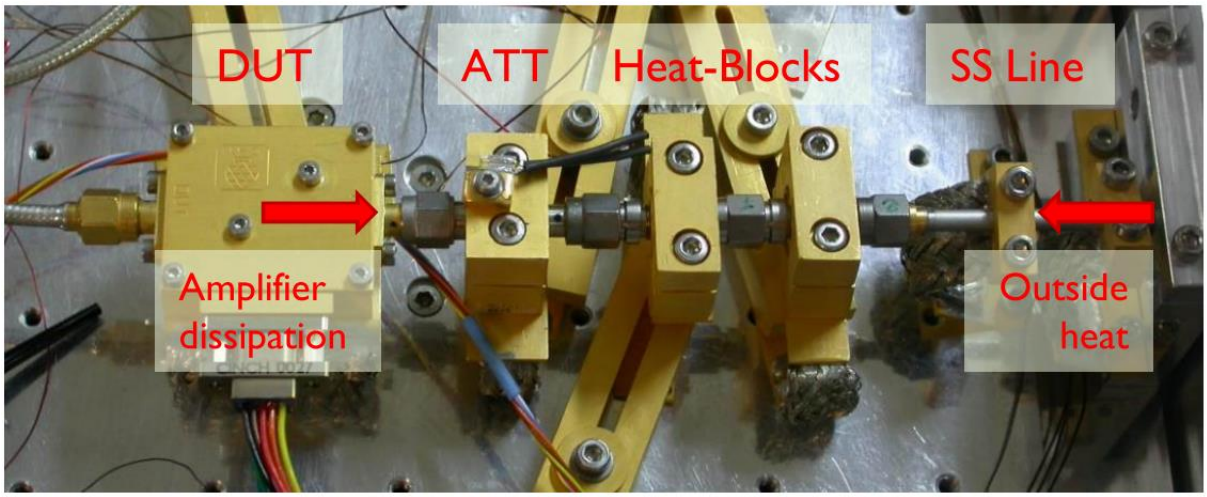

Figure 6.3. Two heat-blocks employed inside a test cryostat at Yebes [62].

The use of heat-blocks

Gallego, López-Fernández and Diez (2009) described the problem of heat transfer through the inner coaxial conductor. They have developed a solution to deal with this issue, called a "heat-block". Shown in Figure 6.4, the heat-block is a cascade of two 2.92 mm (K-type) female sparkplug launcher transitions with a Wiltron K102F or Wiltron K100 glass bead sandwiched in-between. The thermal resistance of the glass bead is much higher than the copper centre conductor. As shown in Figure 6.3, Gallego, López-Fernández and Diez (2009) suggest using two heat-blocks in series provides sufficient thermal isolation between the centre conductor and the attenuator [62].

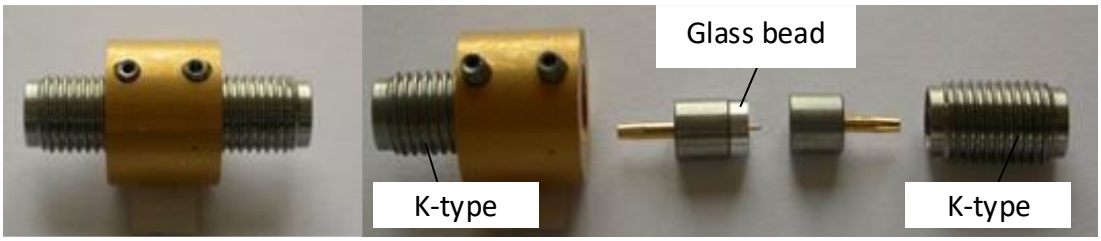

Figure 6.4. The heat-blocks employed inside a test cryostat isolating the attenuator from the heat carried by the centre conductor [62].

In future, the use of heat-blocks will increase the certainty of the temperature measurement of the attenuator resistive element.

Heat transfer between the AUT and the attenuator

Gallego, López-Fernández and Diez (2009) also suggest that heat is very efficiently transferred from the amplifier under test to the attenuator. Excess power dissipation or insufficient thermal contact between the amplifier body and the cold plate results in a noticeable difference in the measured noise temperature [62].

Self-heating of the noise source

The noise source temperature increases when the diode is biased, therefore leaving the noise source powered for extended periods of time will cause the T_h to change. Instead, the noise source should be switched on, then off for each frequency point or each sweep, provided that the sweep time is not too long. Performing consecutive sweeps with the noise source switched on and then consecutive sweeps with the noise source switched off causes temperature changes of five or more degrees C.

Correspondence with an expert in the field

A summary of the results and conclusions were sent to an expert in the field Juan Daniel Gallego at the Yebes observatory and he advised the following:

- The determination of the noise of cryogenic amplifiers with good accuracy is not an easy task.
- The cold attenuator method is very convenient for using commercial noise figure meters however, the temperature of the attenuator needs to be accurately known.
- Often, the attenuation element is hotter than the attenuator body due to the heat conducted by the inner coaxial cables. They have tried different solutions over the years, and currently use a custom designed attenuator that is immune to this effect.
- They previously used the "heat block" between the attenuator and the transmission line when using commercial coaxial attenuators.

His recommendation was to try to improve the thermal isolation of the attenuator from the centre conductor of the transmission line using a "heat block" or similar solution.

Additionally, he advised that they have found in the past that the supplier data may be too optimistic and offered an independent measurement to verify the data.

The email is contained in Appendix D - for reference.

Bibliography

[1] K. G. Jansky, “Technical papers: Minimum noise levels obtained on shortwave radio receiving systems,” *Proceedings of the Institute of Radio Engineers*, vol. 25, no. 12, pp. 1648–1651, 1937, doi: 10.1109/JRPROC.1937.228864.

[2] K. G. JANSKY, “Radio Waves from Outside the Solar System,” *Nature*, vol. 132, no. 3323, pp. 66–66, Jul. 1933, doi: 10.1038/132066a0.

[3] K. G. Jansky, “Electrical Disturbances Apparently of Extraterrestrial Origin,” *Proceedings of the IRE*, vol. 21, no. 10, pp. 1387–1398, Oct. 1933, doi: 10.1109/JRPROC.1933.227458.

[4] G. Reber, “Cosmic Static,” *Proceedings of the IRE*, vol. 30, no. 8, pp. 367–378, 1942, doi: 10.1109/JRPROC.1942.231700.

[5] H. C. Van De Hulst, “Origin of the Radio Waves from Space,” in *Classics in Radio Astronomy*, Dordrecht: Springer Netherlands, 1982, pp. 302–316.

[6] J. D. Kraus, M. Tiuri, A. V. Räisänen, and T. D. Carr, *RADIO ASTRONOMY*, 2nd ed. Durham: Cygnus-Quasar Books, 1986.

[7] Haade, “Electromagnetic spectrum and atmospheric opacity,” 2007. https://commons.wikimedia.org/wiki/File:AtmosphereEMSpectrum.png (accessed Dec. 28, 2021).

[8] New Technology Development Division, “Millimeter Wave Propagation: Spectrum Management Implications,” Washington, 1997. [Online]. Available: https://transition.fcc.gov/Bureaus/Engineering_Technology/Documents/bulletins/oet70/oet70a.pdf.

[9] ALMA observatory, “How ALMA works, Technologis, Receivers.” https://www.almaobservatory.org/en/about-alma/how-alma-works/technologies/receivers/ (accessed Feb. 06, 2022).

[10] Wikipedia, “Green Bank Telescope,” *Wikipedia*. https://en.wikipedia.org/wiki/Green_Bank_Telescope (accessed Feb. 06, 2022).

[11] R. S. Booth and J. L. Jonas, “An Overview of the MeerKAT Project,” *African Skies*, no. 16, pp. 101–104, 2012, [Online]. Available: http://articles.adsabs.harvard.edu/cgi-bin/nph-iarticle_query?2012AfrSk..16..101B&defaultprint=YES&filetype=.pdf.

[12] Wikipedia, “Carnarvon, Northern Cape.” https://en.wikipedia.org/wiki/Carnarvon%2C_Northern_Cape (accessed Feb. 06, 2022).

[13] Wikipedia, “Karl G. Jansky Very Large Array,” *Wikipedia*. https://en.wikipedia.org/wiki/Very_Large_Array (accessed Feb. 06, 2022).

[14] Hartrao, “15m XDM Radio Telescope.” http://www.hartrao.ac.za/xdm/ (accessed Jan. 02, 2022).

[15] SARAO, “KAT-7 Seven-dish MeerKAT precursor array.” https://www.sarao.ac.za/science/kat-7/ (accessed Jan. 02, 2022).

[16] J. L. Jonas, “The MeerKAT radio telescope,” in *Proceedings of Science*, 2016, pp. 25–27, doi: 10.22323/1.277.0001.

[17] South African Radio Astronomy Observatory (SARAO), “MeerKAT radio telescope gallery,” 2018. https://www.sarao.ac.za/gallery/meerkat/ (accessed Dec. 29, 2021).

[18] S. Okwit, “An Historical View of the Evolution of Low-Noise Concepts and Techniques,” *IEEE Transactions on Microwave Theory and Techniques*, vol. 32, no. 9, pp. 1068–1082, 1984, doi: 10.1109/TMTT.1984.1132818.

[19] J. B. Johnson, “Thermal agitation of electricity in conductors,” *Physical Review*, vol. 32, no. 1, pp. 97–109, 1928, doi: 10.1103/PhysRev.32.97.

[20] H. Nyquist, “Thermal agitation of electric charge in conductors,” *Physical Review*, vol. 32, no. 1, pp. 110–113, 1928, doi: 10.1103/PhysRev.32.110.

[21] D. M. Pozar, *Microwave engineering*, Fourth. Wiley, 2011.

[22] C. T. Stelzried, “Microwave Thermal Noise Standards,” *IEEE Transactions on Microwave Theory and Techniques*, vol. 16, no. 9, pp. 646–655, 1968, doi: 10.1109/TMTT.1968.1126767.

[23] J. Randa, E. Gerecht, D. Gu, and R. L. Billinger, “Precision measurement method for cryogenic amplifier noise temperatures below 5 K,” *IEEE Transactions on Microwave Theory and Techniques*, vol. 54, no. 3, pp. 1180–1188, 2006, doi: 10.1109/TMTT.2005.864107.

[24] D. Vondran, “Noise figure measurement: Corrections related to match and gain,” *Microwave Journal*, vol. 42, no. 3, pp. 22–38, 1999.

[25] E. W. Strid, “Measurement of Losses in Noise-Matching Networks,” *IEEE Transactions on Microwave Theory and Techniques*, vol. 29, no. 3, pp. 247–252, 1981, doi: 10.1109/TMTT.1981.1130335.

[26] T. Y. Otoshi, “The Effect of Mismatched Components on Microwave Noise-Temperature Calibrations,” *IEEE Transactions on Microwave Theory and Techniques*, vol. 17, no. 3. p. 174, 1969, doi: 10.1109/TMTT.1969.1126925.

[27] J.-M. Collantes, R. D. Pollard, and M. Sayed, “Effects of dut mismatch on the noise figure characterization: a comparative analysis of two y-factor techniques,” *IEEE Transactions on Instrumentation and Measurement*, vol. 51, no. 6, pp. 1150–1156, Dec. 2002, doi: 10.1109/TIM.2002.808015.

[28] H. T. Friis, “Noise Figure of Radio Receivers,” *Proceedings of I.R.E.*, vol. 34, no. 9,

pp. 419–422, 1944.

[29] Wikipedia, “Wien’s displacement law.” https://en.wikipedia.org/wiki/Wien’s_displacement_law (accessed Jan. 12, 2022).

[30] A. Tzioumis, *Handbook on Radio Astronomy*, 3rd ed. Geneva: International Telecommunications Union, 2013.

[31] I. Theron, “Current L-Band Radio Astronomy Conventional Receiver State of the Art Karoo Array Telescope,” 2016. [Online]. Available: https://www.astron.nl/midaa2016/documents/midaa2016_Theron.pdf.

[32] C. M. Reporter, “Company continues to provide world-class solutions,” *Creamer Media’s Engineering News*, 2020.

[33] L. Green, “The Fundamental Radiometer Equation,” no. January 2013, 2020, [Online]. Available: https://www.researchgate.net/publication/346967408.

[34] “MeerKAT Spec and Schedule,” 2016. http://public.ska.ac.za/meerkat/meerkat-schedule (accessed Nov. 14, 2021).

[35] S. Goedhart and V. Krishnan, “MeerKAT specifications,” 2020. https://skaafrica.atlassian.net/wiki/spaces/ESDKB/pages/277315585/MeerKAT+specifications (accessed Nov. 14, 2021).

[36] T. Küsel, “SKA & MeerKAT System Overview.” http://www.aardvarkaoc.co.za/wp-content/Proceedings/201505 Aardvark AOC/Thomas.pdf (accessed Dec. 29, 2021).

[37] N. Jiang, D. Garcia, P. Niranjanan, M. Halman, and I. Wevers, “Extremely low noise UHF-band amplifiers for square kilometer array,” *Millimeter, Submillimeter, and Far-Infrared Detectors and Instrumentation for Astronomy VIII*, vol. 9914, p. 991420, 2016, doi: 10.1117/12.2232154.

[38] N. Jiang, L. B. G. Knee, D. Garcia, P. Niranjanan, M. Halman, and I. Wevers, “Cryogenic L-band GaAs HEMT LNA for the Square Kilometer Array,” *Proceedings - ANTEM 2018: 2018 18th International Symposium on Antenna Technology and Applied Electromagnetics*, vol. 2018-Augus, pp. 1–4, 2018, doi: 10.1109/ANTEM.2018.8572988.

[39] M. A. McCulloch *et al.*, “Dependence of noise temperature on physical temperature for cryogenic low-noise amplifiers,” *Journal of Astronomical Telescopes, Instruments, and Systems*, vol. 3, no. 1, p. 014003, 2017, doi: 10.1117/1.jatis.3.1.014003.

[40] D. Schalk and V. D. M. Prinsloo, “Characterisation of L-band Differential Low Noise Amplifiers,” University of Stellenbosch, 2011.

[41] J. E. Fernandez, “A Noise-Temperature Measurement System Using a Cryogenic Attenuator,” *The Telecommunications and Mission Operations Progress Report*, vol. 42, no. 135, pp. 1–9, 1998, [Online]. Available:

https://ipnpr.jpl.nasa.gov/progress_report/42-135/135F.pdf.

[42] M. Leffel and R. Daniel, “The Y Factor Technique for Noise Figure Measurements,” 2012. [Online]. Available: http://cdn.rohde-schwarz.com/pws/dl_downloads/dl_application/application_notes/1ma178/1MA178_1E_the_Y_factor_technique.pdf.

[43] J. C. Bardin, “Silicon-Germanium Heterojunction Bipolar Transistors For Extremely Low-Noise Applications,” California Institute of Technology, 2009.

[44] J. Randa, “Amplifier and Transistor Noise Parameter Measurements,” in *Wiley Encyclopedia of Electrical and Electronics Engineering*, no. 1, John Wiley and Sons, Inc., 2014, p. 38.

[45] R. Adler, R. S. Enelbrecht, S. W. Harrison, H. A. Haus, M. T. Lebenbaum, and W. W. Mumford, “Description of the Noise Performance of Amplifiers and Receiving Systems,” *Proceedings of the IEEE*, pp. 436–442, 1963.

[46] L. Pradell, A. Comeron, and A. Ramirez, “General analysis of errors in noise measurement systems,” in *Conference Proceedings - European Microwave Conference*, 1988, no. 18, pp. 924–929, doi: 10.1109/euma.1988.333927.

[47] L. F. Tiemeijer, R. J. Havens, R. de Kort, and A. J. Scholten, “Improved Y-factor method for wide-band on-wafer noise-parameter measurements,” *IEEE Transactions on Microwave Theory and Techniques*, vol. 53, no. 9, pp. 2917–2925, Sep. 2005, doi: 10.1109/TMTT.2005.854243.

[48] D. Gu, J. Randa, R. Billinger, and D. K. Walker, “A verification method for noise-temperature measurements on cryogenic low-noise amplifiers,” *CPEM Digest (Conference on Precision Electromagnetic Measurements)*, pp. 32–33, 2012, doi: 10.1109/CPEM.2012.6250644.

[49] D. Gu, J. Randa, R. Billinger, and D. K. Walker, “Measurement and uncertainty analysis of a cryogenic low-noise amplifier with noise temperature below 2 K,” *Radio Science*, vol. 48, no. 3, pp. 344–351, 2013, doi: 10.1002/rds.20039.

[50] S. Simbierowicz *et al.*, “Characterizing cryogenic amplifiers with a matched temperature-variable noise source,” *Review of Scientific Instruments*, vol. 92, no. 3, pp. 1–11, 2021, doi: 10.1063/5.0028951.

[51] J. Schleeh, N. Wadefalk, P. A. Nilsson, and J. Grahn, “10 K room temperature LNA for SKA band 1,” *IEEE MTT-S International Microwave Symposium Digest*, vol. 2016-Augus, pp. 1–4, 2016, doi: 10.1109/MWSYM.2016.7540344.

[52] D. S. Russell, “Technology advances for radio astronomy,” California Institute of Technology, 2013.

[53] H. F. Hsiao, C. H. Tu, D. C. Chang, and Y. Z. Juang, “Noise figure verification using cold-Source and Y-factor technique for amplifier and down-converted mixer,” 2014.

[54] A. Paech, S. Neidhardt, and M. Beer, “Noise Figure Measurement without a Noise Source on a Vector Network Analyzer,” 2010. [Online]. Available: https://www.rohde-schwarz.com/in/applications/noise-figure-measurement-without-a-noise-source-on-a-vector-network-analyzer-application-note_56280-15830.html.

[55] Agilent Technologies, “High-Accuracy Noise Figure Measurements Using the PNA-X Series Network Analyzer.” p. 60, 2010, [Online]. Available: cp.literature.agilent.com/litweb/pdf/5990-5800EN.pdf.

[56] M. Garelli, A. Ferrero, and S. Bonino, “A complete noise- and scattering-parameters test-set,” in *IEEE Transactions on Microwave Theory and Techniques*, 2009, vol. 57, no. 1, pp. 716–724, doi: 10.1109/TMTT.2009.2013315.

[57] S. W. Chang, J. Aumentado, W. T. Wong, and J. C. Bardin, “Noise measurement of cryogenic low noise amplifiers using a tunnel-junction shot-noise source,” *IEEE MTT-S International Microwave Symposium Digest*, vol. 2016-Augus, pp. 1–4, 2016, doi: 10.1109/MWSYM.2016.7538226.

[58] Noisecom, “Cold Attenuator Noise Measurements on Cryogenic LNAs,” *Noisecom*, 2013. https://noisecom.com/Portals/0/Applications/Cryogenic LNAs_411.pdf (accessed Nov. 04, 2021).

[59] J. D. Gallego-Puyol and M. W. Pospieszalski, “ACCURACY OF NOISE TEMPERATURE MEASUREMENT OF CRYOGENIC AMPLIFIERS,” 1991.

[60] J. L. C. de Diego, “Cryogenic Technology in the Microwave Engineering: Application to MIC and MMIC Very Low Noise Amplifier Design,” UNIVERSIDAD DE CANTABRIA, 2010.

[61] A. Sheldon, L. Belostotski, H. Mani, C. E. Groppi, and K. F. Warnick, “Cryogenic Noise-Parameter Measurements: Recent Research and a Fully Automated Measurement Application,” *IEEE Microwave Magazine*, vol. 22, no. 8, pp. 52–64, 2021, doi: 10.1109/MMM.2021.3078027.

[62] J. D. Gallego, I. López-fernández, and C. Diez, “A Measurement Test Set for ALMA Band 9 Amplifiers Introduction System description Noise measurements Calibrations Lessons learned after many measurements.” Centro Astronómico de Yebes, OAN (Spain), Gothenburg, 2009, [Online]. Available: https://icts-yebes.oan.es/amplifiers/doc/recent_presentations/RADIONET Low Noise Workshop Goteborg 06-2009 Measurement Test Set for ALMA band 9 Amplifiers.pdf.

[63] F. Molina, “Noise Figure measurement with Spectrum analyzer and Vector Network Analyzer,” 2019.

[64] Keysight, “SNS Series Noise Sources 10 MHz to 26.5 GHz (N4000A, N4001A, N4002A) Technical Overview,” *Keysight Technologies*, 2020. https://www.keysight.com/zz/en/assets/7018-01001/technical-overviews/5988-

0081.pdf (accessed Nov. 03, 2021).

[65] W. E. Pastori, “Applications of the Maury Noise Calibration Systems,” 2021.

[66] H. Liu and S. Weinreb, “Ultra-low loss lumped element cryogenic coolable high pass filter and cryogenic measurement method,” *Microwave and Optical Technology Letters*, vol. 59, no. 9, pp. 2229–2235, 2017, doi: 10.1002/mop.30718.

[67] S. Montazeri and J. C. Bardin, “A 2–4 GHz Silicon Germanium Cryogenic Low Noise Amplifier MMIC,” in *2018 IEEE/MTT-S International Microwave Symposium - IMS*, Jun. 2018, vol. 2018-June, pp. 1487–1490, doi: 10.1109/MWSYM.2018.8439235.

[68] D. Russell and S. Weinreb, “Low-power very low-noise cryogenic sige if amplifiers for terahertz mixer receivers,” *IEEE Transactions on Microwave Theory and Techniques*, vol. 60, no. 6 PART 1, pp. 1641–1648, 2012, doi: 10.1109/TMTT.2012.2190744.

[69] A. H. Akgiray *et al.*, “Noise measurements of discrete HEMT transistors and application to wideband very low-noise amplifiers,” *IEEE Transactions on Microwave Theory and Techniques*, vol. 61, no. 9, pp. 3285–3297, 2013, doi: 10.1109/TMTT.2013.2273757.

[70] J. L. Cano and E. Artal, “Cryogenic technology applied to microwave engineering,” *Microwave Journal*, vol. 52, pp. 70–80, 2009, Accessed: Jun. 25, 2021. [Online]. Available: https://www.microwavejournal.com/articles/8859-cryogenic-technology-applied-to-microwave-engineering.

[71] F. Jiang, S. Claude, and D. Garcia, “Hybrid cryogenic low noise amplifier for the MeetKAT array,” *Proceedings - ANTEM 2014: 2014 16th International Symposium on Antenna Technology and Applied Electromagnetics*, pp. 1–2, 2014, doi: 10.1109/ANTEM.2014.6887699.

[72] S. Weinreb, J. C. Bardin, and H. Mani, “Design of cryogenic SiGe low-noise amplifiers,” *IEEE Transactions on Microwave Theory and Techniques*, vol. 55, no. 11, pp. 2306–2312, 2007, doi: 10.1109/TMTT.2007.907729.

[73] J. L. Cano, N. Wadefalk, and J. D. Gallego-Puyol, “Ultra-wideband chip attenuator for precise noise measurements at cryogenic temperatures,” *IEEE Transactions on Microwave Theory and Techniques*, vol. 58, no. 9, pp. 2504–2510, 2010, doi: 10.1109/TMTT.2010.2058276.

[74] I. L. Fernández, “YCF 6 4-8 GHz AMPLIFIER REPORT,” Guadalajara, 2002.

[75] Oxford Cryosystems, “Coldstar Cryocoolers,” 2018. https://www.oxcryo.com/sites/default/files/2018-10/coolstar_brochure_k450.pdf (accessed Mar. 05, 2022).

[76] Y. S. and A. S. Davood Domairry Ganji, *Nonlinear Systems in Heat Transfer*. Elsevier, 2018.

[77] Times Microwave Systems, “Silicone Dioxide Coaxial Cable Assemblies,” 2019. https://www.timesmicrowave.com/DataSheets/Categories/SiO2.pdf (accessed Mar. 06, 2022).

[78] M. Winkler, “Optimizing Microwave Signal Transmissions In Extreme Cryogenic Environments,” Wallingford, 2009. [Online]. Available: https://www.timesmicrowave.com/DataSheets/Literature/Optimizing Microwave Signal Transmissions.pdf.

[79] Maury Microwave, “Noise Calibration Systems and Accessories.” https://www.maurymw.com/Precision/Noise_Calibration_Systems_Accessories.php (accessed Jan. 26, 2022).

[80] A. Cobin, “Thermalized Low Noise Cryogenic Attenuators,” 2021. https://quantummicrowave.com/wp-content/uploads/2020/03/QMC-CRYOATT-20.pdf (accessed Jan. 31, 2022).

[81] Lakeshore cryotronics, “Silicon Diode Sensor Packages and Mounting Adapters,” 2019. https://www.lakeshore.com/packaging/packagessi (accessed Mar. 20, 2022).

[82] Lake Shore Cryogenics inc, “DT-670 Silicon Diode Specifications,” 2019. https://www.lakeshore.com/products/categories/specification/temperature-products/cryogenic-temperature-sensors/dt-670-silicon-diodes (accessed Feb. 26, 2022).

[83] P. Bradly and R. Radebaugh, *Properties of Selected Materials at Cryogenic Temperatures*. Boca Raton, FL: CRC Press, 2013.

Appendix A - Python script for generating Planck blackbody radiation curves

The script can be downloaded at https://bit.ly/3WhbnUC.

Appendix B - Power Budget

boltzmanr 1.38E-23 J/K

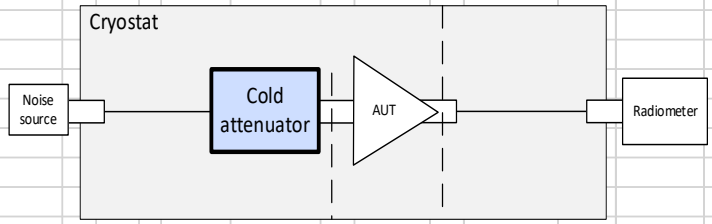

			Tc		Th	Ga Atten		Ga AUT		Ga Total		Th meas		Res BW	Pout		Pout	
ENR 4000A	5.5	dB	295	K	1341.7	-20	dB	46	dB	398.1072	W/W	534140	K	4000000	2.95E-11	W/W	-75.30	dBm
ENR 346B	15	dB	295	K	9623.7	-20	dB	46	dB	398.1072	W/W	3831272	K	4000000	2.11E-10	W/W	-66.75	dBm

Appendix C - Calculation of the Y-factor presented to the AUT

The Y-value presented to the AUT is calculated in order to use in the uncertainty equation. Because there are no measured values, equation (3.25) cannot be used.

The following values are used:

- $T_{e\,AUT}$ = 1 K
- $T_0 = 290\ K$
- $T_c = 18\ K$
- $G_{i\,ATT} = -20dB$

Table 6.1. Cold attenuator calculation to determine the Y-factor value.

ENR	*Th*	*Tc*	L-pad dB	L-pad ratio	*Th eff*	*Tc eff*	*Y*
5	1207.061	290	20	100	29.89	20.72	1.42
10	3190	290	20	100	49.72	20.72	2.33
15	9460.605	290	20	100	112.42	20.72	5.22

20	29290	290	20	100	310.72	20.72	14.35
25	91996.05	290	20	100	937.78	20.72	43.22
30	290290	290	20	100	2920.72	20.72	134.51

T_h is calculated using equation (4.2).

$T_{h\,eff}$ is calculated using equation (3.22).

$T_{c\,eff}$ is calculated using equation (3.23).

The Y value is calculation in this case by the equation: $\frac{T_{e\,AUT}+T_{h\,eff}}{T_{e\,AUT}+T_{c\,eff}}$ instead of the usual equation (3.25).

Appendix D - Email correspondence with Juan Daniel Gallego from Yebes observatory

Juan Daniel Gallego Apr 28, 2022, 10:34 AM

to me

Hi Wesley,

Sorry for the delay in answering. These days I have been immersed in a CDR for ALMA band 2.

About your measurements, as you well know, the determination of the noise of cryogenic amplifiers with good accuracy is not an easy task. The cold attenuator method which you are using very convenient for using commercial noise figure meters although it is not problem free. The main practical difficulties are a) the temperature of the attenuator needs to be accurately know and b) you have to determine the equivalent ENR of your setup, including all cables and transitions (their loss may change when cooling!).

Our experience is, as you pointed out, that in many cases the inside part of the attenuator is hotter than the body due to the heat conducted by the inner coaxial cables (which are usually good thermal conductors to avoid excessive electrical loss). We have tried to use different solutions for this over the years. Now we have a specially designed attenuator based on a mGaAs MMIC built on a very thin

substrate which we believe is quite immune to heating by the inner coax. In the past, when using commercial coaxial attenuators, we introduced a “heat block” between the attenuator and the SS line. You can find a description and some details of that setup here (see pages 15-18):

https://icts-yebes.oan.es/amplifiers/doc/recent_presentations/RADIONET%20Low%20Noise%20Workshop%20Goteborg%2006-2009%20Measurement%20Test%20Set%20for%20ALMA%20band%209%20Amplifiers.pdf

In your case, I would try first something similar to this “heat block” to see what happens. You can never discard that the original measurement from the manufacturer may be too optimistic. We have found many cases of that. If you ever want to compare with other independent measurement, there is the possibility of measuring one of your amplifiers in our lab in a setup with a precision heated load.

Other references which may be of interest related to this:

https://icts-yebes.oan.es/amplifiers/doc/recent_presentations/RADIONET%20Low%20Noise%20Workshop%20Goteborg%2006-2009%20Estimation%20of%20Uncertainty%20in%20Noise%20Measurements.pdf (about error estimation in cryogenic noise measurements)

https://ieeexplore.ieee.org/abstract/document/6365276 (description of a heated load for cryogenic noise measurements)

https://ieeexplore.ieee.org/document/5540248 (other “special” attenuator for cryogenic noise measurements)

If you have more questions, please let me know.

Regards,

Appendix E - Interpolation script for noise diode ENR values

```
# -*- coding: utf-8 -*-
"""
Created on Tue Mar 29 21:59:59 2022

@author: wnewton
"""

import numpy as np
import matplotlib.pyplot as plt
# ----------------------------------------------------------------------------#
f_start = 400e6  # Start frequency
f_stop = 1.8e9  # Stop frequency
numPoints = 1001  # Number of measurement points
freq_delta = (f_stop-f_start)/numPoints
# Get frequency data from Start_freq, Stop_Freq and Amount of Points
freq = np.arange(numPoints)*freq_delta + f_start
# Generate a numpy array for frequency data (Hz)
# %%


def interpolate(original_column1,
                original_column2,
                polynomial_degree,
                new_column1_start,
                new_column1_stop,
                pts):
    Interpolate_V = np.polyfit(original_column1,
                               original_column2,
                               polynomial_degree)
    # returns a vector for the interpolation
    INT_PN = np.poly1d(Interpolate_V)
    # Generate a polynomial from the interpolation vector
    freq = np.linspace(new_column1_start, new_column1_stop, pts)
    # generate frequency array for plot
    INT_ARR = np.column_stack((freq, INT_PN(freq)))
    return INT_ARR

# %%
# Generate the ENR VS freq array for the 346B s/n:MY53400779


ENR_table_346b = np.array([[10e6, 15.33],
                           [100e6, 15.32],
                           [1e9, 14.99],
                           [2e9, 14.97],
                           [3e9, 14.89],
                           [4e9, 14.77],
                           [5e9, 14.74],
                           [6e9, 14.71],
                           [7e9, 14.60],
                           [8e9, 14.69],
                           [9e9, 14.72],
                           [10e9, 14.72],
                           [11e9, 14.78],
                           [12e9, 14.85],
```

```
                            [13e9, 14.82],
                            [14e9, 14.94],
                            [15e9, 15.03],
                            [16e9, 15.13],
                            [17e9, 14.89]])

ENR_uncertainty = 0.2

# %%
# Generate the ENR VS freq array for the N4000A


ENR_table_N4000A = np.array([[10e6, 5.505],
                             [100e6, 5.556],
                             [1e9, 5.559],
                             [2e9, 5.666],
                             [3e9, 5.678],
                             [4e9, 5.607],
                             [5e9, 5.574],
                             [6e9, 5.546],
                             [7e9, 5.614],
                             [8e9, 5.732],
                             [9e9, 5.746],
                             [10e9, 5.744],
                             [11e9, 5.792],
                             [12e9, 5.775],
                             [13e9, 5.844]])

# %%
# Generates the ENR interpolation array using the options:
# (original ENR table frequency points,
# original ENR table ENR values,
# polynomial order, 10th order seems to follow the curve of the original best
# interpolated frequency start,
# interpolated frequency stop,
# number of data points for interpolation)


ENR_INT_ARR_346b = interpolate(ENR_table_346b[:, 0],
                               ENR_table_346b[:, 1],
                               10,
                               freq[0],
                               freq[624],
                               len(freq))

 ENR_INT_ARR_N4000A = interpolate(ENR_table_N4000A[:, 0],
                                  ENR_table_N4000A[:, 1],
                                  10,
                                  freq[0],
                                  freq[624],
                                  len(freq))

 # %%
 # Save interpolated files to numpy arrays

 np.save('np_arrays\\ENR_INT_ARR_346b.npy', ENR_INT_ARR_346b)

 np.save('np_arrays\\ENR_INT_ARR_N4000A.npy', ENR_INT_ARR_N4000A)

```

Appendix F - Thermal simulation details

Figure 5: Cradle CFD SC Stream software used for the thermal simulations.

The simulation was setup to ignore radiation and the domain was set to vacuum as in Figure 117. Only the thermal path through solids was considered.

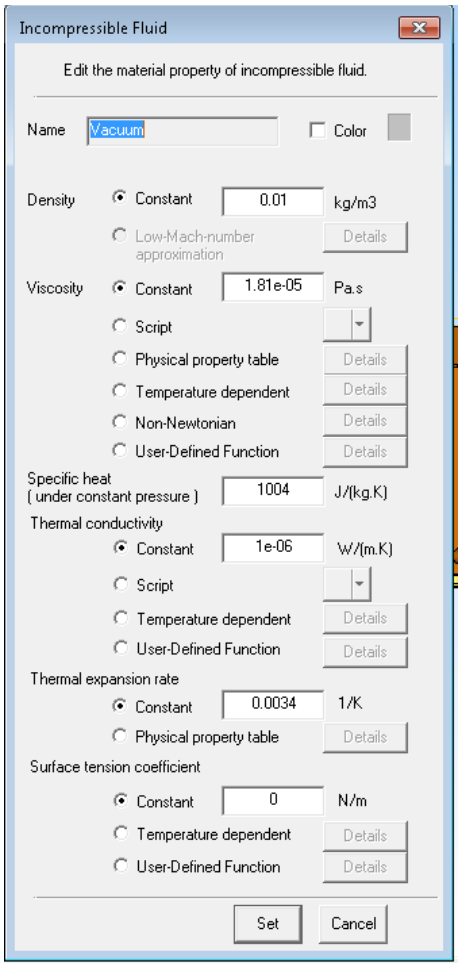

Figure 6: The domain medium was set to vacuum

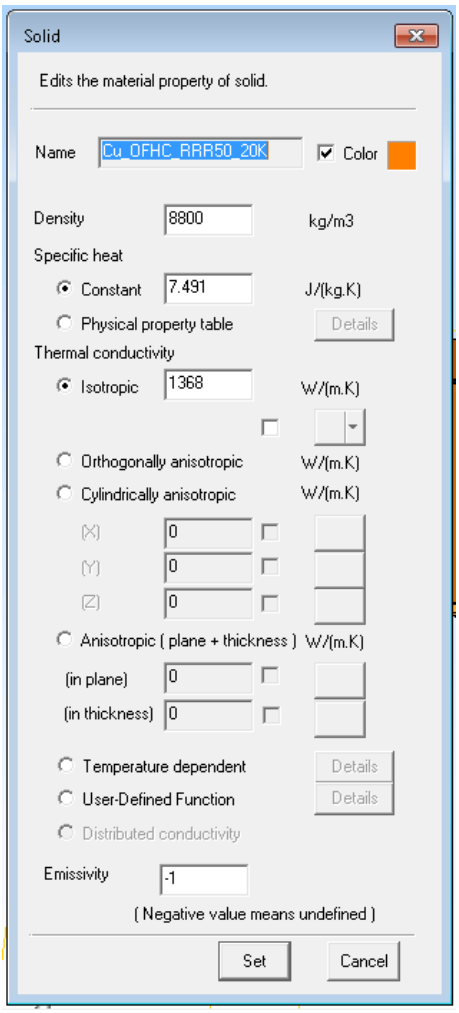

Figure 7: The copper parts material properties

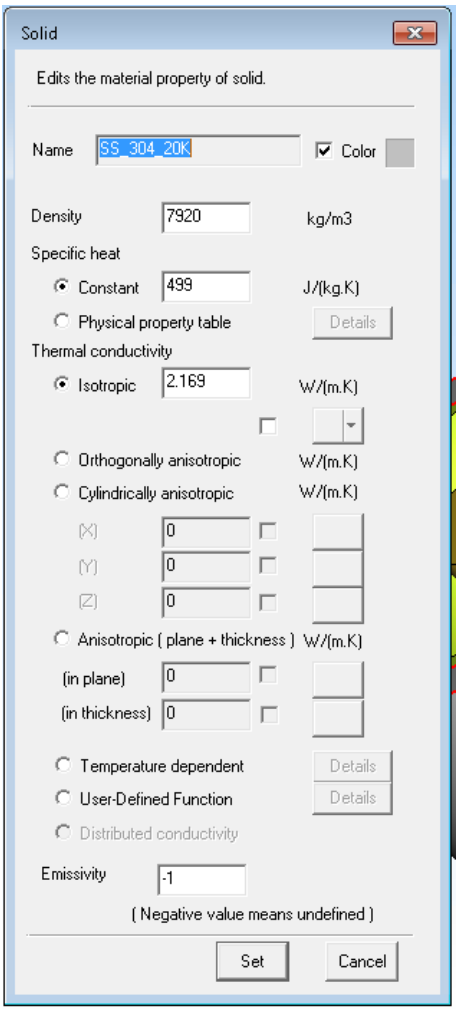

Figure 8: The stainless steel parts material properties

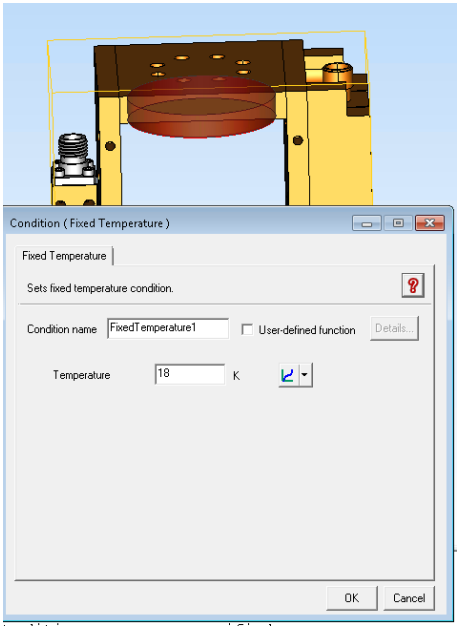

Figure 9: The cold head is modelled as a disk fixed to a physical temperature of 18 K

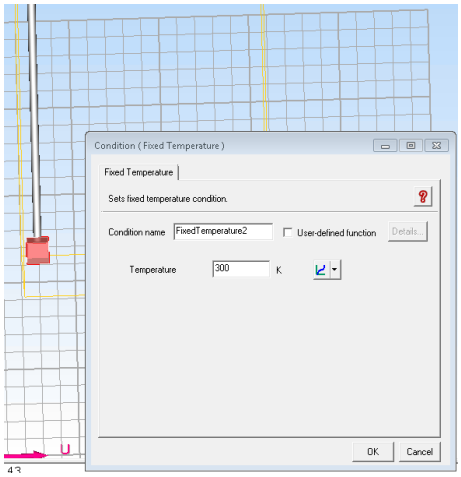

Figure 10: The end of the cable is terminated into a solid block that is fixed to a physical temperature of 300 K

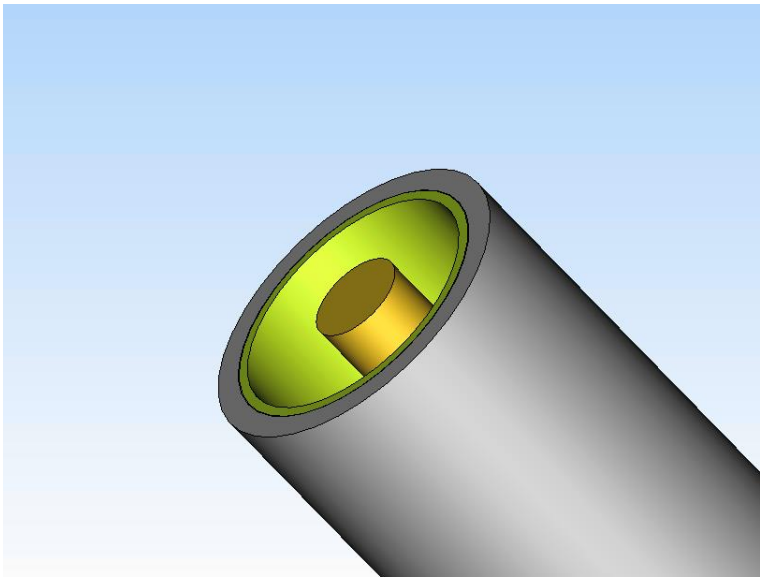

Figure 11: The modelled coaxial cable. The centre conductor is solid copper with diameter of 0.66 mm. The dielectric was modelled as an air gap in this case with a diameter of 1.801 mm. The outer conductor is copper with a thickness of 0.076 mm. The stainless-steel jacket with a thickness of 0.178 mm.